

Labelvrije biosensoren op basis van geavanceerde
fotonische ringresonatoren in silicium

Advanced Silicon Photonic
Ring Resonator Label-Free Biosensors

Tom Claes

Promotor: prof. dr. ir. P. Bienstman
Proefschrift ingediend tot het behalen van de graad van
Doctor in de Ingenieurswetenschappen: Fotonica

Vakgroep Informatietechnologie
Voorzitter: prof. dr. ir. D. De Zutter
Faculteit Ingenieurswetenschappen en Architectuur
Academiejaar 2011 - 2012



ISBN 978-90-8578-516-3
NUR 954
Wettelijk depot: D/2012/10.500/42

CONFIDENTIALITY NOTICE - IMPORTANT - PLEASE READ FIRST

This document may contain confidential information proprietary to the Universiteit Gent. It is strictly forbidden to publish, cite or make public in any way this document or any part thereof without the express written permission by the Universiteit Gent. Under no circumstance this document may be communicated to or put at the disposal of third parties; photocopying or duplicating it in any other way is strictly prohibited. Disregarding the confidential nature of this document may cause irreparable damage to the Universiteit Gent.

VERTROUWELIJKHEID - BELANGRIJK - LEES DIT EERST AUB

Dit document bevat geheime informatie toebehorend aan de Universiteit Gent. Het is ten strengste verboden om dit document of enig onderdeel ervan te publiceren, te citeren of op enige wijze publiek bekend te maken zonder uitdrukkelijke schriftelijke toestemming vanwege de Universiteit Gent. Onder geen enkele voorwaarde mag dit document gecommuniceerd of ter beschikking gesteld worden van derden; het is niet toegestaan het te fotokopiëren of op enige andere manier te dupliceren. Het niet respecteren van de vertrouwelijkheid van dit document kan de Universiteit Gent onherstelbare schade toebrengen.

Promotor:

prof. dr. ir. Peter Bienstman

Jury:

prof. dr. ir. H. Van Landeghem (chairman)	Ghent University
prof. dr. ir. P. Bienstman (promotor)	Ghent University
prof. dr. ir. F. Beunis (secretary)	Ghent University
prof. dr. ir. W. Bogaerts	Ghent University
dr. ir. R. Bockstaele	Ghent University
dr. ir. K. Gylfason	Royal Institute of Technology in Sweden

Ghent University
Faculty of Engineering and Architecture
Department of Information Technology
Photonics Research Group
Sint-Pietersnieuwstraat 41,
9000 Ghent, Belgium



**agency for Innovation
by Science and Technology**

This work was supported by the Flemish Agency for Innovation by Science and Technology (IWT) through a specialization grant, and was performed in the context of the European project InTopSens and the Belgian IAP project Photonics@BE. The European silicon photonics platform *ePIXfab* fabricated the photonic chips presented in this thesis.

Dank jullie wel!

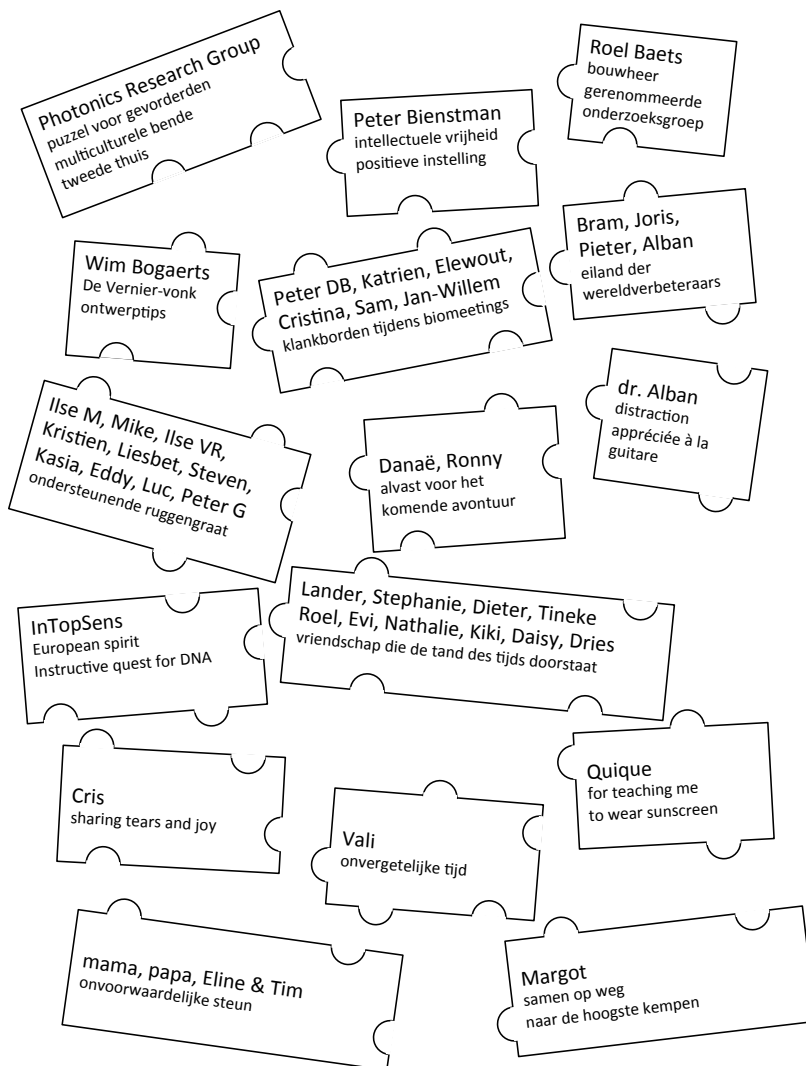


Table of Contents

Nederlandse samenvatting	xiii
English summary	xxiii
1 Introduction	1
1.1 Label-based biosensing	2
1.2 Label-free biosensing	4
1.3 State-of-the-art label-free technologies	5
1.4 Silicon photonic ring resonator label-free biosensors	7
1.4.1 Assets and drawbacks	8
1.4.2 State-of-the-art	11
1.4.3 Application domains	12
1.5 This thesis	14
1.6 Publications	15
1.6.1 Patent applications	15
1.6.2 International journal publications	15
1.6.3 International conference contributions	16
References	19
2 Silicon photonic ring resonator label-free biosensor platform	25
2.1 Silicon wire waveguides	26
2.1.1 Single-mode regime	27
2.1.2 Loss	29
2.1.3 Dispersion	31
2.2 Silicon ring resonators	32
2.2.1 All-pass ring resonators	33
2.2.2 Channel drop ring resonators	35

2.2.3	Lorentzian approximation of resonances	37
2.2.4	Coupling section	38
2.2.5	Silicon ring resonator for biosensing	39
2.3	Evanescent field sensing with ring resonators	43
2.3.1	Evanescent field	45
2.3.2	Sensitivity to refractive index changes	46
2.3.3	Binding curves	48
2.4	Limit of detection	50
2.4.1	Approximate formula	51
2.4.2	Influencing parameters	52
2.4.3	Reference sensors	54
2.4.4	Attainable limit of detection	56
2.5	Size limitation of silicon ring and disk resonator biosensors	60
2.6	Biochemical surface modification	62
2.7	Microfluidics	63
2.8	Optical interrogation	65
2.8.1	Grating couplers and access waveguides	65
2.8.2	Fiber interrogation	67
2.8.3	Remote interrogation	68
2.9	Conclusions	69
	References	71
3	Dual polarization ring resonator sensor	79
3.1	Working principle	80
3.2	Analytical model	82
3.3	Estimation of the accuracy	85
3.4	Implementation	87
3.4.1	Implementation with two access waveguides	88
3.4.2	Implementation with a single access waveguide	91
3.5	Experimental proof-of-concept	95
3.6	Conclusions	97
	References	98
4	Slot waveguide ring resonator sensor	101
4.1	Working principle	102
4.2	Design of a silicon slot waveguide for sensing	105

4.3	Fabrication of silicon slot waveguides	106
4.4	A silicon slot waveguide ring resonator sensor	108
4.5	Experimental sensitivity enhancement	110
4.6	Limit of detection	112
4.7	Conclusions	114
	References	117
5	Vernier-cascade sensor	121
5.1	Working principle	122
5.2	Transmission spectrum	125
5.2.1	Operational regimes	125
5.2.2	Transmission spectrum in the continuous regime	127
5.3	Performance	129
5.3.1	Sensitivity enhancement	129
5.3.2	Noise resistant tracking of the envelope peak	130
5.3.3	Limit of detection	131
5.4	Experimental proof-of-concept	135
5.4.1	Compact silicon Vernier-cascade sensor	136
5.4.2	Experimental sensitivity enhancement	138
5.5	Conclusions	139
	References	140
6	Low-cost and fast interrogation of a Vernier-cascade sensor	143
6.1	Working principle	145
6.2	Limit of detection	147
6.3	Compact silicon Vernier-cascade sensor with on-chip arrayed waveguide grating	149
6.4	Real-time refractive index change measurement	151
6.5	Conclusions	153
	References	154
7	Conclusions	157
7.1	Perspectives	159
A	First order approximation of the roundtrip phase	161
B	Derivation of the Lorentzian approximation of resonances	163
B.1	Lorentzian approximation of resonance dips	163

B.2 Lorentzian approximation of resonance peaks	164
C Derivation of a formula for the resonance wavelength shift due to an effective refractive index change	167
D Derivation of a formula for the limit of detection	169
References	172
E Derivation of a formula for the period of a Vernier-cascade's envelope signal	173
F Analysis of the constituent peaks in a Vernier-cascade's transmission spectrum	175
G Derivation of a formula for the envelope peak in a Vernier-cascade's transmission spectrum	179
H Derivation of a formula for a Vernier-cascade's sensitivity	183

List of Acronyms

BCB	Benzocyclobutene
DNA	Deoxyribonucleic acid
ELISA	enzyme-linked immunosorbent assay
FSR	Free spectral range
FWHM	Full-width at half-maximum
LED	Light-emitting diode
LOD	Limit of detection
PDMS	Polydimethylsiloxane

RIfS	Reflectometric interference spectroscopy
RIU	Refractive index units
RNA	Ribonucleic acid
SPR	Surface plasmon resonance
TE	Transverse electric
TM	Transverse magnetic

Nederlandse samenvatting (Dutch summary)

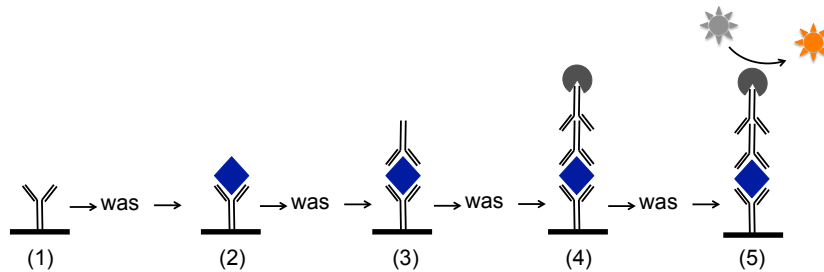
Inzicht in de moleculaire biologie van het menselijk lichaam bevordert vooruitgaan in de geneeskunde. Genetica bijvoorbeeld, in het bijzonder de recente ontwikkelingen in de snelle ontrafeling van hele genomen, laat de identificatie toe van erfelijke ziekten en van aanleg voor anderen, zoals bijvoorbeeld sommige kankers. Deze kennis helpt artsen bij het stellen van een diagnose en prognose, en kan tevens leiden tot aangepaste therapieën. Echter, ondanks de grote vooruitgang in onze kennis van de moleculaire basis van ziekten, is het nog steeds zeer uitdagend om de oorzaak van sommige ziekten te achterhalen en om methodes te ontwikkelen voor vroege diagnose en behandeling. Proteomica, de groteschaalstudie van eiwitten, heeft de capaciteiten om de limitering van genetische methodes te overwinnen, aangezien eiwitexpressies door ziektes veroorzaakte veranderingen kunnen ondergaan die niet zichtbaar zijn op het genetische niveau. Dit kan niet enkel worden toegepast in de ontdekking van dergelijke veranderingen, maar ook bij de identificatie van biomarkers voor vroege diagnoses en van nieuwe doelwitten voor medicijnen, en voor het versnellen van het proces voor het ontwikkelen van nieuwe medicijnen.

Het meten van de verschillende veranderingen die eiwitten kunnen ondergaan bij ziekte vormt een technologische uitdaging. Ten eerste is de techniek bij voorkeur in grootte mate gemultiplexeerd, wat betekent dat vele moleculaire interacties tegelijkertijd kunnen bestudeerd worden in hetzelfde vloeistofstaal, aangezien ziektes vaak de expressie van verschillende eiwitten tegelijkertijd veranderen. Ten tweede moet de techniek in

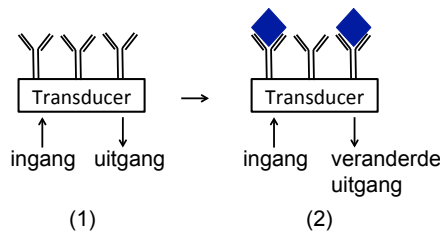
staat zijn om eiwitten te detecteren over een groot bereik van concentraties tot in het femtomolair-regime, terwijl de stalen ook hoge concentraties aan zout en andere eiwitten bevatten. Dit vereist een grootte specificiteit. Ten derde kunnen eiwitten niet efficiënt vermenigvuldigd worden, in in tegenstelling tot DNA, en hebben verschillende eiwitten vaak zeer uiteenlopende eigenschappen, wat de analyse verder bemoeilijkt. Bijkomende sterke punten voor de technologie zijn een hoge doorstroom (veel stalen per tijdseenheid), kwantitatieve metingen, beperkte voorbereiding van de stalen en een lage kost.

Een op dit moment belangrijke methode voor eiwitmetingen steunt op de onrechtstreekse detectie van een analiet door het binden van een gemakkelijk meetbaar label, zoals een fluorescente molecule of een enzym dat een zichtbaar signaal produceert. Een zeer populair test is de *enzyme-linked immunosorbent assay* (ELISA), die toelaat een antigen te meten in een teststaal (Figuur 1). Hoewel labelgebaseerde technieken een zeer lage detectielimiet kunnen bereiken en een hoge doorstroom en graad van multiplexering kunnen bieden (bijvoorbeeld *microarrays* in microtiterplaten), hebben ze ook verschillende nadelen. Ten eerste bieden ze enkel een eenmalige uitlezing, en laten dus geen continue meting van moleculaire interacties toe, waardoor informatie verloren gaat over de bindingskinetiek en -affiniteit. Ten tweede vereisen de meest specifieke *sandwich*-testen twee specifieke bindinspartners voor het analiet, die verschillende en niet-overlappende epitopen van het antigen herkennen. Dit limiteert de ontwikkeling van sterk gemultiplexeerde testen, and verhoogt ook de kost en ontwikkelingstijd ervan. Ten derde vergroten de wasstappen tussen de verschillende stappen in de test de voorbereidingstijd van de test, en verlagen op die manier de effectieve doorstroom.

Daarom krijgen labelvrije biosensoren de laatste tijd veel aandacht. Ze bevatten een *transducer* met receptormoleculen geïmmobiliseerd op het oppervlak (Figuur 1(b)) die rechtstreeks reageert op selectieve bindingsreacties tussen analietmoleculen en de geïmmobiliseerde receptormoleculen door middel van de inherente optische, elektrische of mechanische eigenschappen van het analiet. Meerdere transducers met verschillende receptormoleculen bieden een eenvoudige manier om meerdere moleculaire interacties tegelijkertijd te meten in een sterk gemultiplexeerde



(a) **Gelabelde metingen:** Een sandwich *enzyme-linked immunosorbent assay* (ELISA), een zeer specifieke en wijdverspreide gelabelde techniek om antigenen te detecteren in een vloeistofstaal, vereist in de eerste plaats (1) de immobilisatie van antilichamen die specifiek zijn voor het antigen op een vast oppervlak. Vervolgens wordt het teststaal in contact gebracht met dit oppervlak, zodat (2) de antigenen (indien aanwezig) binden aan de geïmmobiliseerde antilichamen. (3) Dan interageert een ander detectieantilichaam specifiek voor het antigen met de geïmmobiliseerde antigenen, dat (4) wordt herkend door een secundair antilichaam dat is gelinkt aan een enzymatisch label. Dit label produceert een zichtbare verkleuring wanneer het wordt ontwikkeld met een gepast substraat. Tussen de verschillende stappen van de test wordt het oppervlak grondig gespoeld met detergent om niet-specifiek gebonden moleculen weg te wassen.



(b) **Label-vrije metingen:** Een *transducer*, die rechtstreeks een inherente fysische eigenschap meet van biomoleculen, laat toe om continue bindingsreacties te meten tussen (1) antilichaamreceptoren geïmmobiliseerd op zijn oppervlak, en (2) antigenen in het teststaal.

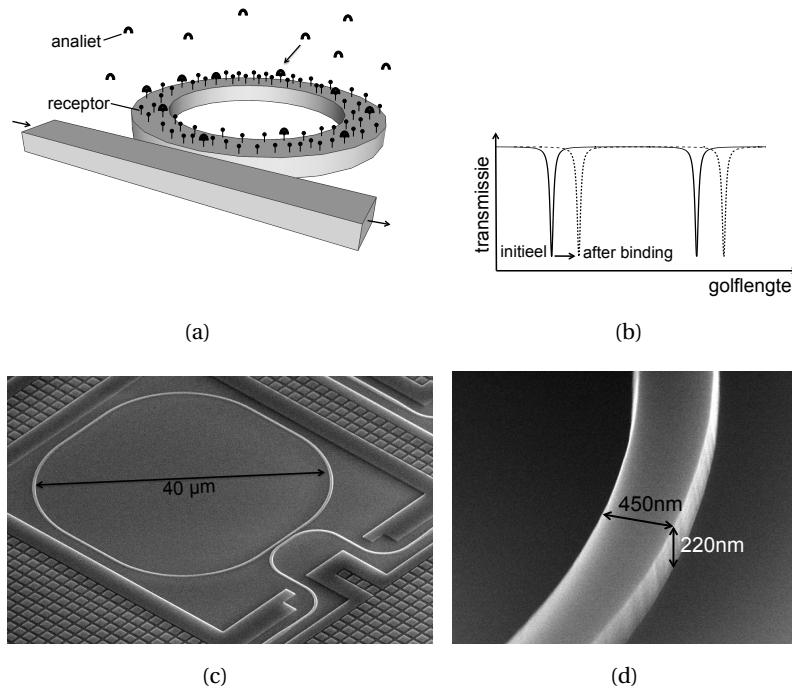
Figuur 1: Terwijl labelgebaseerde technieken de aanwezigheid van antigenen in een teststaal indirect meten door middel van de binding van gelabelde secundaire antilichamen, en daardoor vele stappen vereisen, laten labelvrije technieken toe om rechtstreeks bindingsinteracties te meten door middel van een fysische eigenschap van het antigen, en daardoor haast geen voorbereidende stappen vereisen. Bovendien laten labelvrije technieken continue controle toe van de binding, in tegenstelling tot de eenmalige uitlezing van labelgebaseerde technieken.

test. In tegenstelling tot labelgebaseerde technieken, laten vele labelvrije technieken toe om moleculaire interacties continu te meten, waardoor ze kwantitatieve gegevens bieden over de concentratie van het analiet en over de bindingskinetiek en -affiniteit. Bovendien vereisen ze haast geen voorbereiden van het teststaal, wat een positieve impact heeft op de kost en doorstroom. De ontwikkeling van nieuwe testen is ook eenvoudiger, in het bijzonder voor sterk gemultiplexeerde testen, aangezien ze maar één herkenningsmolecule vereisen voor elk analiet.

Analoog met elektronische geïntegreerde circuits, combineren en miniaturiseren fotonische geïntegreerde circuits optische functies, zoals (laser)bronnen, detectoren en filters, op een chip die bij voorkeur in massa kan gefabriceerd worden aan een hoge kwaliteit door middel van optische lithografie en etsing. Ze worden algemeen toegepast in optische vezelcommunicatienetwerken. Een golfgeleider die licht geleidt over de chip door middel van totale interne reflectie is de hoofdcomponent, en bestaat uit een kern met grote brekingsindex omringd door een mantel met kleine brekingsindex. Geleide optische modes zijn hoofdzakelijk opgesloten in de kern, met exponentieel uitstervende staarten in de mantel.

Een fotonische ringresonator bestaat uit een golfgeleider die op zichzelf is teruggeplooid om een gesloten lus te vormen waarin licht resoneert bij effectieve golflengtes die een geheel aantal keer in de lus passen. Tenminste één toegangsgolfgeleider bevindt zich dicht bij de ring om licht van en naar de resonator te koppelen door middel van de uitstervende staarten van de golfgeleidermodes. Bij de resonantiegolflengtes interfereert het licht in de toegangsgolfgeleider destructief met het licht dat van de resonator wordt teruggekoppeld, waardoor scherpe dips ontstaan in het transmissiespectrum.

Een labelvrije ringresonatorbiosensor meet rechtstreeks selectieve affiniteitsinteracties tussen analietmoleculen en receptormoleculen die geïmmobiliseerd zijn op het oppervlak van de ringresonatorgolfgeleider (Figuur 2). Aangezien de meeste biologische moleculen (eiwitten, DNA, ...) een brekingsindex (ongeveer 1.45) hebben die groter is dan die van het waterige oplosmiddel (ongeveer 1.31), veroorzaken die moleculaire bindingen een verhoging van de brekingsindex in het bereik van de uitster-



Figuur 2: (a) Een label-vrije ringresonatorbiosensor bestaat uit een golfgeleider met een chemisch aangepast oppervlak dat receptormoleculen presenteert die selectief zijn voor het analiet. Indien aanwezig in het vloeibaar teststaal, diffunderen analietmoleculen naar de sensor en binden daar aan de receptormoleculen, waardoor de brekingsindex in het bereik van de uitsterven optische staart verandert. (b) De resulterende verschuiving van de resonantiegolflengte representeert de concentratie van het analiet, en de bindingskinetiek en -affiniteit van de biochemische reactie. (c) Silicium-op-insulator fotonische ringresonatorsensoren bestaan volledig uit golfgeleiders met een groot brekingsindexcontrast, en kunnen daardoor zeer compact gemaakt worden.

vende staart van het golfgeleidermode. De resulterende faseverandering van de optische mode veroorzaakt een meetbare verschuiving van de resonantiegolflengte van de ring, die continu gemeten wordt en die informatie geeft over de concentratie van het analiet, de affiniteit tussen de moleculen en de kinetiek van de biochemische reactie.

Afgelopen jaren hebben silicium labelvrije ringresonatorbiosensoren bezwezen uitmuntende sensoren te zijn, die de vergelijking met andere la-

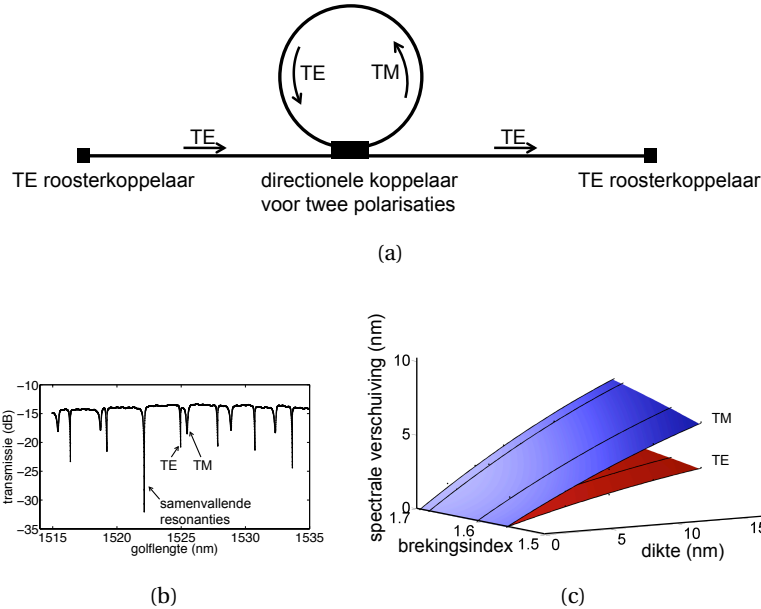
belgebaseerde en labelvrije technologieën zeker kunnen doorstaan. Verschillende aspecten vereisen echter nog verbeteringen alvorens een grote gebruikersgroep kan worden overtuigd. Hoewel er nog een grote marge voor verbetering is in de ontwikkeling van specifieke biochemische testen op het platform, denken wij dat ook het optische platform nog verder kan worden verbeterd. Aangezien de *Photonics Research Group* van de Universiteit Gent - imec vele jaren ervaring heeft in siliciumfotonica, bevinden we ons in een goede positie om verdere verbeteringen aan het platform te verkennen op het niveau van de silicium ringresonator.

Een gekend probleem voor alle labelvrije platformen is dat de rechtstreekse testen vaak minder specifiek zijn dan sandwich-testen, aangezien slechts een enkele biomoleculair herkenningselement wordt gebruikt. De ringresonator met tweevoudige polarisatie die wij voorstellen (Figuur 3) kan een onderscheid maken tussen de brekingsindex en dikte van dunne diëlektrische laagjes, en heeft de capaciteiten om dit voldoende nauwkeurig te doen om een onderscheid te kunnen maken tussen specifieke en niet-specifieke interacties. Bovendien laat hij toe om moleculaire interacties diepgaander te bestuderen door informatie te bieden over bijvoorbeeld de oriëntatie van DNA-moleculen of over de vorm van eiwitten, waarvan geweten is dat het een belangrijke rol speelt bij ziektes zoals sommige kankers en bij de ziekte van Alzheimer.

Een ander gekend probleem van het platform is dat de huidige detectielimiet (LOD) (1.5 pg/mm^2) onvoldoende is voor de directe (onversterkte) detectie van kleine moleculen, zoals cytokines bij klinisch relevante concentraties. Daarom hebben we een benaderende formule afgeleid voor de detectielimiet van nauwkeurige concentratiemetingen die werken door middel van het fitten van die initiële helling van bindingscurves met een kleinste kwadratenmethode.

$$LOD \approx 3.29 \cdot \frac{2\sqrt{3} \cdot \sigma_{\Delta\lambda}}{\sqrt{R_t} \cdot T^{\frac{3}{2}} \cdot S_{slope}}$$

waarbij $\sigma_{\Delta\lambda}$ de standaardafwijking is van de Gaussische ruis op de bindingscurve, R_t de temporele resolutie van de bindingscurve, en T de meettijd. De hellingsgevoeligheid S_{slope} is de helling van de calibratiecurve bij concentratie nul.



Figuur 3: (a) Zowel de quasi-TE and quasi-TM mode van de ringresonator kunnen beiden geëxiteerd worden door de verliesarme quasi-TE mode van een enkele toegangsgolfgeleider. De door ons gekozen directionele koppelaar voor de koppeling van beide polarisaties bestaat uit twee golfgeleiders met verschillende breedte die gekozen zijn zodat de effectieve brekingsindex van de quasi-TE mode van de toegangsgolfgeleider die van de quasi-TM mode van de ringgolfgeleider benadert, zodat koppeling tussen beiden mogelijk is ondanks het sterk verschillende modeprofiel. (b) Het gemeten vezel-tot-vezel transmissiespectrum van een silicium implementatie van deze sensor in water vertoont duidelijk zichtbare resonantiedips voor zowel de quasi-TE als de quasi-TM modes, zodat beiden nauwkeurig en onafhankelijk kunnen worden gevolgd. De extinctie stijgt drastisch wanneer twee modes overlappen. (c) De quasi-TM mode van onze sensor is gevoeliger voor gedeponeerde diëlektrische laagjes dan de quasi-TE mode, zoals verwacht door de verschillende modeprofielen en zoals gewenst om een onderscheid te kunnen maken tussen de brekingsindex en dikte van de laag.

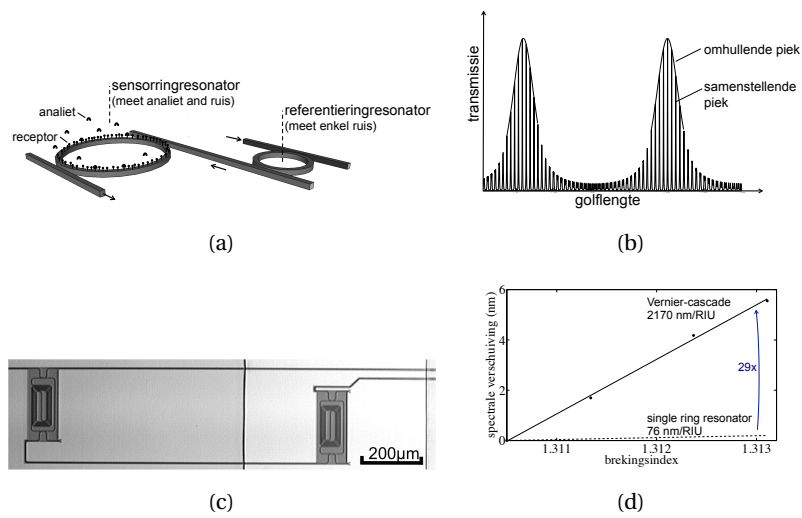
De formule identificeert de bepalende parameters en kan dienst doen als maatstaf bij de initiële vergelijking van transducers en uitleestechnieken. Ze toont dat de resonantiegolflengtegevoeligheid slecht één van de parameters is, en dat de temporele resolutie en de ruis op de bindingscurve ook een belangrijke invloed hebben op de detectielimiet. De formule

benadrukt de noodzaak voor referentiesensoren die brekingsindex- en temperatuursruis compenseren. Een tweede implicatie van de formule is dat niet alleen scherpe en diepe resonantiedips belangrijk zijn in het ontwerp van ringresonatorsensoren, maar ook een kleine periode, aangezien die toelaat sensoren sneller uit te lezen met een golflengtescan in een sterk gemultiplexeerd platform. Ringresonatorsensoren lange (tot 7 mm) opgevouwen caviteiten zijn daardoor in het voordeel.

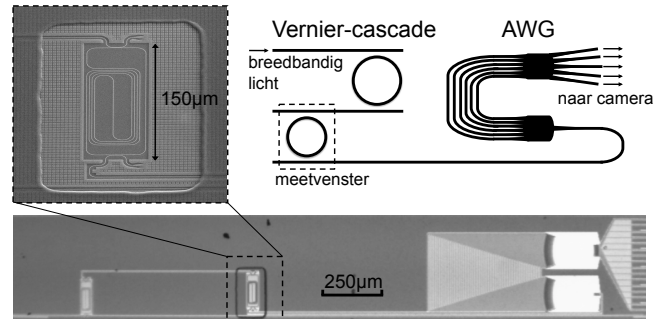
Sleufgolffeleiderringresonatorsensoren bleken de resonantiegolflengtegevoeligheid te vergroten door middel van een verhoogde interactie tussen de optische mode en de gebonden moleculen. De zesvoudige winst bleek echter te klein om de nadelen te compenseren, zoals de extra optische verliezen en bemoeilijkte oppervlaktemodificatie.

Vernier-cascade ringresonatorsensoren (Figuur 4) leveren een veel grotere winst van de golflengtegevoeligheid (tot twee grootte-orde), en bemoeilijken de biochemische oppervlaktemodificatie niet extra, en compenseren bovendien de meest belangrijke ruisfactoren op een optische manier. Hoewel ze minder geschikt zijn voor snelle uitlezingen met een golflengtescan door hun breed transmissiespectrum, kunnen ze worden gecombineerd met geïntegreerde golflengtefilters op de chip voor uiterst snelle en kostenbesparende uitlezing met een breedbandige lichtbron (Figuur 5). Onze eerste resultaten geven aan dat deze transducer dezelfde of zelfs betere detectielimiet kan bieden als geoptimaliseerde ringresonatorsensoren met afzonderlijk uitgelezen referentiesensoren die uitgelezen worden met dure en grote top lasers met een externe caviteit. Bovendien bieden ze het vooruitzicht op compactere uitleesinstrumentatie die kan worden ingezet in een bredere groep van toepassingen.

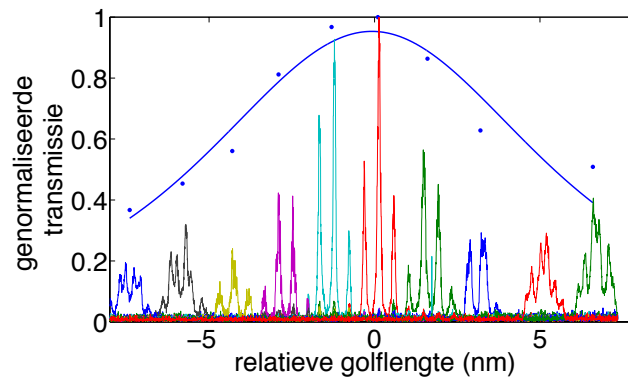
Deze thesis introduceert nieuwe silicium fotonische transducers voor labelvrije biochemische metingen, en stelt initiële testen voor die hun sterke en zwakke punten weergeven. Opvolgend onderzoek kan zich best focussen op het uittesten van relevante biochemische testen in (verdund) serum op een geoptimaliseerde opstelling, om de noodzakelijke data te genereren voor een uitgebreide vergelijking met andere technologieën.



Figuur 4: (a) Een Vernier-cascadesensor bestaat uit twee opeenvolgende ringresonatoren, waarvan slechts één beschikt over receptormoleculen die selectief zijn voor het analiet. (b) Hij kan beschikken over een transmissiespectrum met scherpe pieken waarop een periodieke omhullende is gesuperponeerd. Terwijl gemeenschappelijke ruis van de ringresonatoren slechts resulteert in een kleine verschuiving van de omhullende, zal selectieve binding van het analiet aan die ene ringresonator een differentiële resonantiegolflengteverschuiving veroorzaken tussen beide resonatoren, en daardoor een veel grotere verschuiving van de omhullende. (c) De silicium Vernier-cascadesensor die werd gebruikt voor de experimentele verificatie van het concept bestaat uit twee 2.5 mm-lange resonatoren waarvan de oppervlakte is beperkt door de caviteit op te vouwen. (d) Het omhullende signaal in het transmissiespectrum verschoof 29 keer sterker ten gevolge van brekingsindexveranderingen dan de resonantiegolflengteverschuiving van een gewone ringresonatorsensor.



(a)



(b)

Figuur 5: (a) Een *arrayed waveguide grating* (AWG) is een gekende spectrale filter die zeer compact kan gemaakt worden in silicium, terwijl hij toch voldoende spectrale resolutie biedt (in de orde van een nanometer) om nauwkeurig genoeg de omhullende uit het transmissiespectrum van een Vernier-cascade te filteren. De microscopische afbeelding van de silicium chip toont de compacte opgevouwen caviteiten van de Vernier-cascade, die is verbonden met een compacte 16-kanaals AWG. (b) Het transmissiespectrum van de Vernier-cascade gefilterd door de verschillende kanalen van de AWG (een kleur per kanaal) vertoont het omhullende signaal gesuperponeerd op de scherpe transmissiepieken wanneer het gemeten wordt met een laser. Aangezien er per kanaal ongeveer drie scherpe pieken zijn, is er voldoende vermogenuitmiddeling per kanaal om de omhullende rechtstreeks weer te geven wanneer de transmissie wordt gemeten met een breedbandige bron (blauwe punten). Het kwadraat van een Lorentzianse functie fit behoorlijk aan het breedbandig transmissiespectrum (blauwe lijn), zodat de positie van de piek van de omhullende voldoende nauwkeurig kan worden gemeten.

English summary

Insight in the molecular biology of the human body helps to advance medicine. Genetics, especially the advances in the rapid sequencing of genomes made over the last decade, allowed the identification of hereditary diseases and predispositions for others, such as cancer. This knowledge helps clinicians with the diagnosis and prognosis, and can also lead to adapted therapies.

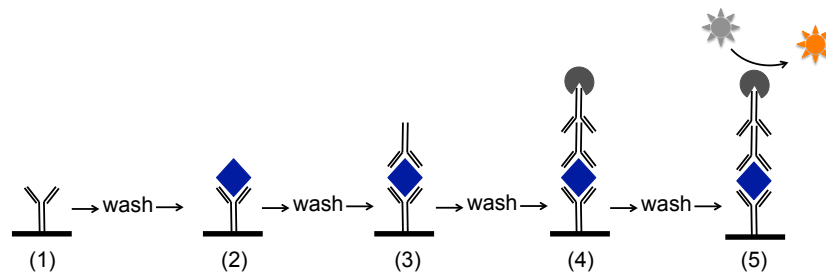
However, despite the large progress in our understanding of the molecular basis of diseases, it is still very challenging to further explore their causes and to develop methods for early diagnosis and treatment. Proteomics, the large-scale study of proteins, has the prospect of overcoming the limitations of genetic approaches, as protein expression can undergo disease-mediated alternations that are not visible at the genetic level. Applications include the discovery of altered protein expression, in tissue or in biological fluids, identification of novel biomarkers for early diagnosis of diseases and of new targets for therapeutics, and acceleration of drug development.

Measuring the many different features of proteins that can be altered in a disease form a technological challenge. First, the technique should be highly multiplexed, meaning that many molecular interactions can be monitored in the same sample, since often the expression of multiple proteins is altered by a disease. Second, the technique should be capable to detect proteins over a wide range of concentrations down to the femtomolar-range, while the sample contains high levels of salt and other proteins at concentrations up to several hundreds of micromolars. This demands a high specificity. Third, in contrast to DNA, proteins cannot be amplified efficiently, and different proteins can have very different

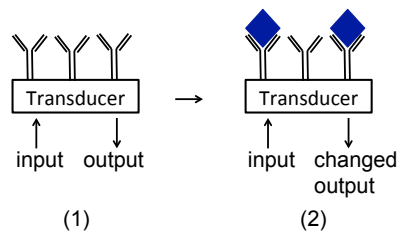
properties, further complicating the analysis. Additional assets for the technology are a high throughput, so that many samples can be analyzed in a short period of time, quantitative measurements, little sample preparation and low-cost.

Nowadays, an important method for protein measurements relies on the indirect detection of an analyte by attaching an easy to measure label to it, such as a fluorescent dye or an enzyme that produces a visible signal. A very popular assay is the *enzyme-linked immunosorbent assay* (ELISA), which allows to measure antigens in a sample (Figure 1). While labeled techniques can attain limits of detection down to the single-molecule level and offer a high degree of multiplexing and throughput (e.g. microarrays in microtiter plates), they have several practical drawbacks. First, labeling and sandwich assays only provide end-point read-out, and do not allow continuous, real-time monitoring of molecular interactions, thus losing information on the binding kinetics and affinity. Second, the most selective sandwich-type assays require two high-affinity capture agents that recognize distinct and non-overlapping target epitopes, which often limits the development of highly multiplexed assays, and augments the cost and development time. Third, the required washing in between different steps of the assay often increase the required sample preparation, and can reduce the effective throughput.

Therefore, label-free affinity biosensors lately receive a lot of attention. They consist of a transducer with receptor molecules immobilized on its surface (Figure 1(b)) that directly responds to a selective affinity interaction between analyte molecules and the immobilized receptor molecules through the inherent optical, electrical or mechanical properties of the analyte. Multiple transducers with different receptor molecules provide an easy way to monitor multiple parameters in a highly multiplexed assay. In contrast to labeled techniques, many label-free methods allow to continuously monitor the affinity reaction, providing highly quantitative measures on the concentration, affinity and binding kinetics. Moreover, label-free assays require almost no sample preparation, reducing the cost and enhancing the throughput. The assay development is also significantly simplified, especially for highly multiplexed assays, since only one recognition element is required for each analyte.



(a) **Labeled sensing:** A sandwich *enzyme-linked immunosorbent assay* (ELISA), a very specific and widespread labeled technique to detect antigens in a fluidic sample, first (1) involves the immobilization of antibodies specific to the target antigen on a solid surface. Then the test sample is brought into contact with the surface, if present (2) allowing the antigen to bind to the immobilized antibodies. Thereafter, (3) a detection antibody specific to the antigen interacts with the immobilized antigens, and subsequently (4) is recognized by a secondary antibody linked to an enzymatic label that (5) produces a visible signal upon reaction with an enzymatic substrate. In between the different steps, non-specifically bound molecules are washed with detergent.



(b) **Label-free sensing:** A transducer that directly measures an inherent physical property of biomolecules provides a straightforward way to continuously monitor affinity interactions between antibody receptor molecules immobilized on its surface (1), and antigens in the test sample (2).

Figure 1: Whereas labeled techniques indirectly measure the presence of an antigen in a test sample through the binding of labeled secondary recognition elements, and require many assay steps, label-free techniques directly measure affinity interactions through a physical property of the analyte and almost need no sample preparation. Moreover, label-free techniques allow continuous monitoring of the binding, as opposed to the end-point read-out of labeled techniques.

In analogy to electronic integrated circuits, photonic integrated circuits combine and miniaturize optical functions, such as (laser) sources, detectors and filters, on a chip that can preferably be mass manufactured at high quality using optical lithography and etching. They are commonly applied in optical fiber communication networks. A waveguide that guides light over the chip by total internal reflection is the principal component, and consists of a high-refractive-index core surrounded by a low-refractive-index cladding. Guided modes are mainly confined in the core, with exponentially decaying evanescent tails in the cladding.

A photonic ring resonator consists of a waveguide that is folded back on itself to form a closed loop in which light resonates at effective wavelengths that fit an integer times in the loop. At least one access waveguide is positioned close to the ring resonator to couple light to and from the resonator through evanescent wave coupling. It connects the ring to a (possibly remote) source and detector. At the resonance wavelengths, light in the access waveguide destructively interferes with light coupled back from the ring resonator, causing sharp dips in the transmission spectrum.

A ring resonator label-free biosensor directly measures selective affinity interactions between analyte molecules and receptor molecules immobilized on the ring waveguide surface (Figure 2). Since most biological molecules (proteins, DNA, ...) have a refractive index (around 1.45) larger than that of the aqueous solvent (around 1.31), this molecular binding locally increases the refractive index in the range of the evanescent field of the waveguide mode. The resulting phase change of the mode induces measurable shifts of the resonance wavelengths of the ring, which are continuously monitored over time and which give information on the analyte concentration, affinity between the molecules and the kinetics of the biochemical reaction.

In recent years, silicon ring resonator label-free biosensors have proven to be excellent sensors, comparing favorably with many other labeled and label-free sensing techniques. However, many aspects still need improvement in order to convince a large user-base. While there are many opportunities in the development of specific assays, we think there is also still room for improvements in the optical platform. Being embedded in

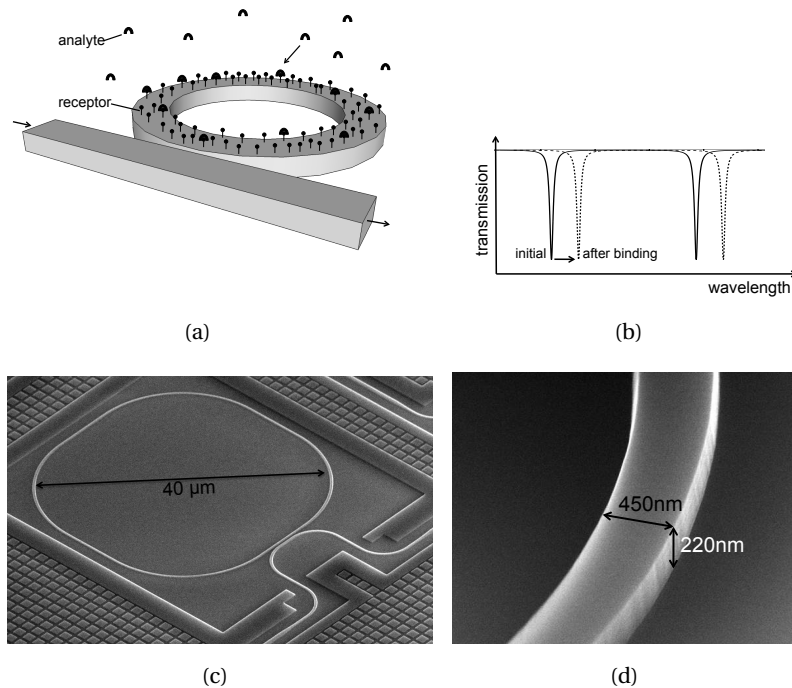


Figure 2: (a) A ring resonator label-free biosensor consists of a waveguide with a chemically modified surface that presents receptor molecules that are selective to the analyte. Analyte molecules, if present in a fluidic sample, diffuse to the sensor and bind to the receptors, increasing the refractive index in the range of the evanescent field of the ring resonator waveguide. (b) The consequent shift of the resonance wavelength signifies the concentration of the analyte, and the kinetics and affinity of the biochemical reaction. (c) Silicon-on-insulator photonic ring resonator sensors entirely consist of high-refractive index contrast waveguides, and can therefore be made very compact.

the *Photonics Research Group* of Ghent University - imec, that has many years of experience in silicon photonics, we are well-positioned to explore methods to improve the sensor platform at the level of the silicon ring resonator transducer.

A common problem for all label-free platforms is that straightforward direct label-free assays are often less specific than sandwich assays, since they only employ a single biomolecular recognition element. The dual polarization ring resonator sensor we propose (Figure 3) can distinguish

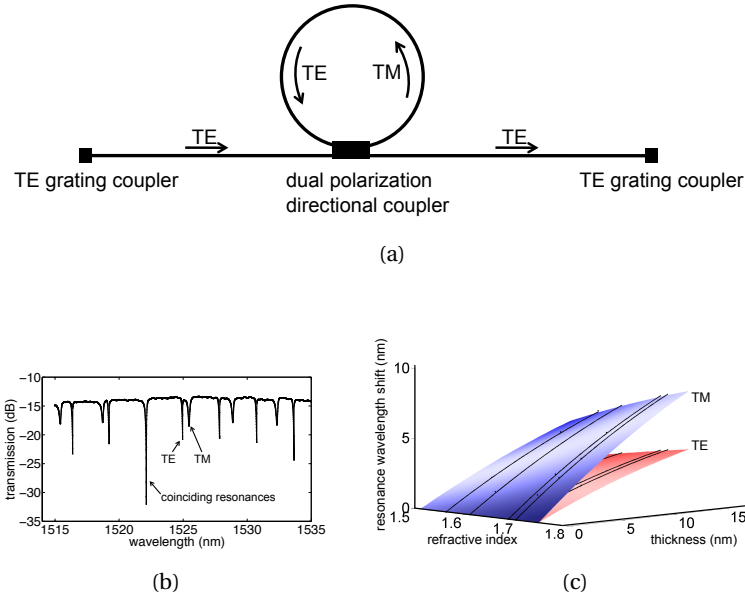


Figure 3: (a) Both the quasi-TE and quasi-TM mode in the ring resonator can be excited from the low-loss quasi-TE mode of a single access waveguide. Our dual polarization directional coupler consists of two waveguides with different widths, that are chosen so that the effective refractive index of the quasi-TE mode of the access waveguide is close to that of the quasi-TM mode of the ring waveguide, thus allowing coupling between the two despite the very different field profiles. (b) The measured fiber-to-fiber transmission spectrum of a water-clad silicon implementation has clearly visible resonance dips for both the quasi-TE and quasi-TM modes, allowing accurate and independent tracking of both. When two resonances overlap, the extinction increases significantly. (c) The quasi-TM mode of our sensor is more sensitive to deposited dielectric layers, as expected from their different field profiles and confinement and as desired to differentiate between the refractive index and thickness of the layer.

between the refractive index and thickness of thin dielectric layers, and has the prospect of being able to do so with sufficient accuracy to measure structural molecular changes that allow distinguishing specific interactions from non-specific ones. Moreover, it allows to study molecular interactions in more depth by providing information on e.g. DNA-orientation or protein conformation, which has already proven to play an important role in several cancers and in Alzheimer's disease.

Another primary concern of the platform is the moderate limit of detection (LOD) (1.5 pg/mm^2), as it is insufficient for the direct (unamplified) detection of small molecules, such as cytokines at clinically relevant concentrations. Therefore, we derived an approximate formula for the limit of detection of accurate concentration measurements based on least-squares fitting the initial slope of the binding curve.

$$LOD \approx 3.29 \cdot \frac{2\sqrt{3} \cdot \sigma_{\Delta\lambda}}{\sqrt{R_t} \cdot T^{\frac{3}{2}} \cdot S_{slope}}$$

with $\sigma_{\Delta\lambda}$ the standard deviation of the Gaussian noise on the binding curve, R_t the temporal resolution of the binding curve, and T the measurement time. The slope sensitivity S_{slope} is the slope of the calibration curve at zero concentration ($S_{slope} = \frac{\partial\alpha(C=0)}{\partial C}$).

It identifies the governing parameters and can serve as a figure of merit in the initial comparison of transducers and interrogation techniques. It shows that the resonance wavelength sensitivity of the ring sensor is only one parameter, and that the temporal resolution of and the noise on the binding curve also have a significant impact. The formula first of all indicates that reference sensors for compensation of refractive index and temperature noise are indispensable. A second implication of the formula is that not only sharp and deep resonances are important in the design of ring resonator sensors, but also small values of the free spectral range, since this allows faster interrogation of a multiplexed platform using wavelength scanning. Therefore, ring resonator sensors with large roundtrips (up to 7 mm) in folded cavities are beneficial.

Slot waveguide ring resonator sensors were found to improve the resonance wavelength sensitivity through enhanced light-matter interaction. However, the sixfold gain is too small to compensate the drawbacks: extra optical losses and troubled biochemical surface modification.

Vernier-cascade ring resonator sensors (Figure 4) have a much larger gain of the wavelength sensitivity (up to two order of magnitude), do not complicate the biochemical surface modification, and additionally optically compensate the most important noise factors. Although they are less suited for fast interrogation with a wavelength scan because of their broad

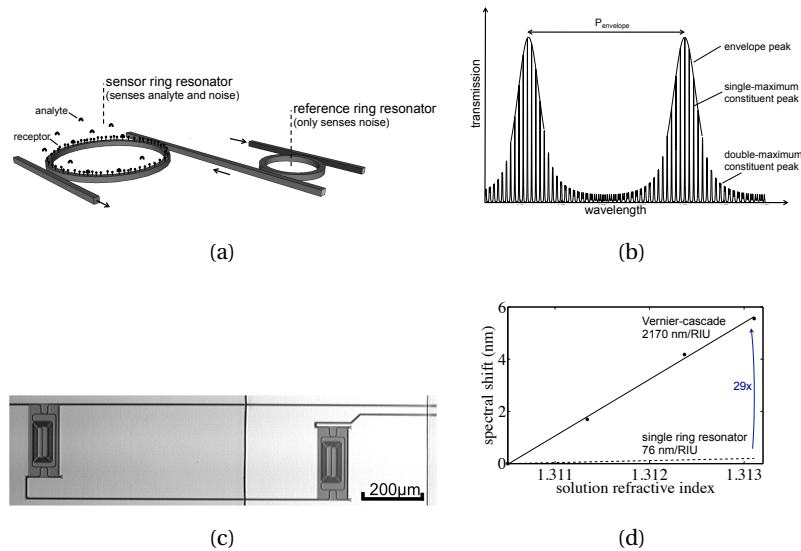


Figure 4: (a) A Vernier-cascade sensor consists of two channel drop ring resonators that are cascaded, so that the drop signal of the first resonator serves as the input of the second. Only the sensor resonator has receptors immobilized on its surface and selectively reacts to the analyte. The ring resonators have a different optical roundtrip, and therefore a comb spectrum with different free spectral range. (b) The transmission spectrum of a Vernier-cascade that operates in the continuous regime manifests a periodic envelope signal superposed on sharp constituent peaks. Common noise will shift the resonances of both resonators, and only results in a small shift of the Vernier-cascade spectrum. However, selective analyte binding to the sensor resonator results in a differential resonance wavelength shift between the resonators, and therefore in a much larger shift of the Vernier-cascade transmission spectrum. (c) The silicon Vernier-cascade sensor used for the proof-of-concept measurements consists of two 2.5 mm-long resonators of which the footprint is reduced by folding the cavity. A 500 nm-thick silicon oxide cladding covers the complete chip except for the etched opening to the sensor ring resonator, so that only this resonator reacts to refractive index changes of liquid flowing over the sensor, and differential resonance wavelength shifts between the resonators can easily be applied. (d) The envelope signal of the studied silicon Vernier-cascade sensor is 29 times more sensitive to liquid refractive index changes than a single ring resonator.

transmission spectrum, they can be combined with an on-chip spectral filter to provide very fast and cost-effective interrogation with a broadband light source (Figure 5). Our preliminary results indicate that this transducer can offer the same or better limit of detection than optimized ring resonator sensors with separate reference sensors that are interrogated with an expensive and bulky high-end external cavity laser. Moreover, it provides the prospect of more compact read-out instrumentation that is applicable in a wider set of applications.

This thesis introduces novel silicon photonic transducers for label-free sensing, and presents initial proofs-of-concept that indicate their strengths and weaknesses. Follow-up research should focus on performing relevant multiplexed assays in (diluted) serum in an optimized read-out instrument to provide the necessary data for a proper comparison with other technologies.

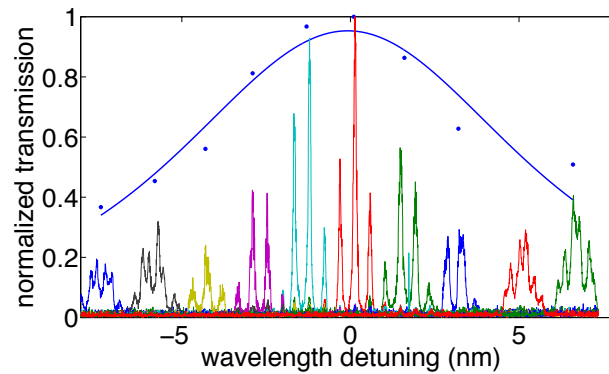
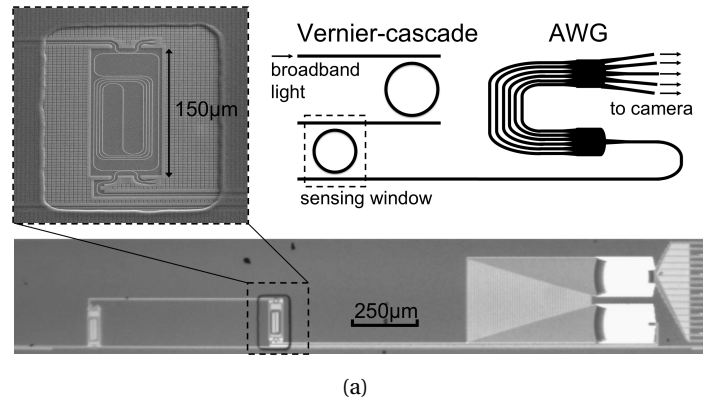


Figure 5: (a) An arrayed waveguide grating (AWG) is a well-known spectral filter that can be made very compact with high quality in silicon, while providing sufficient spectral resolution (in the order of a nanometer) to accurately filter the envelope from the transmission spectrum of a Vernier-cascade. The micrograph of the silicon-on-insulator chip shows the compact folded cavities of the ring resonators constituting the Vernier-cascade that is connected to a dense 16-channel AWG. (b) The transmission spectrum of the Vernier-cascade through different channels of the AWG measured with a tunable laser (bottom, a color for each AWG-channel) shows the envelope peak superposed on the sharp constituent peaks. Approximately three constituent peaks are transmitted by each channel, providing enough power averaging per channel to also reveal the shape of the envelope peak when the transmission is measured with a broadband light source (blue dots). A squared Lorentzian function can be satisfactorily fitted to the broadband transmission peak (blue line), allowing accurate determination of the peak position.

1

Introduction

Insight in the molecular biology of the human body helps to advance medicine. Genetics, especially the advances in the rapid sequencing of genomes made over the last decade, allowed the identification of hereditary diseases and predispositions for others, such as cancer. This knowledge helps clinicians with the diagnosis and prognosis, and can also lead to adapted therapies. In the case of breast cancer for example, gene expression profiling was found to be a better predictor of disease outcome than clinical and histological classification [1].

However, despite the large progress in our understanding of the molecular basis of diseases, it is still very challenging to further explore their causes and to develop methods for early diagnosis and treatment. Proteomics, the large-scale study of proteins, has the prospect of overcoming the limitations of genetic approaches, as protein expression can undergo disease-mediated alternations that are not visible at the genetic level. Applications include the discovery of altered protein expression, in tissue or in biological fluids, identification of novel biomarkers for early diagnosis of diseases and of new targets for therapeutics, and acceleration of drug development [2]. Of special interest is the direct analysis of proteins in blood serum, the liquid portion of blood without clotting factors, since it

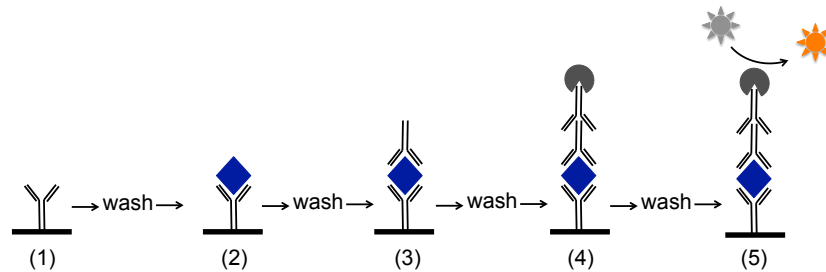
is an easy accessible liquid that contains a variety of proteins released by diseased tissue [3].

Measuring the many different features of proteins that can be altered in a disease forms a technological challenge [2]. First, the technique should be highly multiplexed, meaning that many molecular interactions can be monitored in the same sample, since often the expression of multiple proteins is altered by a disease. Second, the technique should be capable to detect proteins over a wide range of concentrations down to the femtomolar-range, while the sample contains high levels of salt and other proteins at concentrations up to several hundreds of micromolars. This demands a high specificity. Third, in contrast with DNA, proteins cannot be amplified, and different proteins can have very different properties, further complicating the analysis. Additional assets for the technology are a high throughput, so that many samples can be analyzed in a short period of time, quantitative measurements, little sample preparation and low-cost.

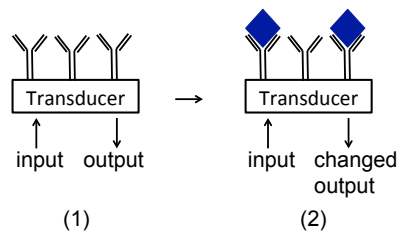
1.1 Label-based biosensing

Nowadays, an important method for protein measurements relies on the indirect detection of an analyte by attaching an easy to measure label to it, such as a fluorescent dye or an enzyme that produces a visible signal. A very popular assay is the *enzyme-linked immunosorbent assay* (ELISA) [4], which allows to measure antigens in a sample (Figure 1.1(a)). First, an unknown quantity of antigen in a fluidic test sample is immobilized on a surface, either via non-specific adsorption (indirect ELISA) or via specific binding to previously immobilized antibodies (sandwich ELISA). Then, a detection anti-body specific to the antigen is added, which binds to the immobilized antigens. This detection anti-body is either directly linked to an enzymatic label or recognized by an extra labeled non-specific anti-body. In between the different steps, the surface is washed with a detergent solution to remove non-specifically bound molecules. To conclude the assay, an enzymatic substrate is added that reacts with the enzymatic labels to produce a visible signal indicative for the presence and quantity of the antigen in the sample. Today, ELISA is one of the primary tests for the diagnosis of human immunodeficiency virus (HIV) infection [5].

Typically, labeled assays such as ELISA are performed inside the wells



(a) **Labeled sensing:** A sandwich *enzyme-linked immunosorbent assay* (ELISA) [4], a very specific and widespread labeled technique to detect antigens in a fluidic sample, first (1) involves the immobilization of antibodies specific to the target antigen on a solid surface. Then the test sample is brought into contact with the surface, if present (2) allowing the antigen to bind to the immobilized antibodies. Thereafter, (3) a detection antibody specific to the antigen interacts with the immobilized antigens, and subsequently (4) is recognized by a secondary antibody linked to an enzymatic label that (5) produces a visible signal upon reaction with an enzymatic substrate. In between the different steps, non-specifically bound molecules are washed with detergent.



(b) **Label-free sensing:** A transducer that directly measures an inherent physical property of biomolecules provides a straightforward way to continuously monitor affinity interactions between antibody receptor molecules immobilized on its surface (1), and antigens in the test sample (2).

Figure 1.1: Whereas labeled techniques indirectly measure the presence of an antigen in a test sample through the binding of labeled secondary recognition elements, and require many assay steps, label-free techniques directly measure affinity interactions through a physical property of the analyte and almost need no sample preparation. Moreover, label-free techniques allow continuous monitoring of the binding, as opposed to the end-point read-out of labeled techniques.



Figure 1.2: A microtiter plate is a standard tool in biomolecular research, and consists of small wells in which assays such as ELISA can be performed.

(small test tubes) of a microtiter plate (Figure 1.2). The color change indicative for a positive assay outcome can be interpreted qualitatively without read-out equipment, or quantitatively by measuring the optical transmission. While this basic platform for labeled detection only allows measuring a single protein in each sample, several techniques exist to scale to highly multiplexed measurements. A common technique is that of protein microarrays, glass plates on which different capture agents, such as antibodies, are immobilized in separate spots ordered in an array that can be imaged using microscopy. In this way, hundreds of different proteins can be monitored in each well of a microtiter plate [6]. Labeled assays can also be applied on the surface of microbeads in solution, providing another approach for highly multiplexed sensing [7].

1.2 Label-free biosensing

While labeled techniques can attain limits of detection down to the single-molecule level [8], they have several practical drawbacks. First, labeling and sandwich assays only provide end-point read-out, and do not allow continuous, real-time monitoring of molecular interactions [9], thus losing information on the binding kinetics and affinity. Second, the most selective sandwich-type assays require two high-affinity capture agents that recognize distinct and non-overlapping target epitopes, which often limits the development of highly multiplexed assays, and increases the cost and development time [10, 11]. Third, the required washing in-between different steps of the assay often increase the required sample

preparation, and can reduce the effective throughput.

Therefore, label-free affinity biosensors lately receive a lot of attention. They consist of a transducer with receptor molecules immobilized on its surface (Figure 1.1(b)) that directly responds to a selective affinity interaction between analyte molecules and the immobilized receptor molecules through the inherent optical, electrical or mechanical properties of the analyte. Multiple transducers with different receptor molecules provide an easy way to monitor multiple parameters in a highly multiplexed assay. In contrast with labeled techniques, many label-free methods allow to continuously monitor the affinity reaction, providing highly quantitative measures on the concentration, affinity and binding kinetics. Moreover, label-free assays require almost no sample preparation, decreasing the cost and enhancing throughput. The assay development is also significantly simplified, especially for highly multiplexed assays, since only one recognition element is required for each analyte.

1.3 State-of-the-art label-free technologies

There are many different label-free technologies, and an overview of the most promising ones is described by A.J. Qavi et al. [11] and M. Nirschl et al. [12]. This section highlights some of the most prominent technologies.

Currently the most widespread label-free technology is *surface plasmon resonance* (SPR) [13, 14], which directly measures the local refractive index change induced by biomolecular interactions at a gold surface using surface plasmon waves, charge density oscillations that can be excited optically. The best limits of detection (typically around 0.1 pg/mm^2 for protein interactions [12]) are obtained when interrogating the sensor with angular or wavelength spectroscopy, but then only up to ten measurements can be performed simultaneously [13], limiting the degree of multiplexing and throughput. Intensity interrogation allows *SPR imaging*, where a camera monitors the broadband reflectance change of the gold surface with a spatial resolution down to $4 \mu\text{m}$ [15], making this technique scalable to tens of thousands of parallel measurements [16]. However, SPR imaging has a more than an order of magnitude worse limit of detection than SPR spectroscopy (5 pg/mm^2 for protein interactions [12, 13]), making it less suited for applications requiring highly quantitative measurements. Multiple companies have SPR label-free sensor systems, including *Biacore* (a division of *GE Healthcare*), *GWC Technologies*, *IBIS Technologies*,

Toyobo, GenOptics, SensiQ and Bio-rad.

Multiple technologies are emerging in the quest for a robust and practical technology that can deliver limits of detection that rival that of SPR spectroscopy (0.1 pg/mm^2), while allowing a high throughput and degree of multiplexing with small fluidic sample consumption.

A commonly applied optical technology is *reflectometric interference spectroscopy* (RIfS), which measures biomolecular interactions at a surface through the induced refractive index change using a Michelson interferometer configuration. Its self-referencing makes it noise-tolerant, and moreover its more flexible read-out compared to SPR imaging makes it easier to integrate in a system, e.g. in the optical fiber probe of the company *ForteBio* and the array format of *Biametrics*. While this technology reaches the same degree of multiplexing and throughput as SPR imaging, it does not significantly improve the limit of detection (1 pg/mm^2 for protein interactions [12]).

Optical diffraction gratings can also measure refractive index changes induced by molecular interactions through a shift of the diffraction wavelength in a fixed direction. They can be mass produced cost-effectively from continuous sheets of plastic film by imprinting, and can be incorporated into standard microtiter plates [17]. Commercial systems for high-throughput cell-based assays and drug development are offered by *SRU Biosystems* and *Corning*. However, simultaneous interrogation of many wells of the microtiter plate in parallel requires optical imaging that only offers end-point read-out [17], instead of the real-time binding curves necessary for analysis of binding kinetics and affinity. Additionally, no highly multiplexed quantitative proteomics at clinically relevant limits of detection has been reported to date.

Electrochemical label-free sensors [18], such as *electrochemical impedance spectroscopy* and field effect transistor sensors based on *silicon nanowires* and *carbon nanotubes*, are well-suited for highly integrated systems. However, their performance often deteriorates at physiological ionic strengths (0.15 M), requiring desalting of the sample prior to the measurement [19].

Microcantilevers convert molecular interactions into mechanical motion on the nanometer scale, and also offer a platform for highly multiplexed label-free biosensing [9]. The best values for the limit of detection are achieved when optically interrogating the mechanical movement of the cantilever, with demonstrated protein measurements at clinically relevant concentrations (0.2 ng/ml [20]) for static measurements, and even down

to 10 pg/ml when dynamically measuring the mechanical resonance frequency change [21]. However, the optical interrogation through the fluidic system might be cumbersome, and more practical electrical interrogation with integrated piezoelectric materials cannot yet attain the same values for the limit of detection. Small arrays of eight microcantilever label-free biosensors are commercially offered by *Cantion* and *Concentris*.

1.4 Silicon photonic ring resonator label-free biosensors

In analogy to electronic integrated circuits, photonic integrated circuits combine and miniaturize optical functions, such as (laser) sources, detectors and filters, on a chip that can preferably be mass manufactured at high quality using optical lithography and etching. They are commonly applied in optical fiber communication networks. A waveguide that guides light over the chip by total internal reflection is the principal component, and consists of a high-refractive-index core surrounded by a low-refractive-index cladding. Guided modes are mainly confined in the core, with exponentially decaying evanescent tails in the cladding.

A photonic ring resonator consists of a waveguide that is folded back on itself to form a closed loop in which light resonates at effective wavelengths that fit an integer number of times in the loop. At least one access waveguide is positioned close to the ring resonator to couple light to and from the resonator through evanescent wave coupling. It connects the ring to a (possibly off-chip) source and detector. At the resonance wavelengths, light in the access waveguide destructively interferes with light coupled back from the ring resonator, causing sharp dips in the transmission spectrum. Ring resonators are well-known photonic components [22–24] that are applicable as filters in wavelength division multiplexed networks [25], as delay elements in optical buffers [26], and when combined with active materials also as laser cavities [27, 28] and modulators [29]. Section 2.2 in chapter 2 details their operation.

A ring resonator label-free biosensor directly measures selective affinity interactions between analyte molecules and receptor molecules immobilized on the ring waveguide surface (Figure 1.3(a)). Since most biological molecules (proteins, DNA, ...) have a refractive index (around 1.45) larger than that of the aqueous solvent (around 1.31), this molecular binding locally increases the refractive index in the range of the evanescent field

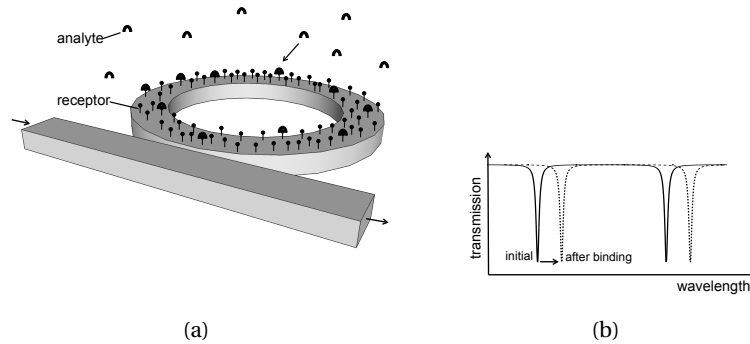


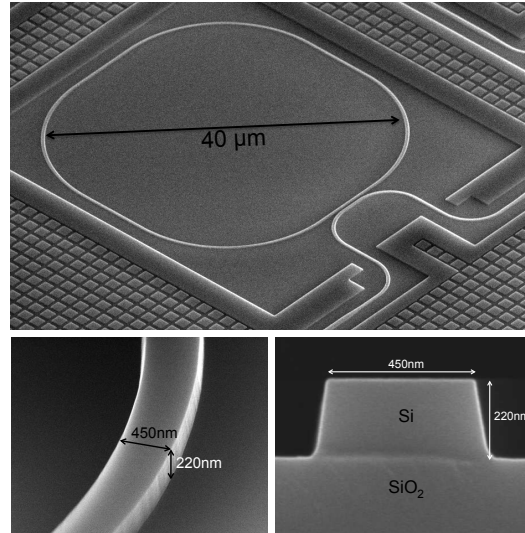
Figure 1.3: A ring resonator label-free biosensor consists of a waveguide with a chemically modified surface that presents receptor molecules that are selective to the analyte. Analyte molecules, if present in a fluidic sample, diffuse to the sensor and bind to the receptors, increasing the refractive index in the range of the evanescent field of the ring resonator waveguide. The consequent shift of the resonance wavelength is a measure for the concentration of the analyte, and the kinetics and affinity of the biochemical reaction.

of the waveguide mode. The resulting phase change of the mode induces measurable shifts of the resonance wavelengths of the ring, which are continuously monitored over time and which give information on the analyte concentration, affinity between the molecules and the kinetics of the biochemical reaction.

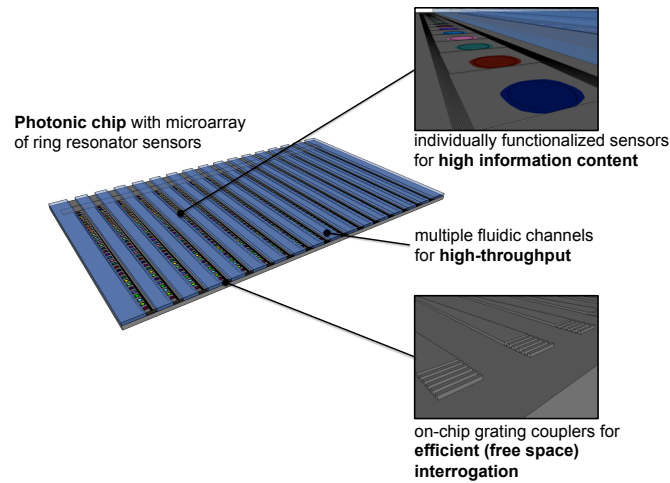
1.4.1 Assets and drawbacks

Silicon ring resonator label-free biosensors have many assets.

First, they consist of waveguides (Figure 1.4(a)) with a silicon core with high refractive index (3.47 at $1.55\ \mu\text{m}$ wavelength) separated from a silicon substrate by a buried oxide layer with low refractive index (1.44 at $1.55\ \mu\text{m}$ wavelength). The sensor benefits from this large refractive index contrast twice. In the first place, the ring sensors can be made very compact (typically less than $100\ \mu\text{m}$ diameter, but down to $5\ \mu\text{m}$ diameter is possible) to form *a dense label-free sensor array that enables high-throughput and highly multiplexed sensing*. In the second place, the ring waveguide's rapidly decaying evanescent field (in the order of 50 nm penetration depth instead of the hundreds of nanometers for SPR sensors [30]) overlaps very well with biomolecular interactions, providing a *high signal-to-noise ratio*.



(a)



(b)

Figure 1.4: (a) Silicon-on-insulator photonic ring resonator sensors entirely consist of high-refractive index contrast waveguides, and can therefore be made very compact. (b) Hence they can be incorporated in a dense array that allows a high-throughput, e.g. by flowing multiple samples in parallel over the chip. They also offer high information content assays by chemically modifying individual sensors differently with a molecular printer. On-chip grating couplers provide efficient interfaces with the read-out instrument.

Second, efficient broadband grating couplers and access waveguides allow decoupling the location of the sensor from that of the interface to the light source and detector, providing a lot of *flexibility for the instrument design*.



Figure 1.5: High-quality silicon photonic chips can be manufactured using the facilities already invested in by the electronics industry (a), providing the means to fabricate them at wafer-scale (b) in high volume at a low cost per chip. Images adopted from the IBM-website [31]

Third, silicon ring resonators are also *highly manufacturable*. Silicon is the material of choice in consumer electronics, for which industry invested tremendously in fabrication facilities (Figure 1.5). Silicon photonic circuits can be fabricated using the same facilities, especially those for optical lithography and dry etching [32, 33], so that their manufacturing can be scaled to high volumes at wafer scale using very reliable processes. This enables high-quality sensor chips that are cheap enough to be disposable, meaning that the chip is only used once to avoid complex cleaning of the sensor surface after use. Moreover, ring resonators entirely consist of standard waveguides, and can therefore reliably be made with large quality factor, large extinction and low insertion loss.

Fourth, the native oxide of silicon is standard glass, as used in standard protein arrays. Slightly oxidizing the sensor's top surface makes it *very suited for biochemical surface modification*.

Fifth, silicon photonics has the *prospect of further integration* of filters, electronics, sources and detectors. This opens the perspective of portable instruments, capable of high-end point-of-care diagnostics.

Nevertheless, silicon ring resonator label-free sensors also have draw-

backs. First, silicon is only transparent to light with wavelengths starting in the near-infrared, where sources and detectors are more expensive than in the visible light region, and where additionally water absorbs light significantly, typically dominating the propagation loss in the ring resonator waveguide (section 2.1.2 in chapter 2). Second, the high refractive index contrast causes scattering at surface roughness in the waveguides, possibly giving rise to aberrations in the transmission spectrum [34].

1.4.2 State-of-the-art

Since R. W. Boyd and J. E. Heebner [35] introduced the idea of using an integrated (disk) resonator for direct label-free detection of biomolecules in 2001, several research groups contributed to the experimental characterization. In 2006, A. Yalcin et al. [36] first demonstrated label-free detection of a model protein with a glass ring resonator sensor, quickly followed by a demonstration of the concept on silicon ring resonator sensors by K. De Vos et al. [37] from our research group and Ramachandran et al. [38]. Shortly after, multiple groups, including ours, presented different methods for multiplexed label-free detection of proteins [39–41] in an array format that does not compromise the performance of each of the sensors. Currently, the start-up company *Genalyte* [42] is launching a multiplexed label-free biosensor platform based on silicon ring resonators [43]. In collaboration with this company, the group of R. C. Bailey recently made extensive contributions to the characterization of the platform [30, 39, 44–51]. M.S. Luchansky et al. [52] thoroughly reviewed photonic biosensors with large quality factor, including silicon ring resonators. The remainder of this section reviews the state-of-the-art results achieved by the Bailey group.

Luchansky et al. [30] measured 1.5 pg/mm^2 limit of detection, which is not a significant improvement over SPR imaging (5 pg/mm^2 [12, 13]). However, the corresponding absolute mass limit of detection is as low as 125 ag due to the small sensor size, proving that the sensor only requires small fluidic samples.

Washburn et al. [44] demonstrated direct label-free quantification of a cancer biomarker (carcinoembryonic antigen) with a silicon ring resonator sensor over 3-log dynamic range down to 2 ng/ml in buffer, which is comparable to commercial ELISA-kits. However, non-specific binding deteriorated the limit of detection in undiluted serum to 25 ng/ml , still insufficient for clinical applications. Nevertheless, the total assay time

(under 30 min, including sensor calibration) compared favorably with that of ELISA (over 3 hours), and moreover the assay can be scaled to a multiplexed measurement of five biomarkers without compromise on the sensor performance [39]. Luchansky et al. [45] enhanced the dynamic range (6-logs) and limit of detection (down to 30 pg/ml in diluted serum) using a three-step sandwich assay with micro-bead signal amplification.

Cytokines, small proteins that play an important role in intercellular communication, are more difficult to quantify than antibodies due to their smaller size (5 - 40 kDa for cytokines instead of 150kDa for antibodies) [53] and low concentrations (pg/mL to ng/mL) [54]. Luchansky and Bailey [47] measured the temporal secretion patterns of T-cells using 4-plex real-time binding analyses with 32 silicon ring resonators, albeit after incubation of the sample with detection antibodies to amplify the sensor signal.

Qavi et al. [48] quantified 15-mer DNA across 3 orders of magnitude (nanomolar to micromolar) down to 2 nM in a 10 min direct label-free assay, and employed the sensor's real-time binding curve to distinguish single nucleotide polymorphism by differences in the dissociation kinetics. The authors also demonstrated the simultaneous direct label-free detection of 4 miRNAs [49] down to 2 nM, and enhanced the limit of detection down to 10 pM by amplifying the signal with antibodies [50].

Finally, McClellan and Bailey recently employed the sensor for virus detection in agricultural applications [51].

1.4.3 Application domains

Label-free sensors in general, and silicon ring resonator sensors in particular, have the potential to improve efficiency in health care research. This includes studying the molecular basis of diseases and identifying biomarkers, molecules in a patient's sample whose concentrations reflect the presence or severity of a disease. Especially its capability to monitor many different molecules, such as proteins, DNA, RNA and viruses, simultaneously in real time at high throughput can make a difference.

Also in drug development (Figure 1.6), silicon photonic ring resonator label-free biosensors can help. Healthcare reform, tougher regulatory hurdles and patent expiry of drugs are putting the pharmaceutical industry under increasing pressure, with R&D costs continuing to increase but the numbers of new medicines remaining static. It is clear that for companies to remain competitive, they not only need to improve cycle times using

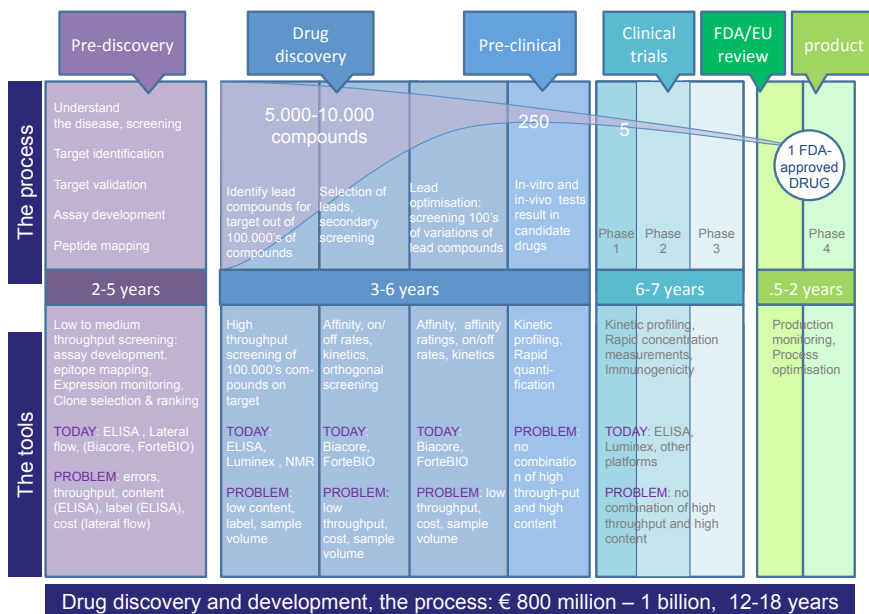


Figure 1.6: The drug development process [55], with indication of the currently used instruments [56, 57]

advanced high-throughput equipment, but also need to identify technologies that provide more information on the biomolecular interactions early in the process. The efficiency in the drug pre-discovery and discovery phase can be improved, both in cost and timing, using more relevant assays, such as real-time label-free techniques that offer a higher degree of multiplexing (high-content) in combination with a high throughput. This can substantially shorten the drug discovery phase (Figure 1.6) and reduce the process cost of bringing a new drug to the market.

In hospitals, biomarkers measurements can be used for presymptomatic diagnostics, disease prognosis and can indicate appropriate treatments. Eventually this can lead to a treatment that is adapted to the patient in personalized medicine [58]. Silicon ring resonator sensors are well-suited for integration in a laboratory-on-a-chip, which combines microfluidic sample preparation and biomarker detection in a (trans)portable device that can be used at the point-of-care.

Finally, they can also be applied for applications other than healthcare, such as on-site continuous environmental monitoring [59] and food process control [60].

1.5 This thesis

In recent years, silicon ring resonator label-free biosensors have proven to be excellent sensors, comparing favorably with many other labeled and label-free sensing techniques. However, many aspects still need improvement in order to convince a large user-base. While there are many opportunities in the development of specific assays, we think there is also still room for improvements in the optical platform. Being part of the *Photonics Research Group* of Ghent University - imec, that has many years of experience in silicon photonics, we are well-positioned to explore methods to improve the sensor platform at the level of the silicon ring resonator transducer.

First, straightforward direct label-free assays are often less specific than sandwich assays, since the former only employ a single biomolecular recognition element. Therefore, we assessed using a second waveguide mode in the ring resonator sensor to provide additional information on the biomolecular interactions (chapter 3). This has the prospect of distinguishing between specific and non-specific interactions and enabling measurements of conformational changes.

Second, the limit of detection of current ring resonator sensors (1.5 pg/mm^2 [30]) is only slightly better than that of more mature and widespread SPR imaging systems (5 pg/mm^2 [12, 13]), and is worse than that of (low-plex and low-throughput) SPR spectroscopy systems (0.1 pg/mm^2 [12]). Hence, we derived an approximate formula for the limit of detection that can serve as a figure of merit for ring resonator transducers, and proposed improvements of the ring resonator design (chapter 2). We also enhanced the light-matter interaction with a slot waveguide, and assessed its impact on the limit of detection (chapter 4). Additionally, we applied the Vernier-principle in a cascade of two ring resonator sensors that optically compensates temperature and refractive index noise, and enhances the wavelength sensitivity up to two orders of magnitude (chapter 5).

Third, interrogating small wavelength shifts of the sharp ring resonances complicates the read-out instrument and increases the cost by requiring an external cavity wavelength-tunable laser. Therefore, we integrated a spectral filter on the Vernier-cascade sensor chip that allows interrogation with a cheaper broadband light source, and moreover improves the temporal resolution of the binding curve (chapter 6).

1.6 Publications

1.6.1 Patent applications

1. P. Bienstman, T. Claes, W. Bogaerts, *Vernier-biosensor - device* GB Provisional 1117649.2
2. P. Bienstman, T. Claes, W. Bogaerts, *Vernier photonic sensor data-analysis* US Provisional 13/271,875
3. P. Bienstman, T. Claes, K. De Vos, J.-W. Hoste, W. Bogaerts, *Methods and systems for biosensing* US Provisional 61/478,103

1.6.2 International journal publications

1. L. Wang, J. Ren, X. Han, T. Claes, X. Jian, P. Bienstman, R. Baets, M. Zhao, G. Morthier, *A Label-Free Optical Biosensor Built on a Low Cost Polymer Platform*, accepted for publication in IEEE Photonics Journal.
2. K. Van Acoleyen, J. Roels, P. Mechet, T. Claes, D. Van Thourhout, R. Baets, *Ultra-compact phase modulator based on a cascade of NEMS-operated slot waveguides fabricated in Silicon-On-Insulator*, IEEE Photonics Journal, vol. 4(3), pp. 779-788, June 2012.
3. W.A.D. De Cort, J. Beeckman, T. Claes, K. Neyts, R. Baets, *Wide Tuning of Silicon-On-Insulator Ring Resonators with a Liquid Crystal Cladding*, Optics Letters, vol. 36(19), pp. 3876-3878, Sep. 2011.
4. T. Claes, W. Bogaerts, P. Bienstman, *Vernier-cascade label-free biosensor with integrated arrayed waveguide grating for wavelength interrogation with low-cost broadband source*, Optics Letters, vol. 36(17), pp. 3320-3322, Aug. 2011.
5. W. Bogaerts, P. De Heyn, T. Van Vaerenbergh, K. De Vos, S. Selvaraja, T. Claes, P. Dumon, P. Bienstman, D. Van Thourhout, R. Baets, *Silicon Microring Resonators* (invited), Lasers and Photonics Review, Jun. 2011.
6. C. Lerma Arce, K. De Vos, T. Claes, K. Komorowska, D. Van Thourhout, P. Bienstman, *Silicon-on-insulator microring resonator sensor integrated on an optical fiber facet*, IEEE Photonics Technology Letters, Apr. 2011.

7. T. Claes, W. Bogaerts, P. Bienstman, *Experimental characterization of a silicon photonic biosensor consisting of two cascaded ring resonators based on the Vernier-effect and introduction of a curve fitting method for an improved detection limit*, Optics Express, vol. 18(22), pp. 22747–22761, Oct. 2010.
8. K. De Vos, Jordi Girones Molera, T. Claes, Y. De Koninck, Stepan Popelka, Etienne Schacht, R. Baets, P. Bienstman, *Multiplexed antibody detection with an array of silicon-on-insulator microring resonators*, IEEE Photonics Journal, vol. 1(4), pp. 225-235, Oct. 2009.
9. T. Claes, J. Girones Molera, K. De Vos, E. Schacht, R. Baets, P. Bienstman, *Label-Free Biosensing With a Slot-Waveguide-Based Ring Resonator in Silicon on Insulator*, IEEE Photonics Journal, vol. 1(3), IEEE, pp. 197-204, Sep. 2009.
10. J. Schrauwen, J. Van Lysebetsens, T. Claes, K. De Vos, P. Bienstman, D. Van Thourhout, R. Baets, *Focused-ion-beam fabrication of slots in silicon waveguides and ring resonators*, IEEE Photonics Technology Letters, vol. 20(23), p. 2004, Dec. 2008.
11. F. Van Laere, T. Claes, J. Schrauwen, S. Scheerlinck, W. Bogaerts, D. Taillaert, L. O’Faolain, D. Van Thourhout, R. Baets, *Compact Focusing Grating Couplers for Silicon-on-Insulator Integrated Circuits*, IEEE Photonics Technology Letters, vol. 19(23), pp. 1919-1921, Dec. 2007.

1.6.3 International conference contributions

1. T. Claes, D. Vermeulen, P. De Heyn, K. De Vos, G. Roelkens, D. Van Thourhout, P. Bienstman, *Towards a silicon dual polarization ring resonator sensor for multiplexed and label-free structural analysis of molecular interactions*, Proceedings of Europt(r)ode XI, Barcelona, Spain, Apr. 2012.
2. C. Lerma Arce, T. Claes, K. Komorowska, P. Bienstman, *Silicon nanophotonics sensors integrated in reaction tubes*, Proceedings of Europt(r)ode XI, Barcelona, Spain, Jan. 2012.
3. P. Bienstman, T. Claes, C. Lerma Arce, W. Bogaerts, K. Komorowska, D. Van Thourhout, *Novel Ring Resonator Based Biosensors* (invited), CLEO Europe, Munchen, Germany, pp. jsiv1.3-sun, Nov. 2011.

4. W.A.D. De Cort, J. Beeckman, T. Claes, K. Neyts, R. Baets, *Widely Tunable Silicon-On-Insulator Ring Resonators with a Liquid Crystal Cladding*, IEEE Photonics 2011 Conference (IPC11), Arlington, Virginia, pp. 541-542, Oct. 2011.
5. K. Van Acoleyen, J. Roels, T. Claes, D. Van Thourhout, R. Baets, *NEMS-based optical phase modulator fabricated on Silicon-On-Insulator*, 8th International Conference on Group IV Photonics, vol. FC6, London, United Kingdom, pp. 371-373, Sep. 2011.
6. T. Claes, W. Bogaerts, P. Bienstman, *Vernier-cascade silicon photonic label-free biosensor with very large sensitivity and low-cost interrogation*, Proceedings of SPIE 8099, San Diego, United States, Aug. 2011.
7. D. Hill, N. Sandström, K. Gylfason, E. Carlborg, M. Karlsson, T. Moh, T. Haraldsson, H. Sohlström, A. Russom, Göran Stemme, W. van der Wijngaart, T. Claes, P. Bienstman, A. Kazmierczak, F. Dortu, M. J. Banuls Polo, A. Maquieira Catala, G. M. Kresbach, L. Vivien, J. Popplewell, G. Ronan, C. A. Barrios, *Microfluidic and transducer technologies for lab on a chip applications*, 32nd Annual International Conference of IEEE Engineering in Medicine and Biology Society (EMBC, Buenos Aires, Argentina, pp. 305-307, Aug. 2010.
8. K. De Vos, J. Girones, T. Claes, E. Schacht, R. Baets, P. Bienstman, *High throughput label-free biosensing with silicon-on-insulator microring resonators*, Europt(r)ode X , Czech Republic, Mar. 2010.
9. G. Yurtsever, K. De Vos, T. Claes, P.P.P. Debackere, P. Bienstman, R. Baets, *Photonic Biosensors in Silicon-on-Insulator* (invited), 2nd International Conference On Silicon Photonics, Cambridge, United States, Jan. 2010.
10. K. De Vos, P.P.P. Debackere, T. Claes, J. Girones, W.A.D. De Cort, E. Schacht, R. Baets, P. Bienstman, *Label-free biosensors on silicon-on-insulator optical chips* (invited), SPIE Optics and Photonics, vol. 7397(37), San Diego, United States, Jul. 2009.
11. G. Roelkens, D. Taillaert, F. Van Laere, D. Vermeulen, J. Schrauwen, S. Scheerlinck, T. Claes, W. Bogaerts, P. Dumon, S. Selvaraja, D. Van Thourhout, R. Baets, *Interfacing optical fibers and high refractive index contrast waveguide circuits using diffractive grating couplers* (invited), Photonics West, SPIE, San Jose, United States, Apr. 2009.
12. P. Bienstman, K. De Vos, T. Claes, P.P.P. Debackere, R. Baets, J.

Girones, E. Schacht, *Biosensors in silicon on insulator*, Proceedings of SPIE Photonics West 2009-OPTO: Integrated Optoelectronics Devices, vol. 7220, San Jose, California, United States, p. 722000 (9 pages), Jan. 2009.

13. J. Schrauwen, T. Claes, D. Van Thourhout, R. Baets, *Focused-ion-beam fabrication of slots in silicon waveguides and ring resonators*, Proceedings Annual Symposium of the IEEE/LEOS Benelux Chapter, 2008, Twente, Netherlands, pp. 55-58, Nov. 2008.
14. T. Claes, J. Girones, K. De Vos, P. Bienstman, R. Baets, *Label-free biosensing with silicon-on-insulator slotted racetrack resonator*, Proceedings Annual Symposium of the IEEE/LEOS Benelux Chapter, 2008, Twente, Netherlands, pp. 23-26, Nov. 2008.

References

- [1] MJ van de Vijver, YD He, LJ van 't Veer, H Dai, AAM Hart, DW Voskuil, GJ Schreiber, JL Peterse, C Roberts, MJ Marton, M Parrish, D Atsma, A Witteveen, A Glas, L Delahaye, T van der Velde, H Bartelink, S Rodenhuis, ET Rutgers, SH Friend, and R Bernards. *A gene-expression signature as a predictor of survival in breast cancer*. New England Journal of Medicine, 347(25):1999–2009, December 2002.
- [2] S Hanash. *Disease proteomics*. Nature, 422(6928):226–232, March 2003.
- [3] Sandipan Ray, Panga J. Reddy, Rekha Jain, Kishore Gollapalli, Aliasgar Moiyadi, and Sanjeeva Srivastava. *Proteomic technologies for the identification of disease biomarkers in serum: Advances and challenges ahead*. Proteomics, 11(11):2139–2161, JUN 2011.
- [4] RM Lequin. *Enzyme Immunoassay (EIA)/Enzyme-Linked Immunosorbent Assay (ELISA)*. Clinical Chemistry, 51(12):2415–2418, December 2005.
- [5] E Mylonakis, M Paliou, M Lally, TP Flanigan, and JD Rich. *Laboratory testing for infection with the human immunodeficiency virus: Established and novel approaches*. American Journal of Medicine, 109(7):568–576, November 2000.
- [6] UB Nielsen and BH Geierstanger. *Multiplexed sandwich assays in microarray format*. Journal of Immunological Methods, 290(1-2):107–120, July 2004.
- [7] M. T. Arellano-Garcia, S. Hu, J. Wang, B. Henson, H. Zhou, D. Chia, and D. T. Wong. *Multiplexed immunobead-based assay for detection of oral cancer protein biomarkers in saliva*. Oral Diseases, 14(8):705–712, November 2008.
- [8] S Schultz, DR Smith, JJ Mock, and DA Schultz. *Single-target molecule detection with nonbleaching multicolor optical immunolabels*. Proceedings of the National Academy of Sciences of the United States of America, 97(3):996–1001, February 2000.
- [9] J. L. Arlett, E. B. Myers, and M. L. Roukes. *Comparative advantages of mechanical biosensors*. Nature Nanotechnology, 6(4):203–215, APR 2011.

- [10] ML Phelan and S Nock. *Generation of bioreagents for protein chips*. *Proteomics*, 3(11):2123–2134, November 2003.
- [11] Abraham J. Qavi, Adam L. Washburn, Ji-Yeon Byeon, and Ryan C. Bailey. *Label-free technologies for quantitative multiparameter biological analysis*. *Anal. Bioanal. Chem.*, 394(1):121–135, May 2009.
- [12] Martin Nirschl, Florian Reuter, and Janos Vörös. *Review of Transducer Principles for Label-Free Biomolecular Interaction Analysis*. *Biosensors*, 1(3):70–92, 2011.
- [13] Jiri Homola. *Surface plasmon resonance sensors for detection of chemical and biological species*. *Chemical Reviews*, 108(2):462–493, Feb 2008.
- [14] Richard B M Schasfoort and Anna J Tudos, editors. *Handbook of surface plasmon resonance*. RSCPublishing, 2008.
- [15] Charles T. Campbell and Gibum Kim. *SPR microscopy and its applications to high-throughput analyses of biomolecular binding events and their kinetics*. *Biomaterials*, 28(15):2380–2392, May 2007.
- [16] Christina Boozer, Gibum Kim, Shuxin Cong, HannWen Guan, and Timothy Londergan. *Looking towards label-free biomolecular interaction analysis in a high-throughput format: a review of new surface plasmon resonance technologies*. *Current Opinion In Biotechnology*, 17(4):400–405, August 2006.
- [17] Brian T. Cunningham and Lance Laing. *Microplate-based, label-free detection of biomolecular interactions: applications in proteomics*. *Expert Review of Proteomics*, 3(3):271–281, June 2006.
- [18] Dorothee Grieshaber, Robert MacKenzie, Janos Voeroes, and Erik Reimhult. *Electrochemical biosensors - Sensor principles and architectures*. *Sensors*, 8(3):1400–1458, March 2008.
- [19] GF Zheng, F Patolsky, Y Cui, WU Wang, and CM Lieber. *Multiplexed electrical detection of cancer markers with nanowire sensor arrays*. *Nature Biotechnology*, 23(10):1294–1301, October 2005.
- [20] GH Wu, RH Datar, KM Hansen, T Thundat, RJ Cote, and A Majumdar. *Bioassay of prostate-specific antigen (PSA) using microcantilevers*. *Nature Biotechnology*, 19(9):856–860, September 2001.
- [21] JH Lee, KS Hwang, J Park, KH Yoon, DS Yoon, and TS Kim. *Immunoassay of prostate-specific antigen (PSA) using resonant frequency shift*

- of piezoelectric nanomechanical microcantilever*. Biosensors & Bioelectronics, 20(10):2157–2162, April 2005.
- [22] D. G. Rabus. *Integrated Ring Resonators*. Springer series in optical sciences, 2007.
- [23] John Heebner, Rohit Grover, and Tarek Ibrahim. *Optical microresonators*. Springer series in optical sciences, 2008.
- [24] Wim Bogaerts, Peter De Heyn, Thomas Van Vaerenbergh, Katrien De Vos, Shankar Kumar Selvaraja, Tom Claes, Pieter Dumon, Peter Bienstman, Dries Van Thourhout, and Roel Baets. *Silicon microring resonators*. Laser & Photonics Reviews, 6(1):47–73, January 2012.
- [25] B.E. Little, J.S. Foresi, G. Steinmeyer, E.R. Thoen, S.T. Chu, H.A. Haus, E.P. Ippen, L.C. Kimerling, and W. Greene. *Ultra-compact Si-SiO₂ microring resonator optical channel dropping filters*. IEEE Photonics Technology Letters, 10(4):549–551, apr 1998.
- [26] Fengnian Xia, Lidija Sekaric, and Yurii Vlasov. *Ultrapact optical buffers on a silicon chip*. Nature Photonics, 1(1):65–71, JAN 2007.
- [27] Brian R. Koch, Alexander W. Fang, Oded Cohen, and John E. Bowers. *Mode-locked silicon evanescent lasers*. Opt. Express, 15(18):11225–11233, Sep 2007.
- [28] S. L. McCall, A. F. J. Levi, R. E. Slusher, S. J. Pearton, and R. A. Logan. *Whispering-gallery mode microdisk lasers*. Applied Physics Letters, 60(3):289–291, January 1992.
- [29] Qianfan Xu, Sasikanth Manipatruni, Brad Schmidt, Jagat Shakya, and Michal Lipson. *12.5 Gbit/s carrier-injection-based silicon micro-ring silicon modulators*. Opt. Express, 15(2):430–436, Jan 2007.
- [30] Matthew S. Luchansky, Adam L. Washburn, Teresa A. Martin, Muza-mmil Iqbal, L. Cary Gunn, and Ryan C. Bailey. *Characterization of the evanescent field profile and bound mass sensitivity of a label-free silicon photonic microring resonator biosensing platform*. Biosensors and Bioelectronics, 26(4):1283 – 1291, 2010.
- [31] www.ibm.com.
- [32] Shankar Kumar Selvaraja, Patrick Jaenen, Wim Bogaerts, Dries Van Thourhout, Pieter Dumon, and Roel Baets. *Fabrication of Photonic Wire and Crystal Circuits in Silicon-on-Insulator Using 193-nm Optical Lithography*. J. Lightw. Technol., 27(18):4076–4083, 2009.

- [33] Shankar Kumar Selvaraja. *Wafer-Scale Fabrication Technology for Silicon Photonic Integrated Circuits*. PhD thesis, Universiteit Gent, 2011.
- [34] F. Morichetti, a. Canciamilla, M. Martinelli, a. Samarelli, R. M. De La Rue, M. Sorel, and a. Melloni. *Coherent backscattering in optical microring resonators*. Applied Physics Letters, 96(8):081112, 2010.
- [35] RW Boyd and JE Heebner. *Sensitive disk resonator photonic biosensor*. Applied Optics, 40(31):5742–5747, NOV 1 2001.
- [36] A Yalcin, KC Papat, JC Aldridge, TA Desai, J Hryniewicz, N Chbouki, BE Little, O King, V Van, S Chu, D Gill, M Anthes-Washburn, and MS Unlu. *Optical sensing of biomolecules using microring resonators*. IEEE Journal of Selected Topics in Quantum Electronics, 12(1):148–155, JAN-FEB 2006.
- [37] Katrien De Vos, Irene Bartolozzi, Etienne Schacht, Peter Bienstman, and Roel Baets. *Silicon-on-Insulator microring resonator for sensitive and label-free biosensing*. Optics Express, 15(12):7610–7615, JUN 11 2007.
- [38] A. Ramachandran, S. Wang, J. Clarke, S. J. Ja, D. Goad, L. Wald, E. M. Flood, E. Knobbe, J. V. Hryniewicz, S. T. Chu, D. Gill, W. Chen, O. King, and B. E. Little. *A universal biosensing platform based on optical micro-ring resonators*. Biosensors & Bioelectronics, 23(7):939–944, FEB 28 2008.
- [39] Adam L. Washburn, Matthew S. Luchansky, Adrienne L. Bowman, and Ryan C. Bailey. *Quantitative, Label-Free Detection of Five Protein Biomarkers Using Multiplexed Arrays of Silicon Photonic Microring Resonators*. Analytical Chemistry, 82(1):69–72, Jan 2010.
- [40] K. De Vos, J. Girones, T. Claes, Y. De Koninck, S. Popelka, E. Schacht, R. Baets, and P. Bienstman. *Multiplexed Antibody Detection With an Array of Silicon-on-Insulator Microring Resonators*. IEEE Photon. J., 1(4):225–235, Oct. 2009.
- [41] D. X. Xu, M. Vachon, A. Densmore, R. Ma, A. Delage, S. Janz, J. Lapointe, Y. Li, G. Lopinski, D. Zhang, Q. Y. Liu, P. Cheben, and J. H. Schmid. *Label-free biosensor array based on silicon-on-insulator ring resonators addressed using a WDM approach*. Opt. Lett., 35(16):2771–2773, Aug 2010.
- [42] www.genalyte.com.

- [43] Muzammil Iqbal, Martin A. Gleeson, Bradley Spaugh, Frank Tybor, William G. Gunn, Michael Hochberg, Tom Baehr-Jones, Ryan C. Bailey, and L. Cary Gunn. *Label-Free Biosensor Arrays Based on Silicon Ring Resonators and High-Speed Optical Scanning Instrumentation*. IEEE J. Sel. Topics Quantum Electron., 16(3):654–661, May-June 2010.
- [44] Adam L. Washburn, L. Cary Gunn, and Ryan C. Bailey. *Label-Free Quantitation of a Cancer Biomarker in Complex Media Using Silicon Photonic Microring Resonators*. Analytical Chemistry, 81(22):9499–9506, 10 2009.
- [45] Matthew S. Luchansky, Adam L. Washburn, Melinda S. McClellan, and Ryan C. Bailey. *Sensitive on-chip detection of a protein biomarker in human serum and plasma over an extended dynamic range using silicon photonic microring resonators and sub-micron beads*. Lab on a Chip, 11(12):2042–2044, 2011.
- [46] Matthew S. Luchansky and Ryan C. Bailey. *Silicon Photonic Microring Resonators for Quantitative Cytokine Detection and T-Cell Secretion Analysis*. Analytical Chemistry, 82(5):1975–1981, MAR 1 2010.
- [47] Matthew S. Luchansky and Ryan C. Bailey. *Rapid, Multiparameter Profiling of Cellular Secretion Using Silicon Photonic Microring Resonator Arrays*. Journal of the American Chemical Society, 133(50):20500–20506, December 2011.
- [48] Abraham J Qavi, Thomas M Mysz, and Ryan C Bailey. *Isothermal Discrimination of Single-Nucleotide Polymorphisms via Real-Time Kinetic Desorption and Label-Free Detection of DNA Using Silicon Photonic Microring Resonator Arrays*. Analytical Chemistry, 83(17):6827–6833, September 2011.
- [49] Abraham J. Qavi and Ryan C. Bailey. *Multiplexed Detection and Label-Free Quantitation of MicroRNAs Using Arrays of Silicon Photonic Microring Resonators*. Angewandte Chemie, 49(27):4608–4611, 2010.
- [50] Abraham J. Qavi, Jared T. Kindt, Martin A. Gleeson, and Ryan C. Bailey. *Anti-DNA:RNA Antibodies and Silicon Photonic Microring Resonators: Increased Sensitivity for Multiplexed microRNA Detection*. Analytical Chemistry, 83(15):5949–5956, August 2011.
- [51] Melinda S. McClellan, Leslie L. Domier, and Ryan C. Bailey. *Label-free virus detection using silicon photonic microring resonators*. Biosensors & Bioelectronics, 31(1):388–392, January 2012.

-
- [52] Matthew S Luchansky and Ryan C Bailey. *High-q optical sensors for chemical and biological analysis*. *Anal Chem*, 84(2):793–821, Jan 2012.
- [53] JJ Haddad. *Cytokines and related receptor-mediated signaling pathways*. *Biochemical and Biophysical Research Communications*, 297(4):700–713, October 2002.
- [54] N. Leigh Anderson and Norman G. Anderson. *The Human Plasma Proteome*. *Molecular and Cellular Proteomics*, 1(11):845–867, 2002.
- [55] *Pharmaceutical Research and Manufacturers of America* (www.phrma.org).
- [56] MA Cooper. *Optical biosensors in drug discovery*. *Nature Reviews Drug Discovery*, 1(7):515–528, July 2002.
- [57] Matthew A. Cooper. *Optical biosensors: where next and how soon?* *Drug Discovery Today*, 11(23-24):1061 – 1067, 2006.
- [58] Ryan C. Bailey. *Informative diagnostics for personalized medicine*. *Nature Chemical Biology*, 6(12):857–859, DEC 2010.
- [59] KR Rogers. *Recent advances in biosensor techniques for environmental monitoring*. *Analytica Chimica Acta*, 568(1-2):222–231, May 2006.
- [60] Frances S. Ligler. *Perspective on Optical Biosensors and Integrated Sensor Systems*. *Analytical Chemistry*, 81(2):519–526, January 2009.

2

Silicon photonic ring resonator label-free biosensor platform

Multiplexed label-free bioassays with silicon ring resonator sensors entail probing a fluid with multiple sensors that are each sensitive to a different molecule in a selective way. It not only requires performant ring resonator transducers, but also biochemical surface modification of individual sensors on a chip, controlled delivery of fluids, and simultaneous and continuous optical interrogation (Figure 2.1). Several research groups [1–4], including ours [5–7], contributed to the different aspects of this multidisciplinary platform. The novel ring resonator transducers presented in this thesis fit in this larger framework, and understanding all its aspects is a prerequisite to the understanding of the following chapters.

Therefore, this chapter discusses the different aspects of a ring resonator platform, starting with the single-mode silicon waveguide of which most sensors in this thesis consist (section 2.1). Section 2.2 describes the operation of a ring resonator and presents an advantageous design and implementation in silicon for sensing. Section 2.3 explains the principles and figures of merit of evanescent field sensing with ring resonators, and

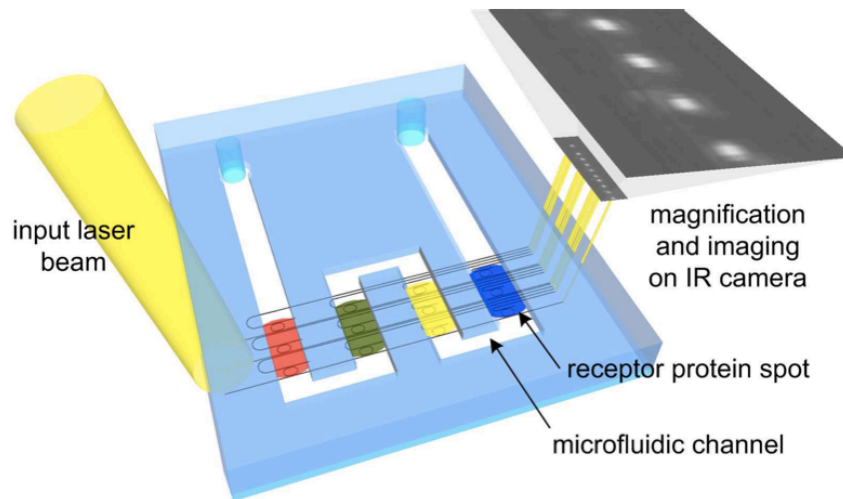


Figure 2.1: A multiplexed silicon ring resonator label-free biosensor platform, as pictured here according to the concept proposed by K. De Vos et al. [6] from our research group, typically comprises a microarray of ring resonator transducers that are each biochemically modified to be selective to a different analyte. A microfluidic channel can transport fluids to the sensor, and an off-chip instrument optically interrogates the sensor chip continuously.

introduces a formula for the limit of detection of the platform, a measure for the smallest quantity it can reliably detect. Section 2.5 studies how small ring and disk resonators can be made, targeting extremely dense label-free sensor arrays. Sections 2.6 and 2.7 summarize the methods for biochemical surface modification and fluidic sample delivery. Finally, section 2.8 provides more information on the interrogation of the sensors.

2.1 Silicon wire waveguides

Many silicon photonic components are developed for the wavelength region around $1.55 \mu\text{m}$, since there the propagation loss in silica fibers becomes minimal [8], making it a wavelength region that is of special interest to telecommunication applications. To profit from this experience, all devices presented in this thesis were also developed to operate at a wavelength of $1.55 \mu\text{m}$. The contrast between the refractive index of silicon (3.47) and silica (1.44) at this wavelength is very high (200%), which

allows to confine light in very compact wire waveguides that can be bent with very small radii (a few micrometer) without significant loss to create very dense photonic circuits. This section introduces the single-mode waveguide that will be used for most sensors presented in this thesis, and discusses its basic properties such as loss and dispersion.

2.1.1 Single-mode regime

Silicon-on-insulator (100) Unibond 200 mm wafers manufactured by *Soitec* [9] serve as the starting point for all sensor chips presented in this thesis. They consist of a 220 nm-thick lightly p-doped crystalline silicon layer that vertically confines light to a single mode, and that is separated from the silicon substrate by a 2 μm -thick buried amorphous silicon dioxide layer to reduce substrate leakage. Horizontal confinement of the optical mode is achieved by etching two parallel trenches of several micrometers wide, one at each side of the waveguide, through the complete 220 nm-thick silicon layer with reactive-ion etching, after patterning with optical lithography at the short wavelength of 193 nm. The chips are fabricated at wafer-scale through the European silicon photonics platform *ePIXfab* [10] with the facilities of *imec* in Leuven, Belgium. The fabrication process is detailed by S. Selvaraja et al. [11, 12]. For biosensing, the waveguide top cladding is an aqueous solution with low refractive index (1.31 at the wavelength of 1.55 μm [13]).

Depending on its width, the resulting waveguide (inset Figure 2.2) can guide multiple modes that either have a major magnetic field component along the transverse (horizontal) direction, called quasi transverse magnetic (quasi-TM) modes, or a major electric field component along the transverse direction, called transverse electric (quasi-TE) modes. Each mode propagates through the waveguide with a phase velocity $\frac{c}{n_{eff}}$, with c the speed of light in vacuum and n_{eff} the effective refractive index felt by that mode. When the effective refractive index is larger than the largest refractive index of the cladding (1.44 in this case), the mode is guided in the waveguide, and the guiding will be stronger with increasing values of the effective refractive index.

Especially in bends, power can be transferred between multiple guided modes, causing undesired interference effects that distort the transmission spectrum of components such as ring resonators. Therefore, waveguides are made narrow enough to only guide a single mode for each polarization. If the difference between the effective refractive index of the

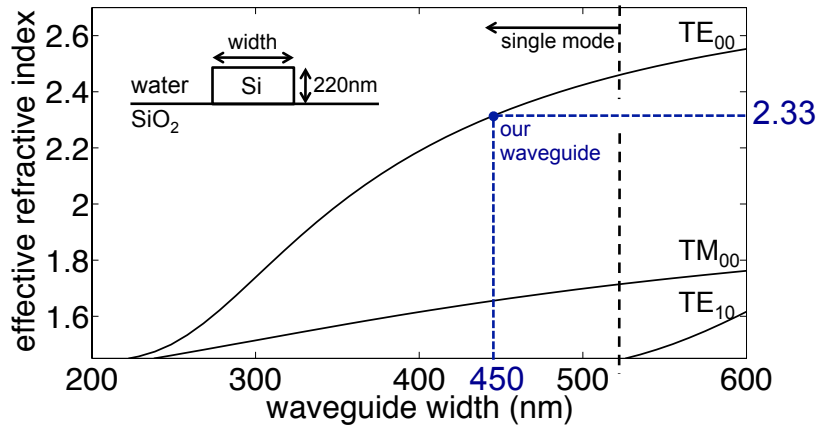


Figure 2.2: A 220 nm-high silicon strip waveguide with silica bottom cladding immersed in water (inset) can guide multiple modes ($n_{eff} > n_{SiO_2}$) at a wavelength of $1.55 \mu\text{m}$, depending on its width. It only guides one quasi-TE polarized mode and one quasi-TM polarized mode when narrower than 520 nm, allowing to make ring resonators with limited undesired multimode interference. With the exception of the dual polarization sensor presented in chapter 3, all wire-based sensors in this thesis use the quasi-TE mode of a 450 nm-wide waveguide.

two remaining quasi-TE and quasi-TM modes is large, coupling between these modes will be limited because of the phase mismatch and very different mode profiles. For widths under 520 nm, the silicon photonic wire waveguide studied here will be single-mode for each polarization (Figure 2.2).

With the exception of the dual polarization sensor presented in chapter 3, all wire-based sensors in this thesis use the quasi-TE mode of a 450 nm-wide waveguide (Figures 2.3 and 2.4) at the wavelength of $1.55 \mu\text{m}$. Its strong confinement allows very compact and performant sensors, and moreover reduces non-specific interactions with refractive index changes in the aqueous cladding, and this reduction has a positive impact on the sensor's limit of detection (section 2.3). The waveguide will also remain single-mode when clad with silicon dioxide or benzocyclobutene (BCB), which is important to make reference sensors for temperature compensation (section 2.4.3) and for the Vernier-cascade sensors presented in chapters 5 and 6.

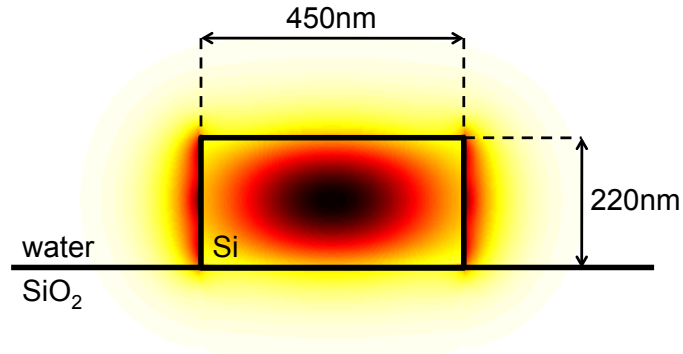


Figure 2.3: The strong confinement of the quasi-TE mode of a 220 nm-high and 450 nm-wide silicon waveguide at a wavelength of $1.55 \mu\text{m}$, as illustrated here by the profile of the electric field energy density, allows to make very compact sensors. Additionally, the mode only interacts with refractive index changes close to its surface, which has a positive impact on the limit of detection of biosensors (section 2.3). However, the discontinuity of the dominant transverse electric field component at the sidewalls increases the loss due to scattering at sidewall roughness.

2.1.2 Loss

Loss limits the performance of ring resonator sensors through its impact on the resonance sharpness (sections 2.2 and 2.4). Many factors contribute to loss in silicon wire waveguides, of which an overview can be found elsewhere [12, 15]. As the intensity in the ring resonator sensors presented in this thesis is low enough to avoid non-linear absorption, the two main loss factors are scattering at sidewall roughness and absorption by the aqueous cladding. Additionally, bend losses can play a very important role in ring resonators with bend radii of only a few micrometers. This section discusses the impact of these three loss factors.

Dry etching creates rough sidewalls [11, 16] (Figure 6.2(b)) that especially scatter the quasi-TE mode, that has a field discontinuity there that causes large intensities at the location of the roughness. The amount of scattering depends on the magnitude and statistics of the roughness and requires full three dimensional modeling for accurate predictions [17]. The propagation loss of the quasi-TE mode in our waveguides is $2.7 \pm 0.06 \text{ dB/cm}$ in air [11], which can serve as an upper limit for the loss in water-clad waveguides. If we do not consider water absorption, the scatter loss in water-clad waveguides will be lower because of the smaller refractive

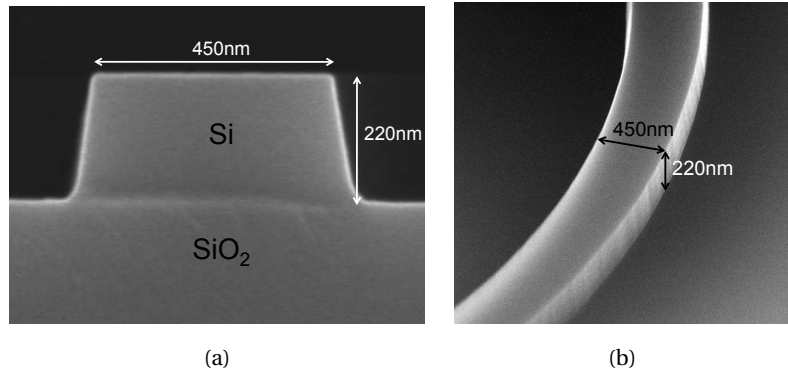


Figure 2.4: (a) The sidewalls of a practical silicon wire waveguide fabricated with 193 nm optical lithography and dry etching [10, 11] are angled, as can be seen on the scanning electron micrograph of its cross section (reproduced from [12]). This increases the bend losses due to cross polarization coupling in sharp bends [12]. More importantly, the sidewalls are rough (scanning electron micrograph in (b), reproduced from [14]), which especially scatters the quasi-TE mode due to the large field discontinuities at the sidewalls that cause large intensities at the location of the roughness. This is presumably the most important factor in the propagation loss of the quasi-TE mode in our waveguides in air (2.7 ± 0.06 dB/cm [11])

index contrast. Next to loss, sidewall roughness can also cause coherent backscattering in a ring resonator, which can distort its transmission spectrum [18], see Figure 2.13(c) in section 2.2.5 for an example.

Concerning the second loss factor, water significantly absorbs light at the wavelength of $1.55 \mu\text{m}$ (Figure 2.5), with an absorption coefficient as high as $10.9 / \text{cm}$ [19]. This contributes 8.8 dB/cm to the propagation loss of the quasi-TE mode of the considered wire waveguide, as a simulation with the mode matching solver *Fimmwave* indicates. The impact of water absorption on the propagation loss is thus four times larger (6 dB) than the other loss factors together. Moving to a smaller operating wavelength with less water absorption, such as the other popular telecommunication wavelength of $1.3 \mu\text{m}$, might be interesting, although increasing scatter losses at shorter wavelengths could annihilate the benefit. This could be a topic for further research.

A third loss factor is bend loss. In a bend, losses increase because of mode mismatch at the straight-bend interface, coupling to the quasi-TM

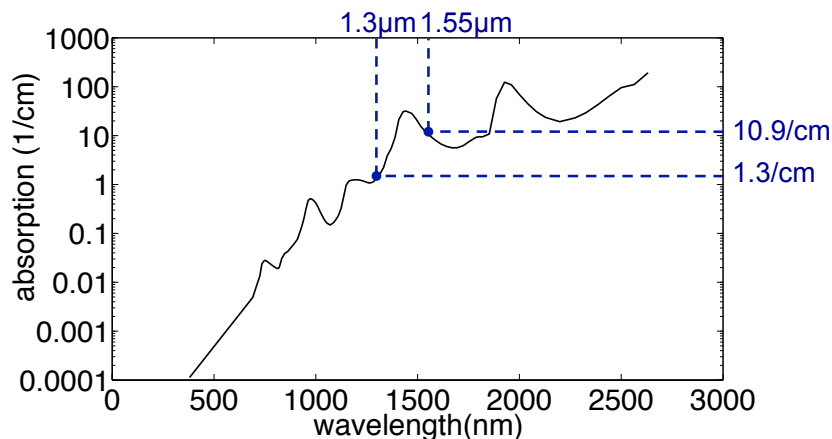


Figure 2.5: Water significantly absorbs light in the near infrared wavelength region [19], which forms a very important loss factor in our sensors. Absorption at the telecom wavelength of $1.3 \mu\text{m}$ ($1.3 / \text{cm}$) is considerably lower than at our wavelength of choice $1.55 \mu\text{m}$ ($10.9 / \text{cm}$), indicating a possible benefit of moving to this wavelength. However, scattering losses in a waveguide increase with decreasing wavelength, which can annihilate this benefit.

guided mode and higher order radiating modes and increased scattering at the outer sidewall of the bend. Although the strong confinement of the quasi-TE mode in a silicon wire waveguide allows bend radii of only a few micrometers with still acceptable loss for most applications, ring resonator sensors can suffer significantly from extra losses in bends. The excess bend loss of the quasi-TE mode of a $500 \text{ nm} \times 220 \text{ nm}$ silicon wire in air that is circularly bent with $5 \mu\text{m}$ radius is 0.009 dB/cm [11]. This corresponds with 11.5 dB/cm average loss in the bend, which is almost 8 times more (8.8 dB) than the straight propagation loss of the same waveguide (2.7 dB/cm). Therefore, the bend radii of the ring resonator sensors presented in this thesis are chosen (much) larger where possible. Section 2.2.5 studies the loss in a ring resonator sensor with $16 \mu\text{m}$ bend radius.

2.1.3 Dispersion

The strong confinement of optical modes in silicon waveguides makes them highly dispersive, meaning that their effective refractive index is heavily wavelength dependent. This has a large impact on the spectral characteristics of ring resonator sensors (section 2.2). The group refractive

index of an optical mode is a useful figure to take first-order dispersion into account, and is defined as

$$n_g = n_{eff} - \lambda \frac{dn_{eff}}{d\lambda} \quad (2.1)$$

with n_{eff} the effective refractive index and λ the wavelength in vacuum.

All optical modes used in this thesis have a normal first-order dispersion, with a group refractive index that is larger than the effective refractive index. The quasi-TE mode of the $450 \text{ nm} \times 220 \text{ nm}$ silicon wire waveguide has a group refractive index (4.36) that is almost twice its effective refractive index (2.34), indicating the importance to take first-order dispersion into account.

This section introduced the principal waveguide mode for our sensors, and summarized its most relevant properties. Next section describes the operation and characteristics of ring resonators, and presents an advantageous design for biosensing.

2.2 Silicon ring resonators

Ring resonators are well-known photonic components [14, 20, 21] that are applicable as filters in wavelength division multiplexed networks [22], as delay elements in optical buffers [23], and when combined with active materials also as laser cavities [24, 25] and modulators [26]. Before section 2.3 presents their use as transducers for label-free biosensing, this section discusses their relevant characteristics.

Ring resonators consist of a closed-loop waveguide in which a propagating mode constructively interferes with itself when its wavelength fits an integer times in the loop. The ring is thus in resonance at wavelengths λ_{res} :

$$\lambda_{res} = \frac{n_{eff}L}{m}, m \in \mathbb{N} \quad (2.2)$$

with L the physical roundtrip length of the ring resonator and n_{eff} the effective refractive index of the waveguide mode. One or more access waveguides are coupled to the ring cavity to provide access to its resonant modes. This section introduces two configurations that will be used for the sensors presented in this thesis, the all-pass configuration with one access waveguide (section 2.2.1) and the channel drop configuration with two access waveguides (section 2.2.2). Section 2.2.4 discusses the

evanescent coupling between the cavity and the access waveguides, and section 2.2.5 presents the experimental characteristics of a silicon ring resonator designed for biosensing.

2.2.1 All-pass ring resonators

In the all-pass configuration (Figure 2.6), one access waveguide couples a fraction k of its field amplitude to the ring. When losses in the coupler are neglected, this amplitude cross-coupling coefficient relates to the amplitude self-coupling coefficient via $r = \sqrt{1 - k^2}$. Note that the phase of the resonator mode runs $\frac{\pi}{2}$ radians behind that of the access waveguide mode. The transmission of one roundtrip is $a \cdot \exp\left(-j\frac{2\pi}{\lambda} n_{eff} L\right)$, where the roundtrip amplitude transmission a relates to the attenuation coefficient of the ring waveguide α via $a = \exp\left(-\frac{\alpha}{2} L\right)$.

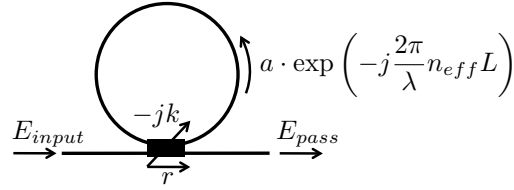


Figure 2.6: An all-pass ring resonator has one access waveguide that couples a fraction k of its field amplitude to the ring, while a fraction r remains in the access waveguide. The roundtrip field transmission is $a \cdot \exp\left(-j\frac{2\pi}{\lambda} n_{eff} L\right)$, and the cavity is in resonance when the roundtrip phase is a multiple of 2π . Since the phase is delayed by $\frac{\pi}{2}$ radians when coupling between the ring and the access waveguide and visa versa, destructive interference occurs at resonance between the access waveguide mode and light coupled back from the ring to the access waveguide, giving rise to dips in the transmission spectrum (in the realistic case of $a < 1$).

The power transmission of the all-pass ring resonator in continuous wave regime can be formulated as [21]:

$$T_{allpass}(\lambda) = \frac{a^2 - 2ar \cos\left(\frac{2\pi}{\lambda} n_{eff}(\lambda) L\right) + r^2}{1 - 2ar \cos\left(\frac{2\pi}{\lambda} n_{eff}(\lambda) L\right) + (ar)^2} \quad (2.3)$$

Note the wavelength dependent effective refractive index. Taking only first order dispersion into account, the roundtrip phase is proportional to

the group refractive index, except for a constant (appendix A):

$$\frac{2\pi}{\lambda} n_{eff}(\lambda) L \approx \frac{2\pi}{\lambda} n_g L + constant$$

The shape of the transmission spectrum is thus determined by the group refractive index, while the exact position of the resonances is determined by the constant.

In the theoretical case of a lossless ring ($a = 1$) the power transmission is unity for all wavelengths, hence the name *all-pass* ring resonator. In this case the component only acts as a phase rotator. However, in practical ring resonators ($a < 1$) the power transmission exhibits dips at the resonance wavelengths (Figure 2.7), caused by destructive interference between the access waveguide mode and the light coupled back from the ring to the access waveguide.

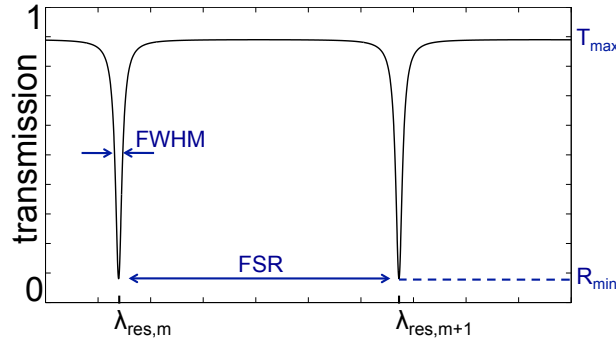


Figure 2.7: The power transmission spectrum of an all-pass ring resonator exhibits dips at the resonance wavelengths that are characterized by their full-width at half-maximum (*FWHM*) and on-off extinction (T_{max}/R_{min}). The spectral distance between consecutive resonances is the free spectral range (*FSR*).

Each resonance dip is characterized by its on-off extinction ratio T_{max}/R_{min} and its full-width at half maximum (*FWHM*):

$$T_{max} = \frac{(a+r)^2}{(1+ar)^2} \quad (2.4)$$

$$R_{min} = \frac{(r-a)^2}{(1-ar)^2} \quad (2.5)$$

$$FWHM = \frac{(1-ar)\lambda_{res}^2}{\pi n_g L \sqrt{ar}} \quad (2.6)$$

The resonances broaden with increasing roundtrip loss (decrease of a) and increasing coupling (decrease of r). The extinction ratio of an under-coupled ring resonator ($r > a$) increases with increasing coupling until it becomes infinite at critical coupling ($r = a$). The latter is an interesting regime for sensing, since it allows accurate measurements of the resonance wavelength (section 2.4). Over-coupling ($r < a$) decreases the extinction ratio again and further broadens the resonances.

The spectral distance between subsequent resonances is called the free spectral range (FSR), which in first order approximation of the dispersion becomes

$$FSR = \frac{\lambda^2}{n_g \cdot L} \quad (2.7)$$

Alternative parameters of a resonator that relate to previously defined parameters are the quality factor $Q = \frac{\lambda_{res}}{FWHM}$ and the Finesse $\mathcal{F} = \frac{FSR}{FWHM}$.

All-pass ring resonators are very suited for sensing (section 2.3), since they can achieve sharper resonances than the channel drop sensors described in next section. Therefore they are the resonators of choice for the sensors described in section 2.2.5 of this chapter, in chapter 4 and in chapter 3, section 3.4.2.

2.2.2 Channel drop ring resonators

For some sensors, such as the dual polarization sensor introduced in chapter 3, section 3.4.1 and the Vernier-cascade sensors described in chapters 5 and 6, a second access waveguide to the resonator is required (Figure 2.8).

Part of the light will be coupled to the drop port of the second access waveguide, while the pass port of the first access waveguide is similar to the output port of the all-pass resonator described in previous section. The power transmission in continuous wave regime to that pass port can be described as [21]:

$$T_{pass}(\lambda) = \frac{r_1^2 + a^2 r_2^2 - 2ar_1 r_2 \cos\left(\frac{2\pi}{\lambda} n_{eff}(\lambda) L\right)}{1 + (ar_1 r_2)^2 - 2ar_1 r_2 \cos\left(\frac{2\pi}{\lambda} n_{eff}(\lambda) L\right)} \quad (2.8)$$

which is similar to the transmission of an all-pass resonator (equation (2.3)) with a roundtrip amplitude transmission ar_2 . The coupling to the

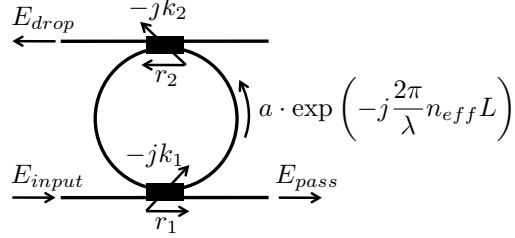


Figure 2.8: A channel drop ring resonator has a second access waveguide that receives part of the light of the cavity, providing a power transmission spectrum with resonance peaks at its drop port. The pass port behaves as the output of an all-pass ring resonator, for which the coupling to the second access waveguide behaves as an extra loss factor that broadens the resonances compared to an all-pass ring resonator.

second access waveguide thus behaves as an extra loss factor, which also reflects in the characteristics of the resonance dips (Figure 2.9):

$$T_{max} = \frac{(r_1 + ar_2)^2}{(1 + ar_1r_2)^2} \quad (2.9)$$

$$R_{min} = \frac{(r_1 - ar_2)^2}{(1 - ar_1r_2)^2} \quad (2.10)$$

$$FWHM = \frac{(1 - ar_1r_2) \lambda_{res}^2}{\pi n_g L \sqrt{ar_1r_2}} \quad (2.11)$$

The free spectral range can still be expressed by equation (2.7). The on-off extinction ratio T_{max}/R_{min} becomes infinite at the critical coupling condition $r_1 = ar_2$. The full-width at half-maximum ($FWHM$) at critical coupling of a ring resonator in the channel drop configuration is larger than that of a similar resonator in the all-pass configuration, which has a negative impact on its performance for sensing (section 2.4).

However, the second access waveguide provides a power transmission spectrum at its drop port that can be formulated as [21]:

$$T_{drop}(\lambda) = \frac{a(1 - r_1^2)(1 - r_2^2)}{1 + (ar_1r_2)^2 - 2ar_1r_2 \cos\left(\frac{2\pi}{\lambda} n_{eff}(\lambda) L\right)} \quad (2.12)$$

which exhibits peaks at the resonance wavelengths (Figure 2.9) that will prove to be useful for the Vernier-cascade sensors described in chapters 5 and 6. The resonance peaks are characterized by their full-width at

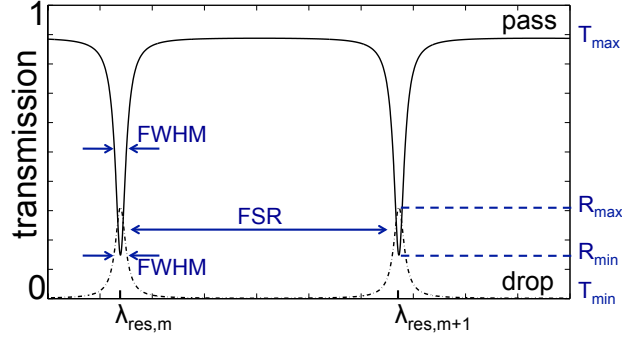


Figure 2.9: The power transmission to the drop port has peaks at the resonance wavelengths with an on-off extinction ratio R_{max}/T_{min} , while the power transmission to the pass port has resonance dips similar to the transmission of an all-pass ring resonator.

half-maximum (equation 2.11), the minimal transmission at the drop port T_{min} and the peak transmission at resonance R_{max} :

$$T_{min} = \frac{a(1-r_1^2)(1-r_2^2)}{(1+ar_1r_2)^2} \quad (2.13)$$

$$R_{max} = \frac{a(1-r_1^2)(1-r_2^2)}{(1-ar_1r_2)^2} \quad (2.14)$$

The on-off extinction ratio at the drop port is defined as R_{max}/T_{min} .

2.2.3 Lorentzian approximation of resonances

Data-fitting is an important tool to extract resonator parameters from measured transmission spectra. However, formulas (2.3), (2.8) and (2.12) are not suited for fitting because of the periodic cosine terms. Therefore, the following easy-to-fit Lorentzian function will be used to fit to resonance dips in the pass transmission:

$$T_{dip}(\lambda) \approx \frac{R_{min} \left(\frac{FWHM}{2} \right)^2 + (\lambda - \lambda_{res})^2}{\left(\frac{FWHM}{2} \right)^2 + (\lambda - \lambda_{res})^2} \quad (2.15)$$

It immediately gives access the resonance wavelength, full-width at half-maximum and extinction. In appendix B it is proven that this function

approximates equations (2.3) and (2.8) very well close to resonance wavelengths.

Similarly, appendix B proves that following Lorentzian function approximates equation (2.12) very well, and can therefore be used for fitting to resonance peaks in the drop spectrum:

$$T_{peak}(\lambda) \approx \frac{R_{max} \left(\frac{FWHM}{2} \right)^2}{\left(\frac{FWHM}{2} \right)^2 + (\lambda - \lambda_{res})^2} \quad (2.16)$$

2.2.4 Coupling section

A directional coupler is commonly used to couple light between a ring resonator and its access waveguides [27, 28], and it is also the coupler of choice in this thesis. It consists of two waveguides that are brought close together so that the waveguide modes are coupled and power can be transferred from one mode to the other. Alternatively, a multimode interferometer coupler is sometimes preferred [29].

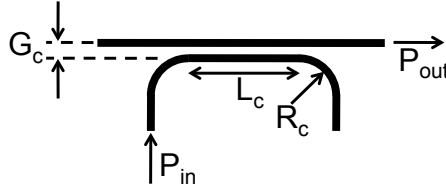


Figure 2.10: The directional coupler employed for most sensors in this thesis consists of a section with length L_c where the two waveguides are parallel to each other with a gap G_c , and two identical sections where one of the two waveguides is bent away from the other with radius R_c . The parallel section is characterized by its coupling coefficient per unit distance κ [$1/\mu m$], while the two bent regions together cause an offset coupling κ_0 .

The directional coupler employed for most sensors in this thesis (Figure 2.10) consists of a section with length L_c where the two waveguides are parallel to each other with a gap G_c , and two identical sections where one of the two waveguides is bent away from the other with radius R_c . The power cross coupling can be formulated as [5]:

$$k^2 = \frac{P_{out}}{P_{in}} = \sin^2(\kappa \cdot L_c + \kappa_0) \quad (2.17)$$

with κ [$1/\mu\text{m}$] the coupling coefficient per unit distance in the parallel section of the coupler and κ_0 the offset coupling in the two bent regions. The coupling strength (both κ and κ_0) increases with increasing wavelength, due to a decreasing mode confinement.

Practical directional couplers, especially in a material system with such a large refractive index contrast as silicon-on-insulator, have a maximum power transfer that is smaller than 100 % [15]. However, also for the directional couplers with limited power transfer applied here, formula (2.17) is a good approximation.

2.2.5 Silicon ring resonator for biosensing

An advantageous ring resonator biosensor design consists of a rounded square shaped cavity and a single directional coupler that is shorter than the sides of the cavity (Figure 2.11(a)), so that the properties of the directional coupler and the cavity are independent to a large extent. The all-pass configuration can attain sharper resonances than the channel drop configuration (formulas (2.6) and (2.11)), and the small aspect ratio of the sensor is beneficial for the uniformity of local biochemical surface modifications by spotting (section 2.6). While the mode mismatch at the eight straight-bend transitions induces extra roundtrip loss, this is expected to be low for the sensors with large bend radii studied here.

Our implementation in silicon-on-insulator (Figure 2.11(b)) consists entirely of the aforementioned 450 nm-wide wire waveguide. Its cavity roundtrip provides a free spectral range (3.6 nm) that is larger than the maximal expected resonance wavelength shift in biosensing, avoiding aliasing in the sensor output without additional requirements on the temporal resolution of the interrogation. The cavity's bend radius (16 μm) and straight sections (10 μm) offer low bend loss, while still having sides that are longer than the directional coupler. The gap (250 nm) can be easily obtained with 193 nm optical lithography and dry etching, and is a trade-off between having strong coupling for a short couple section and a reduction of the scatter loss due to mode mismatch and sidewall roughness in the coupler. The coupler length was swept to enable a study of some important resonator parameters.

A ring resonator sensor preferably has clearly visible resonances with a large extinction ratio that can be resolved in a noise resistant way (section 2.4). Therefore, the amplitude self-coupling r should match the amplitude roundtrip transmission a , which corresponds with critical coupling.

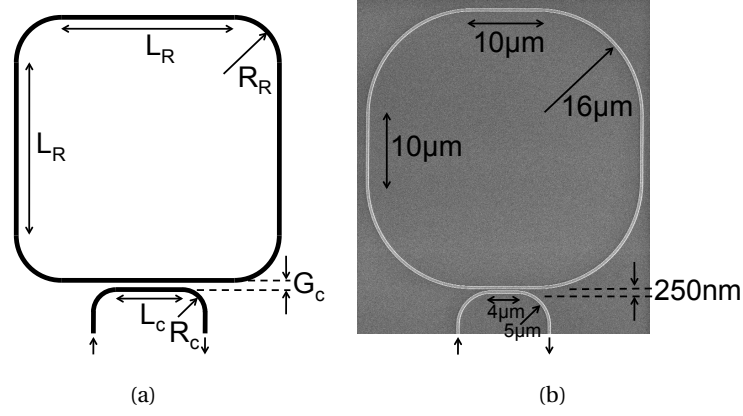


Figure 2.11: (a) The proposed ring resonator has a rounded square shaped cavity with sides that are longer than the directional coupler to allow close-to independent design of the cavity parameters (R_r and L_r) and coupler parameters (L_c , G_c and R_c). (b) Our silicon implementation has a roundtrip length to obtain a free spectral range that is large enough (3.6 nm in water) to have an unambiguous sensor signal, while retaining sharp resonances. The rather large gap (250 nm) of the directional coupler relaxes the fabrication requirements and reduces scattering. Different resonators on the same chip with a variation of the coupler length L_c allowed a study of the resonator parameters (Figure 2.12).

The properties of a measured transmission spectrum of an all-pass ring resonator yield a and r via [30]:

$$(a, r) = \sqrt{\frac{A}{B}} \pm \sqrt{\frac{A}{B} - A} \quad (2.18)$$

with

$$A = \frac{\cos\left(\frac{\pi \cdot FWHM}{FSR}\right)}{1 + \sin\left(\frac{\pi \cdot FWHM}{FSR}\right)}$$

$$B = 1 - \frac{R_{min}}{T_{max}} \left(\frac{1 - \cos\left(\frac{\pi \cdot FWHM}{FSR}\right)}{1 + \cos\left(\frac{\pi \cdot FWHM}{FSR}\right)} \right)$$

where $FWHM$ is the full-width at half-maximum of the measured resonance, FSR the free spectral range, R_{min} the transmission at resonance and T_{max} the maximum off-resonance transmission. Parameters a and r cannot be distinguished for individual resonances, but can be disentangled from the measurement of multiple resonances based on their

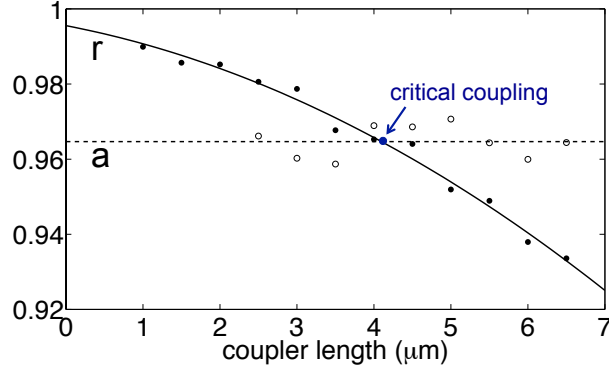


Figure 2.12: Formula (2.20) fits rather well to experimental values of the amplitude self-coupling r for the quasi-TE resonances in water at wavelengths around $1.55 \mu\text{m}$ of the ring resonator depicted in Figure 2.11(b) as a function of its coupler length. The resulting value of the coupling coefficient in the parallel section of the directional coupler is $\kappa = 0.042 / \mu\text{m} \pm 0.002 / \mu\text{m}$, and the offset coupling in the two bent regions is $\kappa_0 = 0.095 \pm 0.009$. Critical coupling occurs for a coupler length of $4.1 \mu\text{m}$, when the amplitude self-coupling r matches the amplitude roundtrip transmission $a = 0.965 \pm 0.004$.

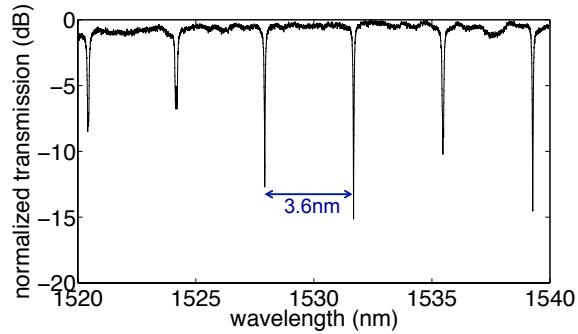
different wavelength dependence [30]. Here, the transmission was measured of different ring resonators on the same chip with only a variation of the coupler length. Since the amplitude self-coupling r depends much more on the coupler length than the amplitude roundtrip transmission a , this different dependence was used to separate the two parameters (Figure 2.12). When all losses in the coupler are incorporated in a , the amplitude self- and cross-coupling relate as $k^2 + r^2 = 1$. Formula (2.17) then yields:

$$r = |\cos(\kappa \cdot L_c + \kappa_0)| \quad (2.19)$$

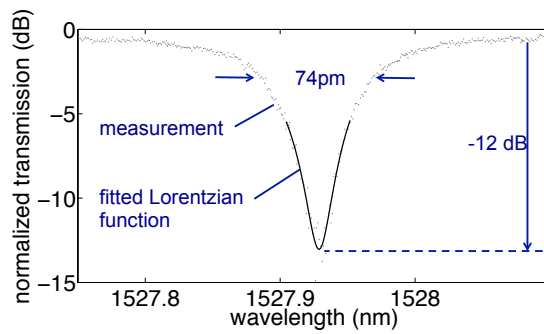
with κ [$1/\mu\text{m}$] the coupling coefficient per unit distance in the parallel section of the coupler and κ_0 the offset coupling in the two bent regions. Since periodic functions can cause inaccurate data-fitting, formula (2.19) is approximated by its second order Taylor polynomial around zero coupler length:

$$r \approx -\frac{1}{2}\kappa^2 \cos \kappa_0 \cdot L_c^2 - \kappa \sin \kappa_0 \cdot L_c + \cos \kappa_0 \quad (2.20)$$

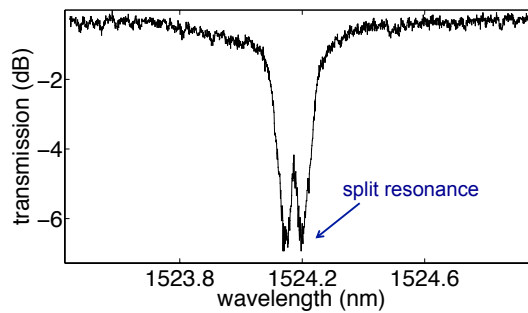
which fits well to the experimental data (Figure 2.12) with $\kappa = 0.042 / \mu\text{m} \pm 0.002 / \mu\text{m}$ and $\kappa_0 = 0.095 \pm 0.009$.



(a)



(b)



(c)

Figure 2.13: The proposed ring resonator (Figure 2.11(b)) is close-to critically coupled with a $4\ \mu\text{m}$ -long directional coupler, resulting in clearly visible resonance dips with (a) 3.6 nm free spectral range and (b) an extinction ratio of $-12\ \text{dB}$ for the quasi-TE mode in water. The full-width at half-maximum is only 74 pm, which corresponds with a quality factor of 21000. (c) Backscattering at sidewall roughness in the ring waveguide can cause distortions of the resonance dips, such as splitting of the resonance dips [18].

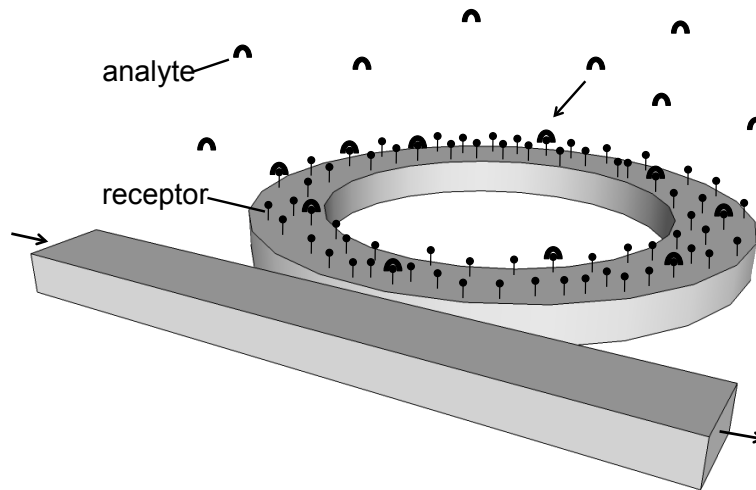
The average amplitude roundtrip transmission is -0.156 dB, which corresponds with 11 dB/cm average propagation loss in the cavity. Absorption by water (8.8 dB/cm) and scattering at the waveguide's sidewall roughness (2.7 dB/cm) dominate the loss (section 2.1.2), and extra loss due to the bends, straight-bend interfaces and directional couplers is negligible.

The ring resonator is close-to critically coupled with a $4\ \mu\text{m}$ -long directional coupler (Figure 2.12), resulting in a clearly visible resonance dip with an extinction ratio of -12 dB for the quasi-TE mode in water (Figure 2.13). The full-width at half-maximum is only 74 pm, which corresponds with a quality factor of 21000. This compares favorably with the ring resonator sensor previously proposed by our research group [5, 6, 31], which has broader resonances ($FWHM \approx 300$ pm in water) because of its sharper bends and channel drop configuration. M. Iqbal et al. [1] presented a circular ring resonator sensor with resonances as narrow as 36 pm, but it is unclear whether this was measured with an absorbing water cladding.

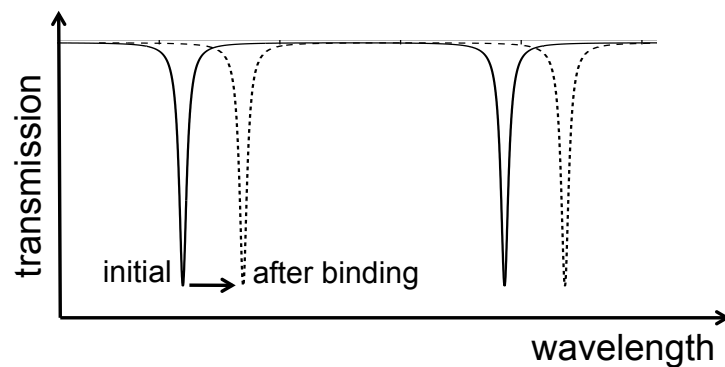
Some improvements to the proposed ring resonator sensor can be considered. When interrogated with a fast wavelength-tunable laser, the sensor benefits from a much larger roundtrip through the reduced free spectral range and consequent improved temporal resolution of the interrogation (section 2.4.4). Reducing the absorption loss by operating at smaller wavelengths (section 2.1.2) might be annihilated by increased scatter loss at sidewall roughness. Employing the quasi-TM mode at smaller wavelengths can avoid this drawback because of the absence of the large field discontinuity at the waveguide sidewalls, and can therefore also reduce the backscattering in the ring resonator and consequent distortions of the transmission spectrum (Figure 2.13(c)). Note however that this approach requires large bend radii because of the smaller mode confinement.

2.3 Evanescent field sensing with ring resonators

A ring resonator label-free biosensor directly measures selective affinity interactions between analyte molecules and receptor molecules immobilized on the ring waveguide surface (Figure 2.14(a)). Since most biological molecules (proteins, DNA, ...) have a refractive index (around 1.45) larger than that of the aqueous solvent (around 1.31), this molecular binding locally increases the refractive index in the range of the evanescent field of the waveguide mode. The resulting phase change of the mode in-



(a)



(b)

Figure 2.14: A ring resonator label-free biosensor consists of a waveguide with a chemically modified surface that presents receptor molecules that are selective to the analyte. Analyte molecules, if present in a fluidic sample, diffuse to the sensor and bind to the receptors, increasing the refractive index in the evanescent field of the ring resonator waveguide. The consequent shift of the resonance wavelength signifies the concentration of the analyte, and the kinetics and affinity of the biochemical reaction.

duces measurable shifts of the resonance wavelengths of the ring (Figure 2.14(b)), which are continuously monitored over time and which give information on the analyte concentration, affinity between the molecules and the kinetics of the biochemical reaction.

This section discusses the properties of the evanescent field of the quasi-TE mode of our silicon wire waveguide (section 2.3.1), and provides formulas that describe the impact of a refractive index change in the evanescent field on the mode's phase change and eventually on the ring's resonance wavelength shift (section 2.3.2). It also introduces the interrogation method of the latter, and describes the binding curves that result from continuously monitoring affinity reactions (section 2.3.3).

2.3.1 Evanescent field

The evanescent field of a guided mode is the fraction that extends in the cladding. It decays exponentially with the distance from the core cladding interface:

$$|\vec{E}(d)| = |\vec{E}(0)| \cdot \exp(-\gamma d)$$

with $|\vec{E}(d)|$ the electric field in the cladding as a function of the distance d from the interface. The decay constant γ can be formulated as [32]:

$$\gamma = \frac{2\pi}{\lambda} \sqrt{n_{eff}^2 - n_w^2}$$

with n_{eff} the effective refractive index of the waveguide mode and n_w the refractive index of the (watery) cladding. A large refractive index contrast thus results in a fast decay.

The quasi-TE mode of our 450 nm-wide and 220 nm-high waveguide (section 2.1.1, Figure 2.2) has a decay constant as high as $7.8/\mu\text{m}$ in water, so that its electric field energy density has decreased to 36.7% ($1/e$) of its value at the core-cladding interface at a distance of only 64 nm (Figure 2.15). This corresponds qualitatively with the experimental value (52.3nm) measured by M. S. Luchansky et al. [33] for a similar 500 nm-wide waveguide. The mode thus only interacts with changes in the cladding that happen tens of nanometers from the waveguide's surface, making it very selective towards refractive index changes caused by molecular binding near that surface. This is a large asset for our biosensors, since it decreases the interaction with refractive index changes in the liquid away from the surface, and therefore improves the signal-to-noise ratio. Although the evanescent field is non-uniformly distributed over the waveguide surface

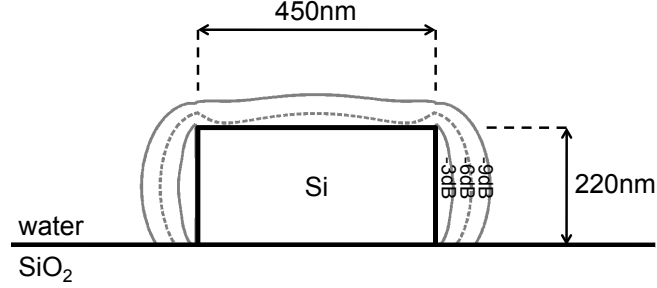


Figure 2.15: The energy density of the evanescent electric field of the quasi-TE mode of our silicon wire waveguide decays exponentially with the distance from the waveguide surface with a penetration depth of only a few tens of nanometers. Consequently, the mode is very selective to refractive index changes that happen close to the waveguide surface, which is a large asset for noise-resistant label-free biosensing. The electric field energy density of the evanescent field varies significantly over the waveguide surface, with its maximum value (the normalization reference) occurring approximately in the middle of the sidewalls and an almost four times lower (6 dB) value at two spots at the waveguide top side. The resulting non-uniform sensitivity to molecular binding depending on the binding location is averaged out in practice, and only becomes relevant when approaching single-molecule detection.

(Figure 2.15), the impact for sensing is negligible when working far enough from single-molecule detection limits.

2.3.2 Sensitivity to refractive index changes

The effective refractive index of the waveguide mode changes with a changing refractive index of the cladding in the range of its evanescent field. Using the method described in [34], it can be found that:

$$\Delta n_{eff} \propto \underbrace{n_g}_{\sim \text{temporal confinement}} \cdot \underbrace{\frac{\iint_{-\infty}^{\infty} n(x,y) \cdot \Delta n(x,y) \cdot |\vec{E}(x,y)|^2 dx dy}{\iint_{-\infty}^{\infty} n^2(x,y) \cdot |\vec{E}(x,y)|^2 dx dy}}_{\sim \text{spatial confinement}} \quad (2.21)$$

with Δn_{eff} the change of the effective refractive index and n_g the group index of the mode, $n(x,y)$ the refractive index profile of the waveguide,

$\Delta n(x, y)$ its change, and $\vec{E}(x, y)$ the electric field phasor. Formula (2.21) expresses that the change of the effective refractive index as a consequence of a refractive index change is proportional to the product of a factor related to the temporal confinement (n_g) and a factor related to the spatial confinement of the electric field energy density. Note that the latter is different from the power confinement in high-index-contrast material systems such as silicon-on-insulator, since there the electric and magnetic field distributions are not proportional. This results from the large electric field discontinuities at the waveguide interfaces.

The resonance wavelength of a ring resonator mode will shift when its effective refractive index changes (Appendix C):

$$\Delta\lambda = \frac{\lambda \cdot \Delta n_{eff}}{n_g} \quad (2.22)$$

with the group index in the denominator to take the large first order dispersion of our waveguides into account. Substituting equation (2.21) in equation (2.22) yields:

$$\Delta\lambda \propto \frac{\iint_{-\infty}^{\infty} n(x, y) \cdot \Delta n(x, y) \cdot |\vec{E}(x, y)|^2 dx dy}{\iint_{-\infty}^{\infty} n^2(x, y) \cdot |\vec{E}(x, y)|^2 dx dy} \quad (2.23)$$

When a molecule with volume V_{mol} and refractive index n_{mol} binds at location (x, y) to the waveguide surface in the watery top cladding environment with refractive index n_w , equation (2.23) can be simplified to

$$\Delta\lambda(x, y) \propto \frac{n_{mol} \cdot (n_{mol} - n_w) \cdot V_{mol} \cdot |\vec{E}(x, y)|^2}{\iint_{-\infty}^{\infty} n^2(x, y) \cdot |\vec{E}(x, y)|^2 dx dy} \quad (2.24)$$

$$\propto \frac{|\vec{E}(x, y)|^2}{\iint_{-\infty}^{\infty} n^2(x, y) \cdot |\vec{E}(x, y)|^2 dx dy} \quad (2.25)$$

assuming the molecule is small enough to neglect variations of the electric field over its volume.

While a large temporal confinement (large n_g) directly increases the light-matter interaction (equation (2.21)), it has no direct impact on the sensor

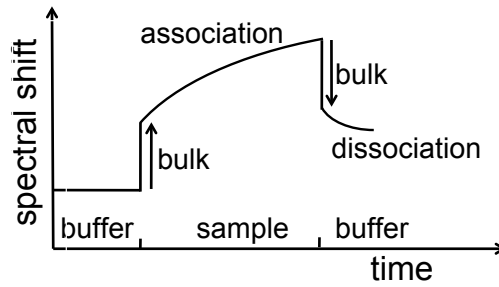
sensitivity (equation (2.25)). Slowing down light thus has no straightforward benefit, and can only have an impact through a change of the spatial mode profile.

The sensitivity does benefit from the large field enhancement at the waveguide surface (equation (2.25)) resulting from the large refractive index contrast. The normal component of the electric displacement field must be continuous at a dielectric interface, so that the value of the normal component of the electric field at the cladding-side of the core-cladding interface is enhanced with a factor $n_{core}^2/n_{cladding}^2$ compared to its value at the core-side. For the high-index-contrast interface between silicon ($n_{core} = 3.47$) and water ($n_{cladding} = 1.31$) in our sensors, this corresponds with a sevenfold enhancement of the electric field component normal to the waveguide surface. The quasi-TE mode of a wire waveguide has its major electric field component normal to the waveguide sidewalls, so that the major field discontinuity occurs there (Figures 2.3 and 2.15). Although the horizontal confinement of the selected 450 nm-wide and 220 nm-high waveguide (section 2.1.1, Figure 2.2) is lower than its vertical confinement, its quasi-TE mode is on average twice as sensitive to refractive index changes at its sidewalls than at its top surface (Figure 2.15).

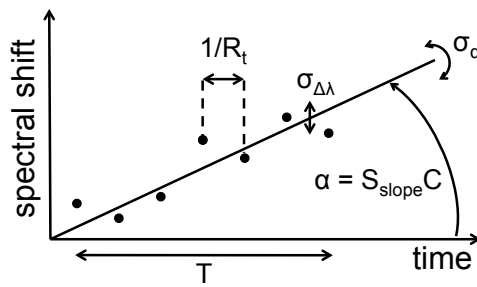
2.3.3 Binding curves

A binding curve or sensorgram (Figure 2.16(a)) results from monitoring the resonance wavelength shifts of a ring resonator sensor over time while analyte molecules interact with the receptor molecules. It provides information on the analyte concentration, and on the affinity and kinetics of the interaction.

Accurately monitoring spectral shifts of a ring resonator sensor requires repetitive measurement of its transmission spectrum with high spectral and temporal resolution. A first approach is to couple broadband light from a light-emitting diode (LED) to the sensor and analyze its spectrum with an optical spectrum analyzer. In chapter 4, this approach is applied to interrogate a slot waveguide ring resonator with an Agilent 86140B spectrum analyzer. However, its spectral resolution (60 pm) is insufficient for the other sensors in this thesis, for which a second approach is applied. This involves changing the wavelength of a laser source and measuring the transmission for different wavelengths with a standard power meter (section 2.8.2) or camera (section 2.8.3). We use a Santec TSL-510C



(a)



(b)

Figure 2.16: A binding curve or sensorgram (a) originates from monitoring the resonance wavelength shift over time while analyte molecules interact with immobilized receptor molecules. Relative to the baseline in buffer, the resonance wavelength shifts upon injection of the sample solution, abruptly due to a bulk refractive index change and gradually with the association of the analyte to the receptor. Switching back to the buffer starts the dissociation phase. The kinetics and affinity of the biochemical reaction can be studied similar to surface plasmons sensors [35]. The initial slope α of the binding curve in the association phase (b) represents the analyte concentration, and can accurately be determined by least-squares fitting a straight line. The limit of detection, the lowest analyte concentration that can reliably be detected, benefits from a low-noise binding curve (small $\sigma_{\Delta\lambda}$), a large temporal resolution R_t , a large measurement time T and a large slope sensitivity S_{slope} .

external cavity laser, which has sufficient spectral resolution (1 pm) to accurately resolve the transmission spectra of the sensors in this thesis. A Lorentzian function (section 2.2.3) is fitted to each measured resonance dip or peak in order to determine the resonance wavelength in a noise tolerant way.

In a direct label-free assay, receptor molecules specific to the analyte are immobilized on the sensor surface prior to the experiment (section 2.6). The experiment is initialized by flowing a buffer solution over the sensor to condition the surface and provide a baseline. When the flow is switched to a solution containing the analyte, the resonance wavelength changes abruptly due to a difference in the bulk refractive index of the analyte solution, and gradually with the capturing of analytes by the receptors (association phase, Figure 2.16(a)). Switching back to the buffer solution starts the dissociation of the analyte from the receptor. Both mass transport and analyte-receptor binding kinetics determine the shape of the binding curve. Diffusion limits the mass transport in most simple flow systems (section 2.7), as a stagnant liquid layer of several micrometers is formed on top of the sensor through which the molecules have to diffuse to reach the sensor surface. The average flow rate determines the thickness of the stagnant layer, and thus influences the diffusion flux. Accurate study of the kinetics and affinity of the analyte-receptor binding requires a binding curve that is not limited by mass transport, a challenging condition that typically requires low receptor surface densities [35]. However, diffusion limitation allows to accurately measure the analyte concentration. Next section introduces a method and discusses the limit of detection.

2.4 Limit of detection

The initial slope of the binding curve (Figure 2.16 (a) and (b)) heavily depends on the analyte quantity or concentration, and allows to rapidly and accurately measure this important figure. When mass transport is only determined by diffusion, the association is linear shortly after switching, with a slope that is proportional to the analyte concentration [35]. This is however not always the case in practical sensor systems: M. Iqbal et al. [1] measured the initial slope of the binding curve of their silicon ring resonator sensor system for interactions between immobilized biotin and streptavidin, which resulted in a sub-linear dependence on the streptavidin-concentration.

Generally a calibration curve $\alpha(C)$ can be constructed for the experiment that gives the relation between the initial slope of the binding curve and the analyte concentration. The accuracy of a concentration measurement depends both on the accuracy of this calibration curve and on the accuracy of the initial slope measurement. Least-squares fitting a straight line to the initial linear part of the binding curve in the association phase (Figure 2.16(b)) allows to determine the initial slope in a noise resistant way.

2.4.1 Approximate formula

The limit of detection (LOD) of the sensor system is a very important property and is the smallest amount or concentration of analyte that can reliably be detected. It is defined by the International Organization of Standardization (ISO) and the International Union of Pure and Applied Chemistry (IUPAC), and discussed in detail by L. A. Currie [36]. It is a two-parameter performance metric that involves a critical value CV that serves as a decision level for the measured concentration $C_{measured}$ for which the chance of a false positive detection is smaller than a predefined value a :

$$Prob[C_{measured} > CV | C_{sample} = 0] \leq a$$

with C_{sample} the real analyte concentration in the sample.

Given this decision level CV , the limit of detection is then the analyte concentration for which the chance of a false negative detection is equal to a predefined value b :

$$Prob[C_{measured} \leq CV | C_{sample} = LOD] = b$$

A typical value for a and b is 5% [36].

An approximative expression for the limit of detection can be obtained by neglecting calibration errors, and assuming a Gaussian distribution of the fitted initial slope with a standard deviation that is independent of the concentration at low concentration-values. In that case both the critical value CV and the limit of detection LOD are proportional to the standard deviation σ_C on the concentration measurement, which is approximately (appendix D):

$$\sigma_C \approx \frac{2\sqrt{3} \cdot \sigma_{\Delta\lambda}}{\sqrt{R_t} \cdot T^{\frac{3}{2}} \cdot S_{slope}} \quad (2.26)$$

with $\sigma_{\Delta\lambda}$ the standard deviation of the Gaussian noise on the binding curve, R_t the temporal resolution of the binding curve (number of measurement points per second), and T the measurement time. The slope sensitivity S_{slope} is the slope of the calibration curve at zero concentration ($S_{slope} = \frac{\partial\alpha(C=0)}{\partial C}$). For the default parameters ($a, b = 0.05$), the critical value and limit of detection become [36]:

$$CV = 1.645 \sigma_C \quad (2.27)$$

$$LOD = 3.29 \sigma_C \quad (2.28)$$

2.4.2 Influencing parameters

Fast sensor interrogation has a positive impact on the limit of detection via the temporal resolution R_t of the binding curve. Rapid capturing of transmission spectra can however be challenging for highly multiplexed sensor systems, and the main approaches are discussed in section 2.8. Capturing transmission spectra by scanning the wavelength of a laser source and measuring the power transmitted by the sensor with a detector results in a temporal resolution that depends on the wavelength scan speed and on the scan range. When multiple sensors are interrogated by splitting the laser beam and employing a detector array, the scan range corresponds to the sensor's free spectral range (FSR), since the resonance wavelengths of the different sensors can be randomly distributed. When using a detector array with 10kHz line rate, a spectral resolution of 1 pm corresponds to 10 nm/s wavelength scan rate, a value easily attainable with typical external cavity lasers. A good estimate for the achievable temporal resolution is thus $10 \text{ nm/s} / \text{FSR}$.

The limit of detection also scales favorably with the measurement time T , provided that the resonance wavelength noise ($\sigma_{\Delta\lambda}$) does not significantly increase when performing long measurements. However, the time-to-result is a very important sensor characteristic, and will therefore often determine the interaction time in practice. A measurement time in the order of 10 min seems a good target [1].

The slope sensitivity S_{slope} directly influences the limit of detection as expected. It scales with the receptor density, the analyte mass and the analyte flux to the sensor. The latter depends on the solvent temperature and viscosity, the molecule size (larger molecules diffuse slower) and on the flow rate (through the thickness of the stagnant layer). The slope sensitivity is moreover proportional to the sensitivity of the ring resonator

sensor to refractive index changes (equation (2.25)). M. Iqbal et al. [1] measured the initial slope of their silicon ring resonator sensor system for the interaction of streptavidin with immobilized biotin, and from their data follows $S_{slope} = 0.18 \text{ pm/min/pM}$. Many routes exist to improve this. Chapter 4 presents a slot waveguide ring resonator that enhances the light-matter interaction, while chapter 5 presents a Vernier-cascade with two ring resonators. More complex assays can also amplify the sensitivity by increasing the bound mass with secondary antibodies [37] or sub-micron beads [38], but this might reduce the practicality of the sensor system.

Finally, noise on the binding curve ($\sigma_{\Delta\lambda}$) also influences the limit of detection, and mainly originates from noise in the optical system, noise in the refractive index of the sample liquid and temperature noise.

First, noise on the resonance wavelength extraction from the optical transmission spectra by fitting a Lorentzian function can dominate the binding curve noise. J. Hu et al. [39] simulated that the accuracy of fitting a Lorentzian function is proportional to the square root of the spectral resolution, or wavelength step, of the transmission spectrum, and to the square root of the resonance width, provided that intensity noise dominates wavelength noise. Moreover, they calculated that the amplitude of both wavelength and intensity noise linearly deteriorate the fitting accuracy. The influence of the resonance extinction is negligible over 15 dB [5, 39], so that the ring is preferably slightly under-coupled (close to critical coupling), since the full-width at half-maximum benefits from a weaker coupling. K. De Vos [5] estimated that the standard deviation on the resonance wavelengths determined by fitting for a sensor such as the one described here (section 2.2.5) is in the order of 100 fm when measured with 1 pm spectral resolution on our interrogation setup.

Second, refractive index noise in the range of the optical mode can also heavily increase the binding curve noise. The sensitivity of our ring resonator sensors to bulk refractive index changes of the liquid is 70 nm/RIU [31], so that despite the high confinement of our waveguides, bulk refractive index changes as small as 10^{-6} RIU already cause resonance wavelength changes of 100 fm and start dominating the noise caused by the optical system and fitting.

Third, the temperature dependence of the resonance wavelength shift of our ring resonator sensors is approximately 50 pm/K, so that temperature noise dominates the noise caused by the optical system and fitting (> 100 fm) starting from temperature noise amplitudes as low as 0.002 K.

In a single ring resonator sensor, the noise in the refractive index of the sample liquid and the temperature noise thus dominate the noise from the optical system. Both scale to a large extent with the slope sensitivity, so that they would also annihilate any enhancement of that parameter. However, on-chip reference ring resonator sensors can compensate both types noise, so that ultimately the noise in the optical system starts determining the limit of detection. Next section describes a possible implementation of these reference sensors, and section 2.4.4 estimates the attainable limit of detection of silicon ring resonator sensors in a system that is limited by optical noise.

2.4.3 Reference sensors

Previous section concluded that noise in the refractive index and temperature of the sample liquid impacts the limit of detection significantly. Two types of reference ring resonator sensors can help to compensate this noise (Figure 2.17):

A general reference sensor without immobilized receptor molecules that is located close to the biosensor and that is in contact with the sample liquid is subject to the same temperature and refractive index noise as the biosensor while not reacting specifically to analyte molecules. Therefore this sensor allows to compensate for both types of noise by subtracting its signal from that of the biosensor. Moreover this type of reference sensors allows to compensate for non-specific binding, an important asset in any biosensing system. However, for some sample liquids the differential refractive index noise between the biosensor and general reference sensor might be large, e.g. due to air bubbles, reducing the reliability of the reference signal.

Therefore it is beneficial to additionally have stable temperature reference sensors that do not react to refractive index noise. Cladding the chip with a transparent material with negligible water absorption that covers the temperature reference sensors, while having windows to the biosensors and general reference sensors, provides a convenient way to make this scheme. The cladding shields the temperature reference sensor's evanescent field from refractive index changes in the liquid, while still allowing it to respond to thermal variations. Regarding the cladding material, K. B. Gylfason et al. [40] and D.-X. Xu et al. [41] employed a silicon-oxide-covered reference ring resonator for temperature compensation. However, reproducibly etching windows through this cladding to

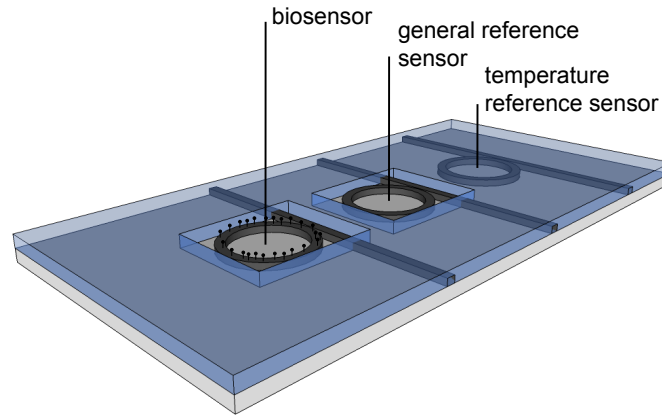


Figure 2.17: Two types of reference sensors allow to compensate (part of) the most dominant noise factors of a ring resonator biosensor. A general reference sensor similar to the biosensor without immobilized receptor molecules allows to compensate both types of noise by subtracting its signal from that of the biosensor. However, its signal might be unreliable due to refractive index changes that differ from those of the biosensor, e.g. due to air bubbles. Therefore, a more stable temperature reference sensor protected by a cladding might be a crucial back-up.

access the other sensors without damaging the silicon-on-insulator waveguides requires an additional silicon nitride etch-stop layer, increasing the number of fabrication steps. A. L. Washburn et al. [42] mentioned the use of a temperature-reference sensor clad with a perfluoro (alkenyl vinyl ether) copolymer.

We identified photopatternable Cyclotene from Dow Chemical [43], a polymer derived from B-staged bisbenzocyclobutene-based (BCB) monomers developed for the micro-electronics industry, as a suitable cladding material, as it is easy to deposit and pattern, and the manufacturer claims it has a low water absorption. Additionally, the thermo-optic coefficient of Cyclotene ($-1.5 \cdot 10^{-4}/K$ [44]) is close to that of water ($-1.1 \cdot 10^{-4}/K$ at 1550 nm [45]), so that the response of the temperature reference sensor and other sensors to temperature variations will be similar. This is especially an asset for the Vernier-cascade sensor that will be presented in chapters 5 and 6.

To verify the suitability of Cyclotene, we fabricated a sensor matrix with

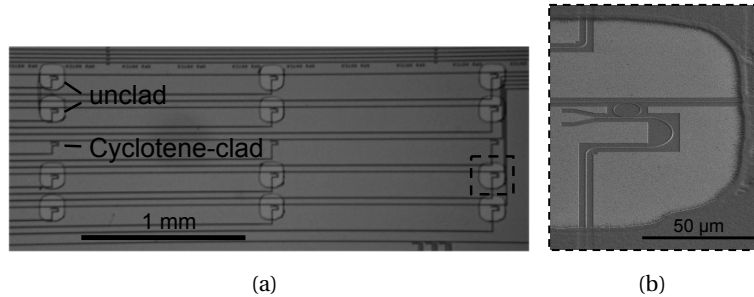


Figure 2.18: Cyclotene, a polymer derived from B-staged bisbenzocyclobutene-based (BCB) monomers developed for the micro-electronics industry, allows to make a sensor matrix with both clad and unclad sensors using a simple fabrication process [43].

both clad and unclad ring resonator sensors (Figure 2.18) using a fabrication process [43] that only involves spin-coating, baking, direct patterning of the cladding with optical lithography and development. The 500 nm-thick cladding is an order of magnitude thicker than the penetration depth of the sensor's evanescent field (64 nm, section 2.3.1), and thus isolates the temperature sensor from the liquid. Only the unclad sensors indeed react to a refractive index change of the liquid, proving the stability of the Cyclotene cladding in a wet environment (Figure 2.19(a)). The resonance wavelength of both sensor types varies linearly with temperature in the most relevant range (Figure 2.19(b)), with a temperature sensitivity of the clad sensor ($65 \text{ pm}/^\circ\text{C}$) close to that of the unclad sensor ($52 \text{ pm}/^\circ\text{C}$). This indicates the potential of Cyclotene for stable reference sensors, both for single ring resonators as for Vernier-cascade sensors.

2.4.4 Attainable limit of detection

When reference sensors sufficiently compensate noise in the refractive index and temperature of the sample liquid, noise on the resonance wavelength extraction from the measured transmission spectra determines the limit of detection of the sensor. This extraction is usually done by fitting a Lorentzian function (section 2.2.3) to a resonance dip, and some properties of the measured spectrum that cause inaccuracies in this fitting are its finite spectral resolution, intensity and wavelength noise, interference fringes and other distortions, e.g. caused by backscattering [18]. If both the biosensor ring resonator and reference ring resonator have a standard

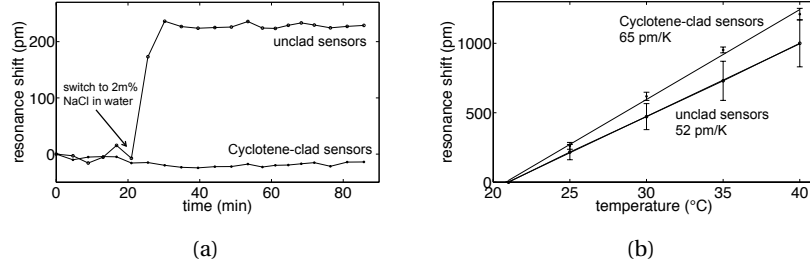


Figure 2.19: (a) Cyclotene-clad sensors do not react to a change of the liquid flow from deionized water to 2 m% of NaCl in water, proving the stability of this cladding in a wet environment. (b) Both types of sensors react similarly to temperature changes, indicating the potential of Cyclotene for stable reference sensors, both for single ring resonators as for Vernier-cascade sensors (chapters 5 and 6).

deviation $\sigma_{\Delta\lambda, optical}$ on their fitted resonance wavelength and the noise between these two resonators is not correlated, the noise on the binding curve has a standard deviation

$$\sqrt{\sigma_{\Delta\lambda, optical}^2 + \sigma_{\Delta\lambda, optical}^2} = \sqrt{2} \cdot \sigma_{\Delta\lambda, optical}$$

since the binding curve originates from the difference between the biosensor and reference sensor signal. The limit of detection then becomes (equations (2.28) and (2.26)):

$$LOD \approx \underbrace{\sqrt{2} \cdot 3.29 \cdot 2 \cdot \sqrt{3}}_{\approx 16} \cdot \frac{\sigma_{\Delta\lambda, optical}}{\sqrt{R_t} \cdot T^{\frac{3}{2}} \cdot S_{slope}} \quad (2.29)$$

with R_t the temporal resolution of the binding curve, T the measurement time, and S_{slope} the slope sensitivity.

A Monte-Carlo simulation with a method similar to the one presented by J. Hu et al [39] allows to estimate the standard deviation on the resonance wavelength extraction $\sigma_{\Delta\lambda, optical}$.

First, the theoretical transmission spectrum of a silicon-on-insulator all-pass ring resonator is calculated with the formulas presented in section 2.2.1, with 11 dB/cm propagation loss (section 2.2.5) and a coupling to obtain a 15 dB on/off-extinction ratio, which is a good value according to J. Hu et al. [39].

Second, Gaussian intensity noise is added to this spectrum. We chose relative intensity noise with 0.01 standard deviation at maximal transmission

to represent noise in the optical alignment. We also added an additional fixed noise floor with 0.001 standard deviation to represent the detector noise, parameters that qualitatively correspond with our measured spectra. No wavelength noise was added, since this is subservient to intensity noise for our resonance widths [39].

Third, a Lorentzian function is fitted to a resonance dip in the noisy spectrum to extract the resonance wavelength. The standard deviation of this fitted resonance wavelength for a thousand instances of noise is a good estimate for the standard deviation on the resonance wavelength extraction $\sigma_{\Delta\lambda, optical}$.

The ring resonator sensor's roundtrip length has a large impact on its limit of detection, since it both influences the temporal resolution through the free spectral range (equation (2.7)) and the noise on the resonance wavelength through the resonance width (equation (2.6)). For a constant propagation loss, the resonance width increases with the roundtrip length, resulting in a monotonous deterioration of the fitting accuracy with increasing roundtrip length (Figure 2.20(a)). However, the temporal resolution is proportional to the roundtrip length through the reduced free spectral range and therefore reduced scan range (section 2.4.2). Hence, the limit of detection of a ring resonator sensor dominated by optical noise (equation (2.29)) first quickly improves with increasing roundtrip lengths, before starting to deteriorate slowly for very large rings (Figure 2.20(b)). For the parameters proposed in section 2.4.2, the limit of detection can become as low as 0.9 fM of streptavidin for 6.7 mm roundtrip length. Experimentally, M. Iqbal et al. measured 60 fM for a ring resonator with much smaller roundtrip length [1].

Note that our very low simulation result is only valid for the ideal case where temperature and refractive index noise in the sample liquid are completely compensated by the reference sensors, where additionally the transmission spectra of the ring resonator does not suffer from interference fringes and other distortions, and only for the extremely high affinity between biotin and streptavidin. Nevertheless, this calculation indicates the potential of the technology and stresses the importance of good reference sensors. Moreover, it suggests that much larger ring resonator sensors can outperform the commonly used small ring resonators through the higher temporal resolution they allow. This is not only a benefit for sensors limited by optical noise, but will also improve those limited by refractive index and temperature noise through a better compensation of fast noise and the smaller time difference between the signals of the biosensor and reference sensor (due to the different

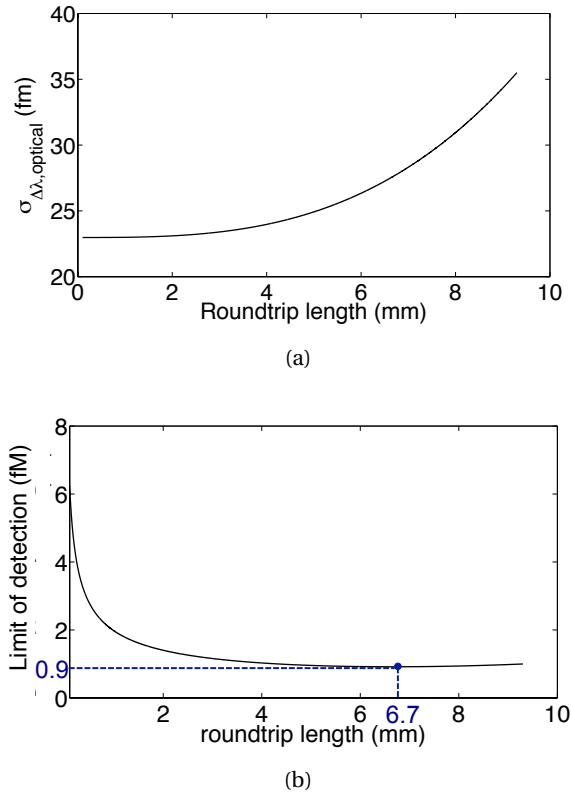


Figure 2.20: (a) Monte-Carlo simulations with a method similar to the one presented by J. Hu et al [39] allow to estimate the standard deviation on the resonance wavelength extraction $\sigma_{\Delta\lambda, \text{optical}}$. For a constant propagation loss of 11 dB/cm and a constant extinction ratio of 15 dB, the resonance width increases with the roundtrip length, resulting in a monotonous deterioration of the fitting accuracy with increasing roundtrip length. (b) Since however the temporal resolution is proportional to the roundtrip length through the reduced free spectral range and therefore reduced scan range, the limit of detection of a ring resonator sensor dominated by optical noise (equation (2.29)) first quickly improves with increasing roundtrip lengths, before starting to deteriorate slowly for very large rings. For a laser scan speed of 10 nm/s, 10 min measurement time and a 0.18 pm/min/pM slope sensitivity for the measurement of the interaction of streptavidin with immobilized biotin (extracted from the measurement data published in [1], see also section 2.4.2), the limit of detection can become as low as 0.9 fM of streptavidin for 6.7 mm roundtrip length.

resonance wavelengths). The large index contrast of silicon-on-insulator allows to reduce the footprint of ring resonators with large roundtrip by folding their cavity [46]. Chapters 5 and 6 present Vernier-cascade sensors with such cavities.

2.5 Size limitation of silicon ring and disk resonator biosensors

Whereas the analysis in previous section focused on ring resonator sensors for achieving low values of the limit of detection, resulting in resonators with large roundtrips, one can envisage applications where the attainable density of the resonator array is more important. The very large index contrast of silicon-on-insulator makes it a very suited material system to make extremely compact structures, and therefore we assessed how small we can make our sensors.

We made several design considerations. First, circular cavities allow the largest possible bend radius for a given area of the cavity, and do not have straight-to-bend transitions that induce mode mismatch loss. Second, a directional coupler that follows the bend of the cavity (Figure 2.21 (a)) provides the required couple length to match the roundtrip loss and achieve critical coupling. Third, microdisk resonators, which can be seen as a special case of ring resonators that consist of a multimode waveguide without inner sidewall (Figure 2.21 (b)), have a fundamental mode with a larger effective refractive index than that of ring resonators, and will therefore have less radiation loss. The multiple supported modes will have very different profiles at very small bend radii, so that in that case the access waveguide can selectively excite the fundamental mode.

We experimentally found that in water the resonances of critically coupled ring resonators start broadening significantly for ring diameters smaller than $5\ \mu\text{m}$ (Figure 2.21(c)). However, critically coupled microdisk resonators in water maintain sharp resonances ($FWHM < 150\ \text{pm}$) down to diameters as small as $3\ \mu\text{m}$. The resonances of our $4\ \mu\text{m}$ -wide critically coupled microdisk resonator sensor (Figure 2.21(b)) with 30 dB extinction are almost as sharp as those of the much larger ring resonators presented before (section 2.2.5), despite the resonator's much smaller size. This makes silicon microdisks very interesting sensors for very dense label-free microarrays.

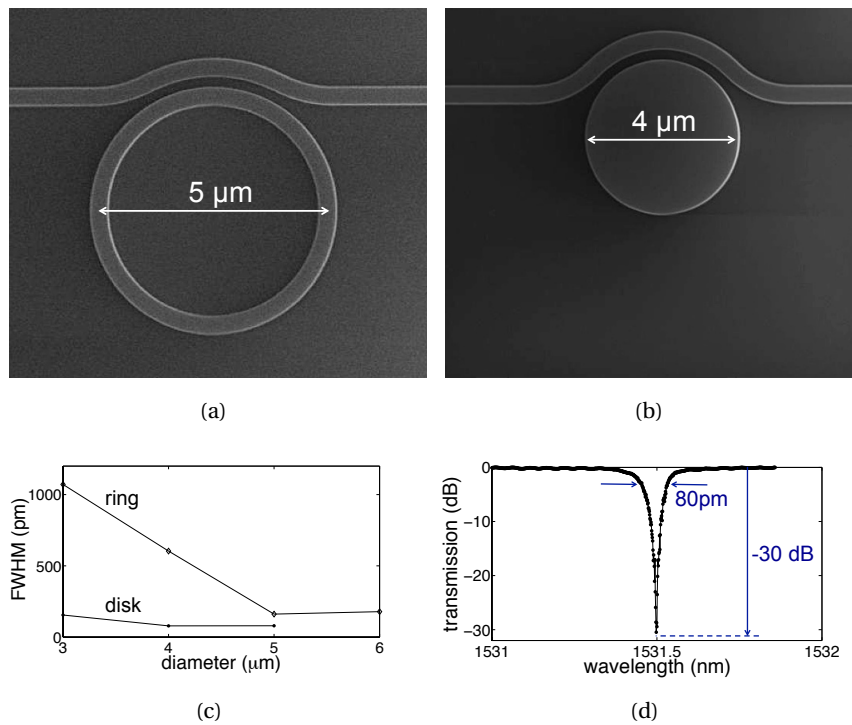


Figure 2.21: (a) and (b): silicon photonic ring and disk resonators can be made very small thanks to the very large refractive index contrast. (c) Whereas ring resonances with large extinction in water start broadening for ring diameters below 5 μm, disk resonances remain very sharp (< 150 pm) down to diameters of only 3 μm. (d) Our critically-coupled 4 μm-wide disk can reach the same quality factors in water as a hundred-times larger ring resonators (section 2.2.5). This example demonstrates the suitability of silicon disk resonators for extremely dense label-free biosensor arrays.

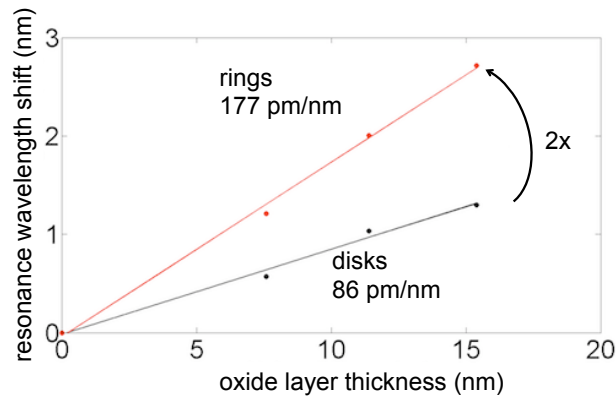


Figure 2.22: Ring resonators are twice as sensitive to refractive index changes at their surface as compared to disk resonators, to a large extent due to the extra evanescent field enhancement at their inner sidewall. Whereas it was measured here in water with silicon dioxide layers deposited with plasma enhanced chemical vapor deposition, a similar scaling is expected for the sensitivity to biochemical interactions at their surface.

However, since microdisks have only one sidewall, and corresponding evanescent field enhancement of the quasi-TE mode, their sensitivity is lower than that of ring resonator sensors. Our measurements confirm this: the resonance wavelength shifts in water of both ring and disk resonators in response to nanometer-sized silicon dioxide layers deposited with plasma enhanced chemical vapor deposition are twice as large for ring resonators compared to disk resonators (Figure 2.22). A similar scaling is expected for their response to biochemical interactions at their surface. Nevertheless, at extremely small diameters ($< 4 \mu\text{m}$) the more noise-resistant sharp resonances of disks are expected to compensate the sensitivity reduction.

2.6 Biochemical surface modification

A biological receptor layer on the surface of a ring resonator sensor selectively binds analyte molecules in complex fluids, and its quality critically determines the performance of the sensor. It has to show a large affinity to the analyte, to obtain a large sensitivity, while maintaining a very low affinity to other molecules in the fluid, to limit non-specific interactions

and consequent false-positive results. Moreover, it is required to be stable, homogeneous and thin (only a few nanometers).

Methods to biochemically modify the surface of silicon waveguides exist, and multiple groups, including ours, have presented multiplexed label-free quantification of proteins [2, 4, 6], DNA [48] and RNA [3]. These surface modification methods can be directly applied to the sensors presented in this thesis, and therefore no new methods are introduced here. The remainder of this section summarizes some widespread techniques to biochemically modify the surface of silicon waveguides, which are described in more detail in chapter 4 of the thesis of K. De Vos [5].

The hydroxyl groups (-OH) of silicon's native oxide are very suited as anchors for the biochemical layer, and their formation can be promoted by submersing the sensor in a mixture of sulfuric acid and hydrogen peroxide (piranha). Silane reagents are then assembled and covalently bound to the surface, providing a smooth surface with functional groups (for example carboxyl or amine groups) to which receptor molecules can attach. A common technique is to activate the surface with N-hydroxysuccinimide (NHS), and bind an outward facing amine group of the receptor to the surface using 1-Ethyl-3-[3-dimethylaminopropyl]carbodiimide Hydrochloride (EDC). Alternatively the receptors can be activated with NHS, after which they are bound to the surface functional groups using EDC. In chapter 4 such a technique is used in the proof-of-concept of slot waveguide ring resonator sensors.

While directly binding receptors to silanes is prevalent, it usually does not yield sufficiently specific sensors. Coating the silane with a hydrophylic polymer such as poly(ethylene glycol) before coupling the receptors enhances the specificity [7].

Multiplexed sensing requires independent surface modification of individual sensors. This can be achieved with molecular printers, such as the *Nano eNabler* or *Bioforce* [49].

2.7 Microfluidics

Microfluidics refers to fluidic handling at length scales below a millimeter. It can be challenging because of the different relative importance of physical effects compared to the macro-scale, resulting from the large surface-to-volume ratio. Integration of functions such as pumping, mix-

ing [50], filtering [51], cell lysis [52] and polymerase chain reaction [53] is intensively researched, and would offer on-chip sample preparation for advanced laboratories-on-a-chip. While this extra functionality would extend the applicability of the ring resonator platform tremendously, its basic operation with controlled delivery of liquids to the sensors suffices for reliable and repeatable measurements.

On-chip microchannels can address all sensors similarly with a laminar flow. Although they can efficiently transport molecules near to the sensor, the flow speed approaches zero close to the chip surface, forming a stagnant liquid layer of a few microns through which the molecules have to diffuse. This limits the mass transport to the sensor. Squires et al. [47] estimate that diffusion in a simple microchannel as ours at concentrations in the order of 1 fM, our best-case value for the limit of detection (section 2.4.4), would approximately result in only one binding event to the sensor per minute. Especially for low-affinity biochemical interactions this will result in a reduced limit of detection, and more advanced mass transport mechanisms could be considered.

For industrial applications the channels are preferably manufactured with a high-volume technique such as injection molding. However, for research a more flexible approach is desired.

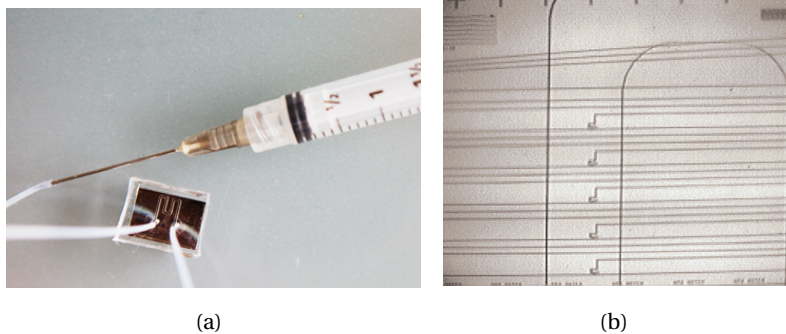


Figure 2.23: A microchannel in polydimethylsiloxane (PDMS) [54] addresses all our ring resonator sensors with a similar laminar flow of the sample liquid. The channel dimensions ($50\ \mu\text{m}$ high and several hundreds of microns wide) aim for small sample volume use, while maintaining an acceptable alignment tolerance. The low-temperature stamp-and-stick packaging method [5, 55] is compatible with biochemical surface modification prior to packaging. Both figures are reproduced, respectively from [6] and [5].

Therefore, we cast our channels in the popular elastomer polydimethylsiloxane (PDMS) [54], and package the chip using the low-temperature stamp-and-stick method introduced by S. Satyanarayana et al. [55] and adapted by K. De Vos from our group [5]. This method is compatible with biochemical surface modification prior to packaging. The channel (Figure 2.23) is only $50\ \mu\text{m}$ high to limit the required liquid volume, and several hundreds of microns wide to be alignment tolerant. It meanders over the different columns of the sensor matrix to address all sensors. All liquids are degassed prior to the experiment by sonication in vacuum to reduce the noise contribution of gas bubbles, and are pushed through the channel with a Harvard syringe pump at a typical flow rate of $5\ \mu\text{L}/\text{min}$.

2.8 Optical interrogation

Highly multiplexed sensing with silicon ring resonator sensors requires simultaneous and robust optical interrogation of tens or even hundreds of sensors on a single chip. An advantageous approach (Figure 2.24) employs on-chip grating couplers to couple light between free space and the ring resonators, allowing alignment tolerant, robust and remote interrogation. While the advanced ring resonator sensors introduced in this thesis are characterized individually, they are compatible with this highly multiplexed interrogation platform.

This section summarizes the working principle and characteristics of grating couplers and discusses the access waveguides that efficiently connect them with the ring resonator sensors (section 2.8.1). It also describes the fiber interrogation technique that is used to characterize the individual sensors in this thesis (section 2.8.2), and reviews two methods for highly multiplexed remote interrogation (2.8.3).

2.8.1 Grating couplers and access waveguides

Efficient coupling to a silicon wire waveguide is not straightforward because of its small core dimensions ($450\ \text{nm} \times 220\ \text{nm}$). Different techniques exist to couple from and to optical fibers at the edge of the chip, but they are either very alignment intolerant or require expensive fabrication steps, making them unsuited for disposable biosensors. Therefore we prefer grating couplers, periodic structures etched in the waveguide that diffract the waveguide mode to a near-vertical direction. They not

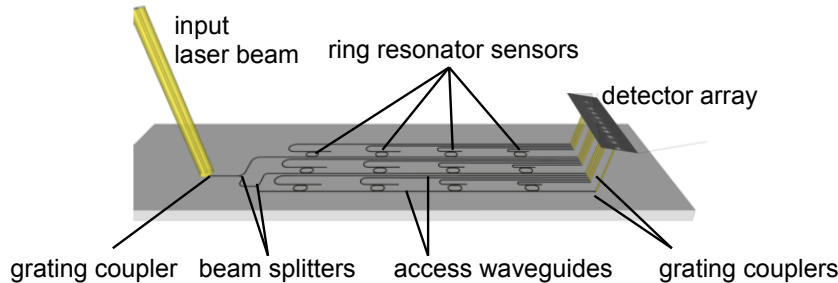


Figure 2.24: Grating couplers allow alignment-tolerant coupling between a waveguide mode and a near-vertical free space beam, and are thus well-suited for robust interrogation. A possible method to simultaneously read-out multiple sensors is to distribute the input power on-chip to all sensors, and monitoring their outputs in parallel with a detector array. This figure is adopted from K. De Vos [5].

only allow alignment tolerant fiber-to-chip coupling (section 2.8.2), but also coupling from and to free space, which is a very large asset for highly multiplexed biosensing (section 2.8.3). Moreover they are made with optical lithography and dry etching together with other on-chip structures, making them very cost effective. They can be placed at any location on the chip, not only at the edges, providing extra design freedom.

The grating couplers employed in this thesis consist of 25 lines with 630nm periodicity etched 70 nm deep in a 10 μm -wide multimode waveguide, which is then adiabatically tapered to the 450 nm-wide wire waveguide. They have an acceptable efficiency (30 % fiber-to-waveguide power efficiency) and bandwidth (40 nm 1 dB bandwidth) for the quasi-TE mode at a wavelength of 1.55 μm and 10° off-vertical coupling angle [57]. More advanced grating couplers [58] are more efficient (70 % fiber-to-waveguide power efficiency) at the cost of extra fabrication steps, while focusing grating couplers consume less space [59].

Access waveguides guide light between each sensor and its input and output grating coupler, so that these three components do not need to be located at the same position. While this offers extra design freedom, it requires efficient waveguides to bridge the distance of often several millimeters without excessive loss. Therefore, the access waveguides of the sensors in this thesis are broadened in the longer straight sections to reduce the impact of sidewall scattering and absorption by water [60]. Adi-

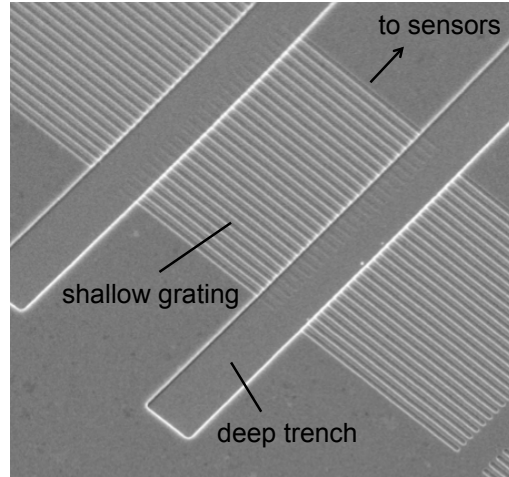


Figure 2.25: Our grating couplers, as pictured on this micrograph adopted from W. Bogaerts et al. [56], consist of 25 lines with 630 nm periodicity etched 70 nm deep in a 10 μm -wide multimode waveguide.

abatic tapering avoids excitation of higher order modes. Alternatively, a single-mode hybrid access waveguide can be used that consists of straight rib sections with only 0.27 dB/cm propagation loss and compact photonic wire bends [61]. This waveguide can be fabricated with the same fabrication steps as the grating couplers, and therefore does not increase the cost.

2.8.2 Fiber interrogation

The input and output signal can be coupled to and from the chip with two single-mode optical fibers that are near-vertically coupled to the corresponding grating couplers. The alignment tolerance is acceptable (2 μm for 1 dB excess loss). A polarization controller adapts the polarization in the input fiber to obtain maximal transmission, which occurs when the polarization of the fiber mode matches that of the quasi-TE mode of the integrated waveguide.

While fiber interrogation is ideal to characterize individual sensors, it is less suited for highly multiplexed sensing. Wavelength division multiplexing allows a limited degree of multiplexing with a single input and output fiber [4, 5], by assigning a wavelength band to each sensor, but this

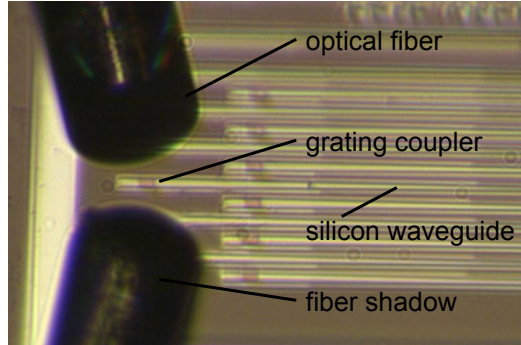


Figure 2.26: A close-to vertically oriented optical fiber can couple light to a single silicon waveguide via a grating coupler. This method is well-suited for characterization of individual sensors, but has drawbacks for a disposable multiplexed sensor system.

cannot be scaled to hundreds of sensors and restricts the sensor design. Interrogation with a fiber array could extend the degree of multiplexing, but at a large cost of more difficult alignment or additional packaging. Hence, next section introduces a remote interrogation method that is better suited for highly multiplexed sensing.

2.8.3 Remote interrogation

A lens system allows to illuminate and monitor multiple grating couplers through free space in a very alignment tolerant way, thus providing a tool for highly multiplexed sensing without requiring wavelength division multiplexing. Furthermore, all fragile optical elements can be kept several centimeters from the chip, making the instrument more robust compared to fiber interrogation.

A first technique proposed by M. Iqbal et al. from the company Genalyte [1] measures the binding curves of multiple sensors simultaneously by sequentially addressing their input grating couplers with the beam of a wavelength-tunable laser and monitoring their output grating couplers with a single shared photodetector. A second technique proposed by K. De Vos from our research group [5, 6] employs beam splitting to address multiple sensors simultaneously, and a detector array or camera to monitor several output grating couplers in parallel. Either one input grating coupler can be used in combination with on-chip splitters, or multiple

grating couplers can be illuminated at once with a broad free-space beam.

Although the sensors presented in this thesis are characterized individually, they can be scaled to a multiplexed platform. All proposed laser-interrogated sensors are compatible with both discussed remote interrogation techniques. The Vernier-cascade sensor with integrated spectral filter that is interrogated with a broadband light source introduced in chapter 6 has multiple output ports that have to be monitored with a detector array or camera.

2.9 Conclusions

Multiplexed label-free biosensing with silicon ring resonator sensors requires more than only a performant transducer. Together with the biochemical surface modification, fluidic sample delivery and optical interrogation it forms a platform that as a whole determines the specifications that are relevant to the user. This becomes clear when looking at the proposed expression of the limit of detection (equation 2.26), which depends on all aspects of the sensor platform. The impact of the novel transducers proposed in this thesis on the performance of the system depends on the other aspects of the platform, hindering a quantitative comparison.

The ring resonator proposed in section 2.2.5 of this chapter has sharper resonances than the one previously proposed by our research group [5, 6, 31], through its all-pass configuration and larger roundtrip. This improves the limit of detection of systems that have a good control or compensation of the refractive index and temperature noise, and that are thus limited by fitting noise.

Some improvements to this ring resonator sensor can be considered. First, when interrogated with a fast wavelength-tunable laser, the sensor benefits from a much larger roundtrip through the reduced free spectral range and consequent improved temporal resolution of the interrogation. Second, employing the quasi-TM mode at smaller wavelengths (for example $1.3\ \mu\text{m}$) can reduce the loss due to absorption and scattering at sidewall roughness. Its lower confinement will increase the sensor's sensitivity to the analyte, but also its sensitivity to refractive index noise, so that the performance of this sensor would depend even more on an accurate compensation mechanism for this type of noise. Chapter 5 proposes a Vernier-cascade sensor that performs this compensation in the optical domain.

Finally, for application in extremely dense label-free biosensor arrays, silicon photonic ring and disk resonators can be made very small thanks to the very large refractive index contrast. Whereas ring resonances with large extinction in water start broadening for ring diameters below $5\ \mu\text{m}$, disk resonances remain very sharp ($< 150\ \text{pm}$) down to diameters of only $3\ \mu\text{m}$. Our critically-coupled $4\ \mu\text{m}$ -wide disk can reach the same quality factors in water as a hundred-times larger ring resonators, albeit at the price of a reduced sensitivity.

References

- [1] Muzammil Iqbal, Martin A. Gleeson, Bradley Spaugh, Frank Tybor, William G. Gunn, Michael Hochberg, Tom Baehr-Jones, Ryan C. Bailey, and L. Cary Gunn. *Label-Free Biosensor Arrays Based on Silicon Ring Resonators and High-Speed Optical Scanning Instrumentation*. IEEE J. Sel. Topics Quantum Electron., 16(3):654–661, May-June 2010.
- [2] Adam L. Washburn, Matthew S. Luchansky, Adrienne L. Bowman, and Ryan C. Bailey. *Quantitative, Label-Free Detection of Five Protein Biomarkers Using Multiplexed Arrays of Silicon Photonic Microring Resonators*. Analytical Chemistry, 82(1):69–72, Jan 2010.
- [3] Abraham J. Qavi and Ryan C. Bailey. *Multiplexed Detection and Label-Free Quantitation of MicroRNAs Using Arrays of Silicon Photonic Microring Resonators*. Angewandte Chemie, 49(27):4608–4611, 2010.
- [4] D. X. Xu, M. Vachon, A. Densmore, R. Ma, A. Delage, S. Janz, J. Lapointe, Y. Li, G. Lopinski, D. Zhang, Q. Y. Liu, P. Cheben, and J. H. Schmid. *Label-free biosensor array based on silicon-on-insulator ring resonators addressed using a WDM approach*. Opt. Lett., 35(16):2771–2773, Aug 2010.
- [5] Katrien De Vos. *Label-free Silicon Photonics Biosensor Platform with Microring Resonators*. PhD thesis, Universiteit Gent, 2010.
- [6] K. De Vos, J. Girones, T. Claes, Y. De Koninck, S. Popelka, E. Schacht, R. Baets, and P. Bienstman. *Multiplexed Antibody Detection With an Array of Silicon-on-Insulator Microring Resonators*. IEEE Photon. J., 1(4):225–235, Oct. 2009.
- [7] Katrien De Vos, Jordi Girones, Stepan Popelka, Etienne Schacht, Roel Baets, and Peter Bienstman. *SOI optical microring resonator with poly(ethylene glycol) polymer brush for label-free biosensor applications*. Biosens Bioelectron, 24(8):2528–33, Apr 2009.
- [8] Govind P. Agrawal. *Fiber-optic Communication Systems*. Wiley Series in Microwave and Optical Engineering, 2002.
- [9] www.soitec.com.
- [10] www.epixfab.eu.
- [11] Shankar Kumar Selvaraja, Patrick Jaenen, Wim Bogaerts, Dries Van Thourhout, Pieter Dumon, and Roel Baets. *Fabrication of Photonic*

- Wire and Crystal Circuits in Silicon-on-Insulator Using 193-nm Optical Lithography*. J. Lightw. Technol., 27(18):4076–4083, 2009.
- [12] Shankar Kumar Selvaraja. *Wafer-Scale Fabrication Technology for Silicon Photonic Integrated Circuits*. PhD thesis, Universiteit Gent, 2011.
- [13] Hui Su and Xu Guang Huang. *Fresnel-reflection-based fiber sensor for on-line measurement of solute concentration in solutions*. Sens. Actuators, B, 126(2):579–582, OCT 1 2007.
- [14] Wim Bogaerts, Peter De Heyn, Thomas Van Vaerenbergh, Katrien De Vos, Shankar Kumar Selvaraja, Tom Claes, Pieter Dumon, Peter Bienstman, Dries Van Thourhout, and Roel Baets. *Silicon microring resonators*. Laser & Photonics Reviews, 6(1):47–73, January 2012.
- [15] Pieter Dumon. *Ultra-Compact Integrated Optical Filters in Silicon-on-insulator by Means of Wafer-Scale Technology*. PhD thesis, Universiteit Gent, 2007.
- [16] KK Lee, DR Lim, HC Luan, A Agarwal, J Foresi, and LC Kimerling. *Effect of size and roughness on light transmission in a Si/SiO₂ waveguide: Experiments and model*. Applied Physics Letters, 77(11):1617–1619, September 2000.
- [17] T Barwicz and HA Haus. *Three-dimensional analysis of scattering losses due to sidewall roughness, in microphotonic waveguides*. Journal of Lightwave Technology, 23(9):2719–2732, September 2005.
- [18] F Morichetti, a. Canciamilla, M. Martinelli, a. Samarelli, R. M. De La Rue, M. Sorel, and a. Melloni. *Coherent backscattering in optical microring resonators*. Applied Physics Letters, 96(8):081112, 2010.
- [19] KF PALMER and D WILLIAMS. *Optical-properties of water in near-infrared*. Journal of the Optical Society of America, 64(8):1107–1110, 1974.
- [20] D. G. Rabus. *Integrated Ring Resonators*. Springer series in optical sciences, 2007.
- [21] John Heebner, Rohit Grover, and Tarek Ibrahim. *Optical microresonators*. Springer series in optical sciences, 2008.
- [22] B.E. Little, J.S. Foresi, G. Steinmeyer, E.R. Thoen, S.T. Chu, H.A. Haus, E.P. Ippen, L.C. Kimerling, and W. Greene. *Ultra-compact Si-SiO₂*

- microring resonator optical channel dropping filters*. IEEE Photonics Technology Letters, 10(4):549–551, apr 1998.
- [23] Fengnian Xia, Lidija Sekaric, and Yurii Vlasov. *Ultracompact optical buffers on a silicon chip*. Nature Photonics, 1(1):65–71, JAN 2007.
- [24] Brian R. Koch, Alexander W. Fang, Oded Cohen, and John E. Bowers. *Mode-locked silicon evanescent lasers*. Opt. Express, 15(18):11225–11233, Sep 2007.
- [25] S. L. McCall, A. F. J. Levi, R. E. Slusher, S. J. Pearton, and R. A. Logan. *Whispering-gallery mode microdisk lasers*. Applied Physics Letters, 60(3):289–291, January 1992.
- [26] Qianfan Xu, Sasikanth Manipatruni, Brad Schmidt, Jagat Shakya, and Michal Lipson. *12.5 Gbit/s carrier-injection-based silicon micro-ring silicon modulators*. Opt. Express, 15(2):430–436, Jan 2007.
- [27] P. D. Trinh, S. Yegnanarayanan, and B. Jalali. *Integrated optical directional-couplers in silicon-on-insulator*. Electronics Letters, 31(24):2097–2098, November 1995.
- [28] P Dumon, W Bogaerts, V Wiaux, J Wouters, S Beckx, J Van Campenhout, D Taillaert, B Luysaert, P Bienstman, D Van Thourhout, and R Baets. *Low-loss SOI photonic wires and ring resonators fabricated with deep UV lithography*. Ieee Photonics Technology Letters, 16(5):1328–1330, May 2004.
- [29] Dan-Xia Xu, Adam Densmore, Philip Waldron, Jean Lapointe, Edith Post, Andre Delage, Siegfried Janz, Pavel Cheben, Jens H. Schmid, and Boris Lamontagne. *High bandwidth SOI photonic wire ring resonators using MMI couplers*. Optics Express, 15(6):3149–3155, March 2007.
- [30] W. R. McKinnon, D. X. Xu, C. Storey, E. Post, A. Densmore, A. Delâge, P. Waldron, J. H. Schmid, and S. Janz. *Extracting coupling and loss coefficients from a ring resonator*. Opt. Express, 17(21):18971–18982, 2009.
- [31] Katrien De Vos, Irene Bartolozzi, Etienne Schacht, Peter Bienstman, and Roel Baets. *Silicon-on-Insulator microring resonator for sensitive and label-free biosensing*. Optics Express, 15(12):7610–7615, JUN 11 2007.
- [32] A. Densmore, D. X. Xu, P. Waldron, S. Janz, P. Cheben, J. Lapointe, A. Delage, B. Lamontagne, J. H. Schmid, and E. Post. *A silicon-on-*

- insulator photonic wire based evanescent field sensor*. IEEE Photonics Technology Letters, 18(21-24):2520–2522, NOV-DEC 2006.
- [33] Matthew S. Luchansky, Adam L. Washburn, Teresa A. Martin, Muzaamil Iqbal, L. Cary Gunn, and Ryan C. Bailey. *Characterization of the evanescent field profile and bound mass sensitivity of a label-free silicon photonic microring resonator biosensing platform*. Biosensors and Bioelectronics, 26(4):1283 – 1291, 2010.
- [34] Jacob T. Robinson, Kyle Preston, Oskar Painter, and Michal Lipson. *First-principle derivation of gain in high-index-contrast waveguides*. Optics Express, 16(21):16659–16669, October 2008.
- [35] Richard B M Schasfoort and Anna J Tudos, editors. *Handbook of surface plasmon resonance*. RSCPublishing, 2008.
- [36] LA Currie. *Detection: International update, and some emerging dilemmas involving calibration, the blank, and multiple detection decisions*. Chemometrics and Intelligent Laboratory Systems, 37(1):151–181, May 1997.
- [37] Matthew S. Luchansky and Ryan C. Bailey. *Silicon Photonic Microring Resonators for Quantitative Cytokine Detection and T-Cell Secretion Analysis*. Analytical Chemistry, 82(5):1975–1981, MAR 1 2010.
- [38] Matthew S. Luchansky, Adam L. Washburn, Melinda S. McClellan, and Ryan C. Bailey. *Sensitive on-chip detection of a protein biomarker in human serum and plasma over an extended dynamic range using silicon photonic microring resonators and sub-micron beads*. Lab on a Chip, 11(12):2042–2044, 2011.
- [39] Juejun Hu, Xiaochen Sun, Anu Agarwal, and Lionel C. Kimerling. *Design guidelines for optical resonator biochemical sensors*. Journal of the Optical Society of America B, 26(5):1032–1041, 2009.
- [40] Kristinn B. Gylfason, Carl F. Carlborg, Andrzej Kazmierczak, Fabian Dortu, Hans Sohlström, Laurent Vivien, Carlos A. Barrios, Wouter van der Wijngaart, and Göran Stemme. *On-chip temperature compensation in an integrated slot-waveguide ringresonator refractive index sensor array*. Opt. Express, 18(4):3226–3237, 2010.
- [41] D-X Xu, M. Vachon, A. Densmore, R. Ma, S. Janz, A. Delage, J. Lapointe, P. Cheben, J. H. Schmid, E. Post, Sonia Messaoudene, and Jean-Marc Fedeli. *Real-time cancellation of temperature induced reso-*

- nance shifts in SOI wire waveguide ring resonator label-free biosensor arrays.* Optics Express, 18(22):22867–22879, Oct 2010.
- [42] Adam L. Washburn, L. Cary Gunn, and Ryan C. Bailey. *Label-Free Quantitation of a Cancer Biomarker in Complex Media Using Silicon Photonic Microring Resonators.* Analytical Chemistry, 81(22):9499–9506, 10 2009.
- [43] <http://www.dow.com/cyclotene/>.
- [44] Kesavan S/O Ulaganathen. *Attenuation Measurement On Cyclotene (Bcb Photo Resin) Polymer Based Slab Waveguide.* Master's thesis, Faculty of Electrical Engineering, Universiti Teknologi Malaysia, 2005.
- [45] Chang-Bong Kim and Chin B Su. *Measurement of the refractive index of liquids at 1.3 and 1.5 micron using a fibre optic Fresnel ratio meter.* Measurement Science and Technology, 15(9):1683, 2004.
- [46] D. X. Xu, A. Densmore, A. Del age, P. Waldron, R. McKinnon, S. Janz, J. Lapointe, G. Lopinski, T. Mischki, E. Post, P. Cheben, and J. H. Schmid. *Folded cavity SOI microring sensors for high sensitivity and real time measurement of biomolecular binding.* Optics Express, 16(19):15137–15148, 2008.
- [47] Todd M. Squires, Robert J. Messinger, and Scott R. Manalis. *Making it stick: convection, reaction and diffusion in surface-based biosensors.* NATURE BIOTECHNOLOGY, 26(4):417–426, APR 2008.
- [48] Abraham J Qavi, Thomas M Mysz, and Ryan C Bailey. *Isothermal Discrimination of Single-Nucleotide Polymorphisms via Real-Time Kinetic Desorption and Label-Free Detection of DNA Using Silicon Photonic Microring Resonator Arrays.* Analytical Chemistry, 83(17):6827–6833, September 2011.
- [49] www.bioforcenano.com.
- [50] Alan Renaudin, Vincent Chabot, Etienne Grondin, Vincent Aimez, and Paul G. Charette. *Integrated active mixing and biosensing using surface acoustic waves (SAW) and surface plasmon resonance (SPR) on a common substrate.* Lab On a Chip, 10(1):111–115, 2010.
- [51] Xing Chen, Dafu Cui, and Jian Chen. *Design, fabrication and characterization of nano-filters in silicon microfluidic channels based on MEMS technology.* Electrophoresis, 30(18):3168–3173, September 2009.

- [52] Chen Xing, Cui Dafu, Liu Changchun, and Cai Haoyuan. *Microfluidic biochip for blood cell lysis*. Chinese Journal of Analytical Chemistry, 34(11):1656–1660, November 2006.
- [53] CS Zhang, JL Xu, WL Ma, and WL Zheng. *PCR microfluidic devices for DNA amplification*. Biotechnology Advances, 24(3):243–284, May-Jun 2006.
- [54] JC McDonald, DC Duffy, JR Anderson, DT Chiu, HK Wu, OJA Schueller, and GM Whitesides. *Fabrication of microfluidic systems in poly(dimethylsiloxane)*. Electrophoresis, 21(1):27–40, January 2000.
- [55] S Satyanarayana, RN Karnik, and A Majumdar. *Stamp-and-stick room-temperature bonding technique for microdevices*. Journal of Microelectromechanical Systems, 14(2):392–399, April 2005.
- [56] W. Bogaerts, D. Taillaert, B. Luyssaert, P. Dumon, J. Van Campenhout, P. Bienstman, D. Van Thourhout, R. Baets, V. Wiaux, and S. Beckx. *Basic structures for photonic integrated circuits in Silicon-on-insulator*. Opt. Express, 12(8):1583–1591, 2004.
- [57] W Bogaerts, R Baets, P Dumon, V Wiaux, S Beckx, D Taillaert, B Luyssaert, J Van Campenhout, P Bienstman, and D Van Thourhout. *Nanophotonic waveguides in silicon-on-insulator fabricated with CMOS technology*. Journal of Lightwave Technology, 23(1):401–412, January 2005.
- [58] D. Vermeulen, S. Selvaraja, P. Verheyen, G. Lepage, W. Bogaerts, P. Absil, D. Van Thourhout, and G. Roelkens. *High-efficiency fiber-to-chip grating couplers realized using an advanced CMOS-compatible Silicon-On-Insulator platform*. Optics Express, 18(17):18278–18283, August 2010.
- [59] Frederik Van Laere, Tom Claes, Jonathan Schrauwen, Stijn Scheerlinck, Wim Bogaerts, Dirk Taillaert, Liam O’Faolain, Dries Van Thourhout, and Roel Baets. *Compact focusing grating couplers for silicon-on-insulator integrated circuits*. IEEE Photonics Technology Letters, 19(21-24):1919–1921, NOV-DEC 2007.
- [60] Wim Bogaerts, Shankar Kumar Selvaraja, Pieter Dumon, Joost Brouckaert, Katrien De Vos, Dries Van Thourhout, and Roel Baets. *Silicon-on-Insulator Spectral Filters Fabricated With CMOS Technology*. IEEE J. Sel. Topics Quantum Electron., 16(1):33–44, JAN-FEB 2010.

- [61] W. Bogaerts and S. K. Selvaraja. *Compact Single-Mode Silicon Hybrid Rib/Strip Waveguide With Adiabatic Bends*. Ieee Photonics Journal, 3(3):422–432, June 2011.

3

Dual polarization ring resonator sensor

Most evanescent wave biosensors, including surface plasmon sensors and the other silicon photonic sensors presented in this thesis, only measure the interaction of a single optical mode with a biochemical layer, thus only providing information on the combined change of the refractive index and thickness of the layer, without being able to distinguish between these two effects. Nevertheless, a disentanglement of these parameters would yield information on the molecular structure, such as DNA orientation and protein conformation, which is of great interest in the study of biomolecular interactions and which has already proven to play an important role in several cancers and in Alzheimer's disease [1].

An example of a commercial label-free biosensor that can accurately distinguish between the refractive index and thickness of a biomolecular layer is the *Analight* Dual Polarization Interferometer from Farfield Scientific Ltd. [2]. It is a Young interferometer-based sensor in which two orthogonally polarized modes interact with the molecules. Molecular binding will have a different impact on the effective refractive index of each of the modes due to their different profiles, thus providing two equa-

tions for the two unknowns, the biomolecular layer refractive index and thickness. The *Analight* Dual Polarization Interferometer has already been proven useful in the study of the impact of small molecules on the structure of DNA [3] and in the research of protein conformational changes [4]. However, it is not compatible with a highly multiplexed sensor platform and has a limited throughput. Recently (early 2012) the sales of this instrument have been discontinued.

Silicon photonic biosensors have the potential to miniaturize and further integrate dual polarization sensing, since they can support multiple modes and allow highly multiplexed sensing. Katrien De Vos theoretically studied the applicability of silicon photonic ring resonators for dual polarization sensing at Ghent University [5], and concluded that a similar performance as the *Analight* can be obtained with an optimized waveguide design. However, exciting both polarizations simultaneously in a ring resonator is not trivial, and a working prototype was still lacking. We investigated two possible implementations, fabricated with a low-cost standard process, and performed calculations and experiments to study their applicability.

This chapter first explains the working principle of dual polarization sensing with a ring resonator (section 3.1), after which it introduces a model (section 3.2) that allows to calibrate the sensor and to calculate a layer's refractive index and thickness from measured resonance wavelength shifts. Section 3.3 discusses the achievable accuracy of a silicon dual polarization sensor composed of easy-to-fabricate waveguides, and section 3.4 compares two implementations. Section 3.5 presents an experimental proof-of-concept of one of these implementations.

3.1 Working principle

For dual polarization sensing, both the fundamental quasi-TE and quasi-TM modes are excited in a silicon ring resonator. If the waveguide is highly birefringent, the modes will be efficiently decoupled and will resonate independently at different resonance wavelengths. Because both modes have a different field distribution, their resonance wavelengths will shift differently when biomolecules interact at the sensor surface. A model of the sensor describing the resonance wavelength shifts for both modes as a function of layer refractive index and thickness can be uniquely solved for the layer properties, given the measured resonance wavelengths. The

model can be an analytical function of which the parameters are determined either based on a simulation or a calibration measurement. Next section will introduce and describe a possible model for silicon ring resonator sensors.

Information on both the layer refractive index and thickness can give additional insight into the measured biomolecular interactions. The layer refractive index n_l is representative for the molecular density ρ_l via [5, 6]:

$$\rho_l = \rho_{molecule} \cdot \frac{n_l - n_w}{n_{molecule} - n_w}$$

with $\rho_{molecule}$ and $n_{molecule}$ respectively the density (g/cm^3) and refractive index of the molecules in dry state, and n_w the refractive index of the watery buffer. In literature, values for $n_{molecule}$ are reported between 1.45 and 1.48 for both proteins [7] and DNA [8], a value of $1.64 g/cm^3$ can be found for ρ_{DNA} [9], while values for $\rho_{protein}$ vary between $0.71 g/cm^3$ [10] and $1.33 g/cm^3$ [11, 12].

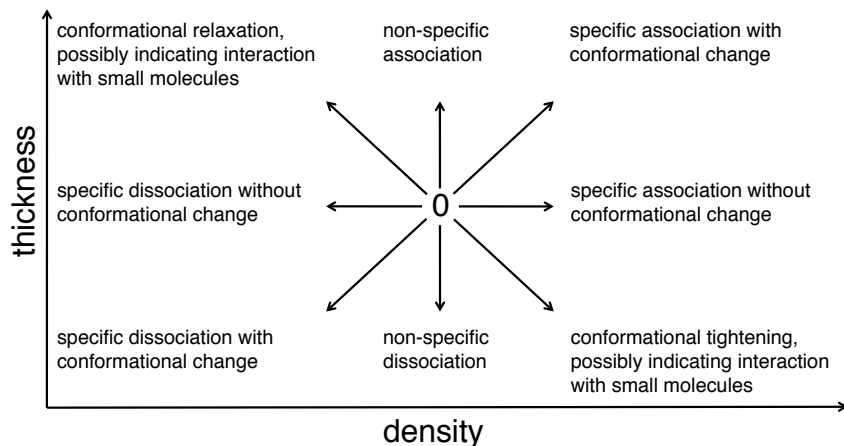


Figure 3.1: Dual polarization sensing allows to independently measure the thickness and density of a biomolecular layer, which provides additional insight in the measured interactions as visualized in this matrix, reproduced from M. Swann et al. [13].

As proposed by M. Swann et al. [13], the interpretation of changes in the layer thickness and density for biomolecular interactions can be visualized in a matrix (Fig. 3.1). An increase/decrease of both parameters signifies a specific association/dissociation of molecules with a conformational change, while a change of only the density indicates specific

interactions without changes in the molecular structures. A change of only the thickness, signals non-specific addition or removal of material. Interactions with small molecules often lead to structural changes of the immobilized molecules, resulting in an opposite variation of the thickness and density. Measuring with two polarizations can thus yield important additional information on the relation between the structure and function of a molecule.

3.2 Analytical model

An analytical model that describes the resonance shifts of both modes as a function of the refractive index and thickness of thin layers on the resonator waveguide allows to calibrate the sensor. This can be done by choosing the model parameters such that they best fit simulated or measured resonance shifts corresponding to layers of known refractive index and thickness. After calibration, the refractive index and thickness of unknown layers can be determined by solving the model with measured resonance wavelength shifts. A first part of this section describes the construction of the model, whereas a second part validates the model with simulations.

First, the shift is required to be zero independent of the layer thickness, when the layer refractive index is equal to that of the watery buffer environment. Second, the shift needs to be zero independent of the layer refractive index if the layer thickness is zero, giving it the following form:

$$\begin{aligned}\Delta\lambda_{TE}(n, t) &= t \cdot (n - n_w) \cdot f_{TE}(n, t) \\ \Delta\lambda_{TM}(n, t) &= t \cdot (n - n_w) \cdot f_{TM}(n, t)\end{aligned}$$

with $\Delta\lambda_{TE}$ and $\Delta\lambda_{TM}$ the resonance wavelength shifts of the quasi-TE and quasi-TM modes, n and t the layer refractive index and thickness, n_w the refractive index of the watery environment and $f_{TE}(n, t)$ and $f_{TM}(n, t)$ so far unknown functions. For very thin layers and small changes of the refractive index that only have a small impact on the mode profiles, the resonance wavelength shift is expected to be linear in both parameters. However, simulations with the eigenmode expansion solver *Fimmwave* showed that in the relevant range of thickness (0 to 25 nm) and refractive index (1.31 till 2.0) for the proof-of-concept experiment described later, the resonance wavelength shift appeared *not* to be linear as a function of the layer refractive index and thickness. Therefore the following model is

proposed:

$$\begin{aligned}\Delta\lambda_{TE}(n, t) &= a_{TE} t (n - n_w)^2 + b_{TE} t^2 (n - n_w) + c_{TE} t (n - n_w) \\ \Delta\lambda_{TM}(n, t) &= a_{TM} t (n - n_w)^2 + b_{TM} t^2 (n - n_w) + c_{TM} t (n - n_w)\end{aligned}\quad (3.1)$$

This is an easy-to-fit polynomial model that is quadratic along the t -axis and n -axis, and that has 7 parameters (a_{TE} , b_{TE} , c_{TE} , a_{TM} , b_{TM} , c_{TM} and n_w). The refractive index of the watery environment n_w is taken as a parameter and not as a constant, since in an experiment this value is usually not known with sufficient accuracy.

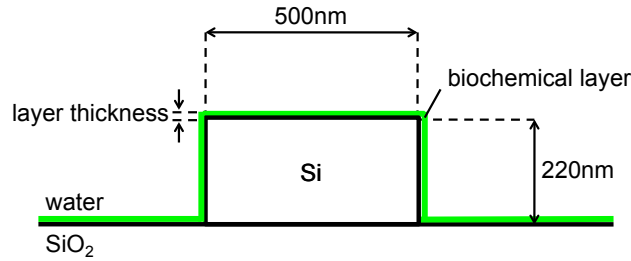


Figure 3.2: The influence on the effective refractive index and group refractive index of a thin biochemical layer covering the complete waveguide was simulated with the eigenmode expansion solver *Fimmwave*, using the layer refractive index and thickness as parameters.

To validate the model, it was proven that it fits simulated resonance wavelength shifts very well. The effective refractive index and group index of the quasi-TE and quasi-TM modes of a common 500 nm wide and 220 nm high silicon wire were simulated with the eigenmode expansion solver *Fimmwave*, and this for multiple values of the refractive index and thickness of a thin layer covering the waveguide. The resonance wavelength shift of a resonator composed of this waveguide was then calculated with (equation 2.22 in chapter 2, derived in appendix C):

$$\Delta\lambda(n, t) = \frac{(n_{eff}(n, t) - n_{eff,0}) \cdot \lambda}{n_g}$$

with $n_{eff}(n, t)$ the simulated effective refractive index of the waveguide mode (TE or TM) when the waveguide is covered with a layer with refractive index n and thickness t , $n_{eff,0}$ the simulated effective refractive index when no layer is present and n_g the group index. Using a standard nonlinear regression algorithm, both equations of the model are fitted

together in a least-square sense to the resulting set of simulated resonance wavelength shifts for both polarizations. Visually the model fits the data set very well (Figure 3.3). A quantitative measure for the quality of fit is given by the R^2 goodness-of-fit

$$R^2 = 1 - \frac{SS_{fit}}{SS_{mean}}$$

with SS_{fit} the square distance between the simulated resonance wavelength shifts and the model and SS_{mean} the square distance between the simulated shifts and their mean, so that R^2 is a measure for how much better the model fits the data compared to a horizontal plane through the mean. The model given by equations (3.1) fits the simulated resonance wavelength shifts with a very high value ($R^2 = 0.9999$).

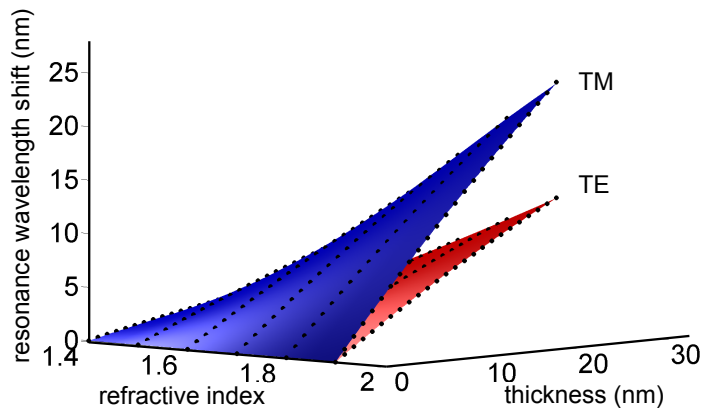


Figure 3.3: A simulation shows that the quasi-TM mode of a resonator consisting of a standard silicon wire waveguide (500 nm wide and 220 nm high) is more sensitive to changes of a layer on the waveguide than the quasi-TE mode, as expected from their different field profiles and confinement and as desired to differentiate between the refractive index and thickness of the layer. The validity of model (3.1) is confirmed by its excellent fit (surfaces) to the simulated shifts (dots), with a R^2 goodness-of-fit value as high as 0.9999.

3.3 Estimation of the accuracy

Previous section presented an analytical model describing the ring resonator sensor's response to layers with different refractive index and thickness. It allows to calibrate the sensor based on measured or simulated resonance wavelength shifts for layers with known refractive index and thickness, after which it admits to unambiguously determine these properties for unknown layers. However, uncertainty on the resonance wavelength shifts limits the accuracy of both the calibration and layer property determination. This section first analyzes the impact of resonance wavelength noise on the calibration, including an estimation of the required amount of calibration points to keep the systematic error at an acceptable level. Second, it studies the accuracy of the refractive index and thickness determination after calibration.

In [5], a numerical study indicates that the optimal silicon wire waveguide for dual polarization sensing is 240 nm wide and 280 nm high. However, this waveguide cannot be fabricated with our standard fabrication process and moreover its low birefringence will induce unwanted polarization coupling in the resonator bends [14]. Therefore, this study focuses on an easy-to-fabricate and highly birefringent 500 nm wide and 220 nm high silicon photonic wire that corresponds with the waveguide employed in the experimental study reported in the next section.

Before the sensor can measure the refractive index and thickness of unknown layers, it has to be calibrated either by simulation or by measuring the resonance wavelength shifts of layers with known properties. Calibration based on simulations is straightforward, but care must be taken that the simulation method takes sufficient sensor properties into account, such as the inclination of the waveguide sidewalls. If the sensor is calibrated by measurements, noise on this measurement results in uncertainty on the fitted model parameters, of which an error translates in systematic errors in the refractive index and thickness determination. The amount of noise heavily depends on the measurement platform, including the use of reference sensors to compensate for temperature-induced noise, mechanical stability and the wavelength accuracy of the laser scanning. M. Iqbal et al. [15] reported an experimentally determined resonance wavelength noise as low as 220 fm for the quasi-TE resonances of a silicon ring resonator sensor composed of a similar waveguide as studied here. Assuming Gaussian resonance wavelength noise with 220 fm standard deviation for both modes in our dual polarization sensor, the average systematic error on the refractive index (Figure 3.4(a)) and thick-

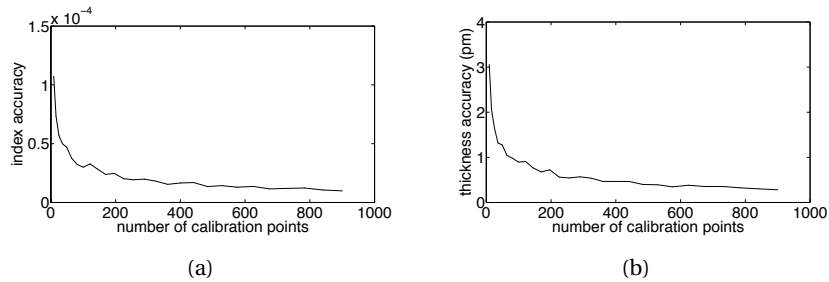


Figure 3.4: Assuming Gaussian resonance wavelength noise with 220fm standard deviation on the calibration points, the average systematic error on the refractive index (a) and thickness determination (b) due to calibration decreases with the number of calibration points as expected, with acceptable accuracies starting after as little as 16 calibration points (less than $1 \cdot 10^{-4}$ RIU and 3 pm inaccuracy on the refractive index and thickness determination respectively). Over 400 calibration points the impact of extra calibration becomes negligible.

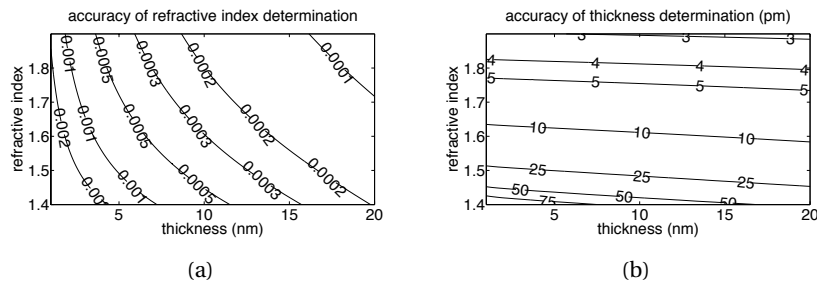


Figure 3.5: Assuming a perfect calibration and a standard deviation of 220 fm on the resonance wavelength shifts, the absolute accuracy of the layer refractive index (a) and thickness determination (b) improves with thickness and refractive index, as expected. The layer refractive index has a much larger impact on the thickness accuracy than the layer thickness.

ness determination (Figure 3.4(b)) due to calibration decreases with the number of calibration points as expected, with acceptable accuracies starting after as little as 16 calibration points (less than $1 \cdot 10^{-4}$ RIU and 3 pm inaccuracy on the refractive index and thickness determination respectively). With more than 400 calibration points the impact of extra calibration becomes negligible.

Once the sensor is calibrated, the uncertainty on the measured resonance wavelength shifts for unknown layers translates into an inaccuracy of the refractive index and thickness determination. Assuming a deviation of 220 fm on this measurement, the maximum error on both the refractive index (Figure 3.5(a)) and thickness determination (Figure 3.5(b)) decreases with increasing layer refractive index and thickness, as can be expected from the larger mode fraction present in the layer. For biosensing, approximately 5 nm thick layers with a refractive index around 1.45 are of interest, which can be measured with an accuracy up to $1.5 \cdot 10^{-3}$ RIU and 50 pm. Although this accuracy is insufficient to quantitatively measure conformational changes of proteins, it might be enough to qualitatively detect such a change. For folding and unfolding of proteins, an accuracy between 500 pm and 1 nm is sufficient, indicating the applicability of this silicon dual polarization ring resonator sensor.

3.4 Implementation

Dual polarization sensing requires simultaneous and accurate measurement of the resonance wavelength shifts of both the fundamental quasi-TE and quasi-TM modes in a single ring resonator, which entails close-to-critical coupling of these modes to one or more access waveguide modes (section 2.4.2 in chapter 2). The difference in confinement, coupling and propagation losses of the two modes make this into a challenging design requirement, and we evaluated different options for implementation. First this section reports on an implementation with two access waveguides that each guide and couple one of the modes, but that design suffers from the different propagation and coupling losses of the two modes. Second, a more advantageous implementation is proposed that only involves one access waveguide and a dual polarization directional coupler that couples the quasi-TE mode of the access waveguide with both modes of the ring resonator. Section 3.5 describes the use of this second implementation for a proof-of-concept experiment of dual polarization sensing.

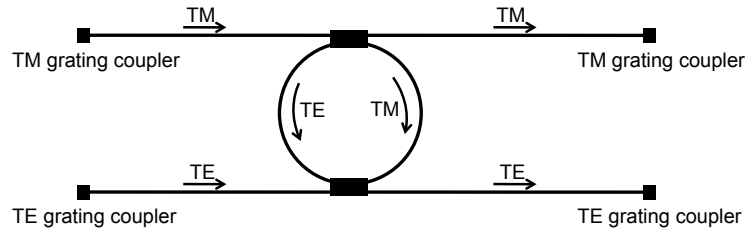


Figure 3.6: The quasi-TE and quasi-TM modes can be excited in the same ring resonator by means of two access waveguides that each guide and couple one of the modes. When the coupling of each of the modes approximately matches its roundtrip loss, the transmission of the access waveguides will display clearly visible resonance dips for the corresponding polarization. Only the intended mode is coupled in and out of the access waveguides by providing them with different polarization selective grating couplers. Illumination of both input grating couplers with a broad laser beam that has field components for both polarizations allows to simultaneously excite the two resonator modes, of which the resonances can be monitored in parallel with a detector array.

3.4.1 Implementation with two access waveguides

A straightforward implementation (Figure 3.6) is to use two access waveguides that each guide and couple one of the two modes to the ring resonator, that will then resonate in opposite directions. The access waveguides have different grating couplers that only couple to the intended mode for the waveguide, in the applied range of wavelengths and angles of incidence. Illumination of both input grating couplers with a broad laser beam that is polarized so that it has both TE and TM field components, allows simultaneous excitation of both access waveguide modes. The transmission spectra of both access waveguides will contain resonance dips for the corresponding mode, which can be monitored in parallel with a detector array. This scheme is compatible with simultaneous interrogation of multiple sensors (section 2.8.3 in chapter 2), which is required for multiplexed sensing.

The directional couplers need to be designed so that for both modes the coupled power matches the roundtrip loss (section 2.2.2 in chapter 2), since both modes are required to have a large extinction to allow accurate monitoring of resonance wavelength shifts. However, the different field profiles of the quasi-TE and quasi-TM modes in the ring waveguide cause them to have very different coupling strengths in a directional coupler.

We propose two equal directional couplers that for both modes couple the power required for close-to critical coupling, despite the different coupling strength, by employing the periodic power transfer in a directional coupler (Fig. 3.7). While the power of the strongly coupled quasi-TM mode is coupled back-and-forth the two waveguides, the power transfer of the weakly coupled quasi-TE mode can build-up. By choosing the appropriate distance between the waveguides and the appropriate coupler length, the required power for both modes can be coupled to the ring resonator.

A silicon photonic implementation (Figure 3.8) confirms that this concept allows to accurately monitor resonances for both the quasi-TE and quasi-TM mode in the same resonator. The cavity consists of the aforementioned 500 nm-wide waveguide and has a rounded square shape with four 18 μm -long straight sections that are longer than the directional coupler (10 μm) to allow to independently design the cavity and directional couplers. The bend radius in the ring resonator (11 μm) is a trade-off between low bend losses and a free spectral range that is large enough for both modes not to limit the dynamic range of the experiments. The gap between the waveguides in both directional couplers (250 nm) keeps a balance between the strong coupling of the quasi-TM mode and the weak coupling of the quasi-TE mode, allowing power transfer of the latter without unacceptable scatter losses of the former. Both modes exhibit clearly visible resonances with over 15 dB extinction ratio (Figure 3.9), proving the concept of exciting both the quasi-TE and quasi-TM mode with two similar directional couplers by using the periodicity of the power transfer.

However, two important drawbacks of this approach also become apparent from the measured transmission spectra (Figure 3.9). First, the resonance full-width at half-maximum of the quasi-TM mode (490 pm) is much larger than that of the quasi-TE mode (130 pm), making the former more noise sensitive. The extra scattering caused by the strong coupling of the quasi-TM mode in the directional couplers, inherent to this approach, is suspected to substantially increase its roundtrip loss and consequently also its resonance width. Second, the fiber-to-fiber insertion loss of the quasi-TM mode is up to 25 dB larger than that of the quasi-TE mode, making it almost impossible to simultaneously interrogate both modes using flood illumination and detector array read-out. The primary reason for the much higher loss for the quasi-TM mode is the impossibility to use adiabatic tapers due to coupling between the fundamental quasi-TM mode and higher order quasi-TE modes when linearly tapering from a

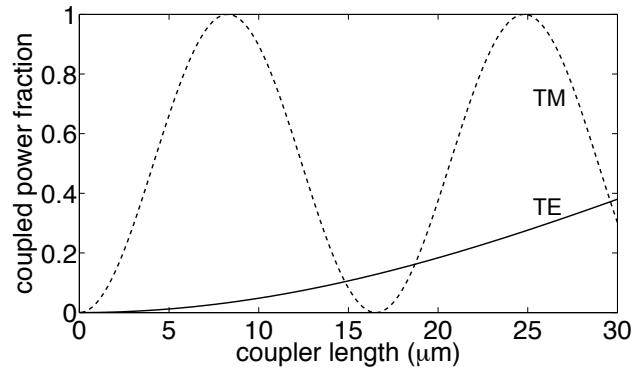


Figure 3.7: The quasi-TM mode is less confined than the quasi-TE mode, and therefore couples much stronger in a directional coupler, resulting in much more power transfer over the same distance. This graph of a simulation of a directional coupler between two 500 nm-wide and 220 nm-high silicon wire waveguides with 250 nm gap illustrates that the periodicity of the power transfer of the strongly coupled quasi-TM mode allows to couple a desired power fraction for both modes. By choosing the appropriate distance between the waveguides and the appropriate coupler length, the required power for both modes can be coupled to the ring resonator.

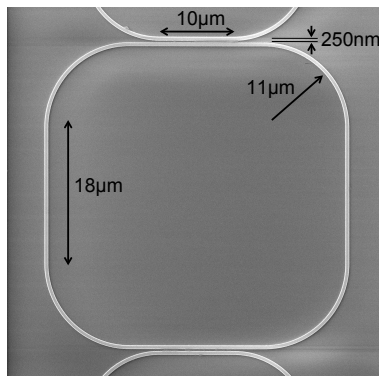


Figure 3.8: This scanning electron micrograph pictures a silicon photonic implementation of the dual polarization ring resonator sensor with two access waveguides. The directional couplers are equal and are shorter than the sides of the rounded square shaped cavity to allow an independent design of the cavity and couplers. They balance between a strong coupling of the quasi-TM mode and a weak coupling of the quasi-TE mode. The cavity roundtrip length is a trade-off between having sharp resonances and a large free spectral range.

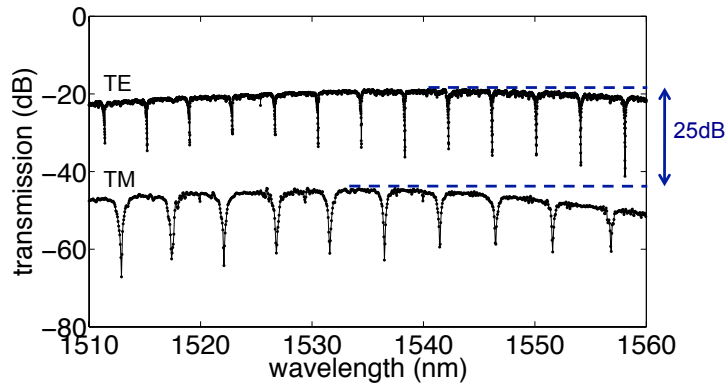


Figure 3.9: The measured fiber-to-fiber transmission spectra of the two access waveguides show the desired large extinction for both modes in the water-clad sensor. However, especially the quasi-TM resonances are too broad (490 pm) for accurate sensing. Moreover, the insertion loss of the quasi-TM mode is 25 dB higher than that of the quasi-TE mode, preventing simultaneous read-out of both modes with a broad laser beam and detector array read-out.

broad waveguide to a narrow waveguide [16]. For the quasi-TE mode, a linear grating first couples light to a $10\ \mu\text{m}$ -wide waveguide, that is then linearly tapered to a low-loss $2\ \mu\text{m}$ -wide waveguide. Only for bends and for coupling to the ring resonator is the waveguide for the quasi-TE mode linearly tapered to a more lossy single-mode $500\ \text{nm}$ -wide photonic wire waveguide. This approach is not applicable to the quasi-TM mode, where a less efficient focusing grating directly couples the light to a photonic wire, that is then used to transport the light across the complete sensor matrix.

The combination of a lower coupling efficiency and higher propagation losses make the quasi-TM mode less suited to interrogate sensors, especially in large sensor matrices for multiplexed sensing. Therefore, next section introduces an implementation of a dual polarization ring resonator sensor that only requires interrogation with the quasi-TE mode.

3.4.2 Implementation with a single access waveguide

An advantageous implementation of a dual polarization ring resonator sensor (Fig. 3.10) follows a design proposed by D. Vermeulen et al. [17] and P. De Heyn et al. [18], and consists of a ring resonator with a single

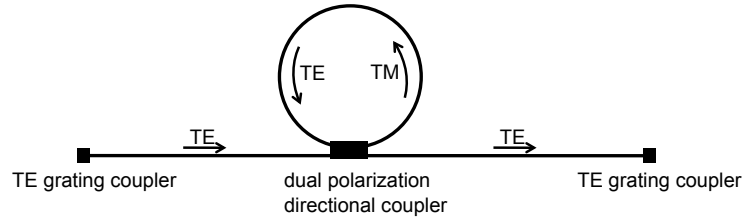


Figure 3.10: The inefficient quasi-TM access waveguide can be avoided by using a dual polarization directional coupler that allows to excite both resonator modes from the low-loss quasi-TE mode of a single access waveguide. When the coupling to each of the modes matches its roundtrip loss, the transmission spectrum will exhibit a superposition of the periodic resonance dips corresponding with the two modes.

access waveguide that guides quasi-TE polarized light to and from the resonator, and that employs a dual polarization directional coupler to couple this quasi-TE mode of the access waveguide to both the quasi-TE and quasi-TM mode of the ring resonator. When the coupling to each of the modes approximately matches its roundtrip loss, the transmission spectrum will exhibit a superposition of the periodic resonance dips that correspond with both resonant modes. The benefits of this approach are threefold. First, the roundtrip losses are reduced by using only one access waveguide. Second, the routing from and to the sensor can be made compact and low-loss by only using the highly confined quasi-TE mode that allows small bend radii and linear tapering. Third, the more efficient grating couplers for the quasi-TE polarization can be used as the only interface with free space modes, improving the transmission and bandwidth.

The dual polarization directional coupler (Figure 3.11) consists of two waveguides with different widths, that are chosen so that the effective refractive index of the quasi-TE mode of the access waveguide is close to that of the quasi-TM mode of the ring waveguide [19, 20]. On one hand, the coupling between the quasi-TE mode of the access waveguide and the quasi-TM mode of the ring waveguide is thus characterized by a high degree of phase matching, but by a small modal overlap due to the different polarization. On the other hand, the coupling between the quasi-TE modes of the access and ring waveguides is characterized by a low degree of phase matching, but by a large modal overlap. Since the power exchange level between two modes increases with modal overlap and the degree of phase matching according to coupled mode theory [21],

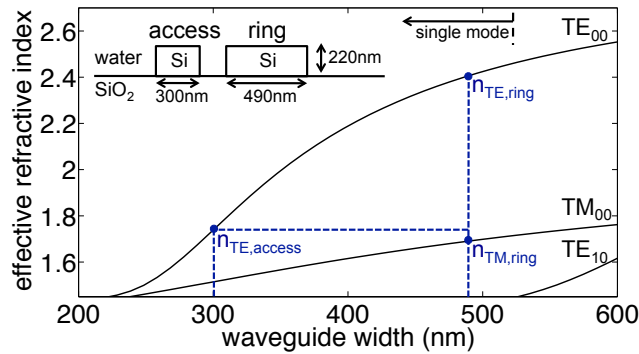


Figure 3.11: The dual polarization directional coupler consists of two waveguides with different widths, that are chosen so that the effective refractive index of the quasi-TE mode of the access waveguide is close to that of the quasi-TM mode of the ring waveguide, thus allowing coupling between the two despite the very different field profiles [19, 20]. The efficiency of the coupling to the quasi-TE mode of the ring waveguide will decrease because of the phase mismatch, but is still possible due to the similar mode profiles.

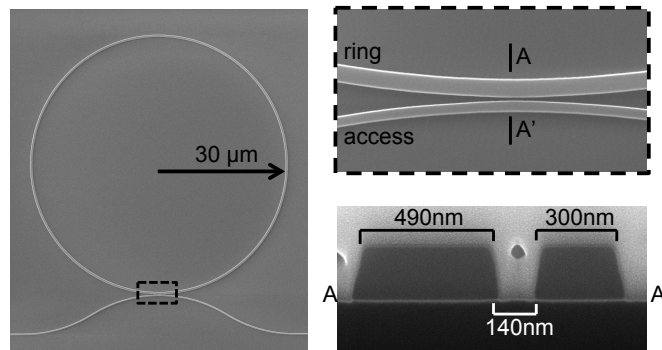


Figure 3.12: This scanning electron micrograph shows a silicon photonic implementation of the dual polarization ring resonator sensor with one access waveguide. A 300 nm-wide access waveguide experimentally proved to couple to both the quasi-TE and quasi-TM waveguide of the 490 nm-wide ring waveguide, and the gap of 140 nm resulted in clearly visible resonances for both (Figure 3.13). The choice for a circular cavity instead of the rounded square one of the implementation with two access waveguides is arbitrary. Also here, the cavity roundtrip length is chosen large to have sharp resonances, while retaining a free spectral range that is large enough for unambiguous sensing.

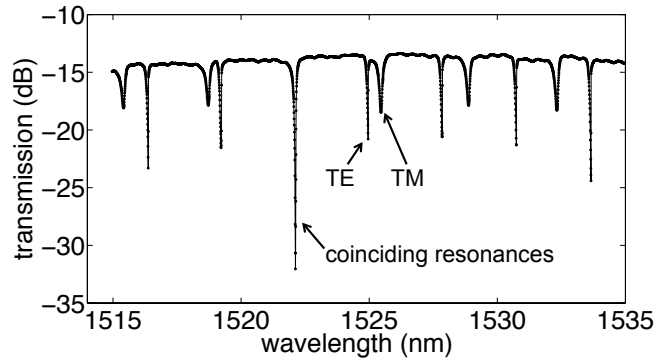


Figure 3.13: The measured fiber-to-fiber transmission spectrum of the water-clad device pictured in Figure 3.12 has clearly visible resonance dips for both the quasi-TE and quasi-TM modes, allowing accurate and independent tracking of both. When two resonances overlap, the extinction increases significantly.

close-to critical coupling can be achieved for both resonant modes by choosing the appropriate waveguide widths and distance between the waveguides.

A silicon photonic implementation (Figure 3.12) confirmed this concept. The resonator waveguide is 490 nm-wide and 220 nm-high, so that it only guides the quasi-TE and quasi-TM modes and has a large birefringence to minimize the coupling between these modes in the bends [14]. A bend radius of $30\ \mu\text{m}$ guarantees low bend losses while retaining a free spectral range that is large enough for sensing with a large dynamic range (3 nm for the quasi-TE mode and 3.5 nm for the quasi-TM mode). The quasi-TE mode of the 300 nm-wide access waveguide is almost phase matched to the quasi-TM mode of the ring waveguide (Figure 3.11) and the waveguides are vertically asymmetrical (water cladding and sloped side-walls) to enable cross-polarization coupling [16]. A 140 pm gap between the waveguides proved to couple enough power to both modes so that both have resonance dips with sufficient extinction (Figure 3.13, $-8\ \text{dB}$ for the quasi-TE mode and $-4\ \text{dB}$ for the quasi-TM mode).

The measured transmission of this sensor (Figure 3.13) confirms the benefits of this implementation over the implementation with two access waveguides. First, the resonances are much sharper (full-width at half-maxima of $70\ \text{pm}$ and $170\ \text{pm}$ for the quasi-TE and quasi-TM mode respectively) because of reduced scattering and coupling losses in the single directional coupler, especially for the quasi-TM mode. Second, the fiber-to-fiber

insertion loss (-13 dB) is much lower, providing enough power budget for parallel interrogation of multiple sensors. Therefore, this implementation is the preferred choice for the proof-of-concept experiment described in the next section.

3.5 Experimental proof-of-concept

Section 3.3 reported calculations indicating that a dual polarization ring resonator sensor consisting of an easy-to-fabricate 500 nm-wide and 220 nm-high silicon waveguide can measure the refractive index and thickness of a biomolecular layer with sufficient accuracy to qualitatively analyze structural molecular changes when integrated in a low-noise measurement platform, while section 3.4.2 proposed an implementation of this sensor with a single access waveguide. This section offers an experimental proof of the concept by showing that the proposed sensor can measure the refractive index and thickness of thin dielectric layers.

Resonance wavelength shifts of the quasi-TE and quasi-TM modes of a dual polarization ring resonator sensor similar to the one pictured in Figure 3.12 were measured as a function of the refractive index and thickness of silicon oxynitride layers of only a few nanometers that were deposited with plasma-enhanced chemical vapor deposition. Four different compositions of silicon oxynitride, each with a different refractive index, were deposited on four nominally identical chips. For each composition, the thickness of the layer was incremented four times, and the resonance wavelengths were measured in between consecutive depositions. During each transmission measurement, the sensor was covered with water to have a refractive index contrast that is representative for the target application. A temperature-stabilized mount limited the temperature variations in between the measurements. The refractive index of each silicon oxynitride composition was measured with a spectroscopic ellipsometer (M-2000FI from J.A. Woollam) on a 100 nm-thick layer deposited with the same parameters as the thinner layers. Extrapolating the measured refractive index, the thickness of the thin layers was subsequently measured with the same ellipsometer on planar thin films that were deposited in the same run as the layers on the sensor. For this proof-of-concept experiment, the measurement errors of the ellipsometer were neglected, as they are dominated by other sources of measurement errors (see later).

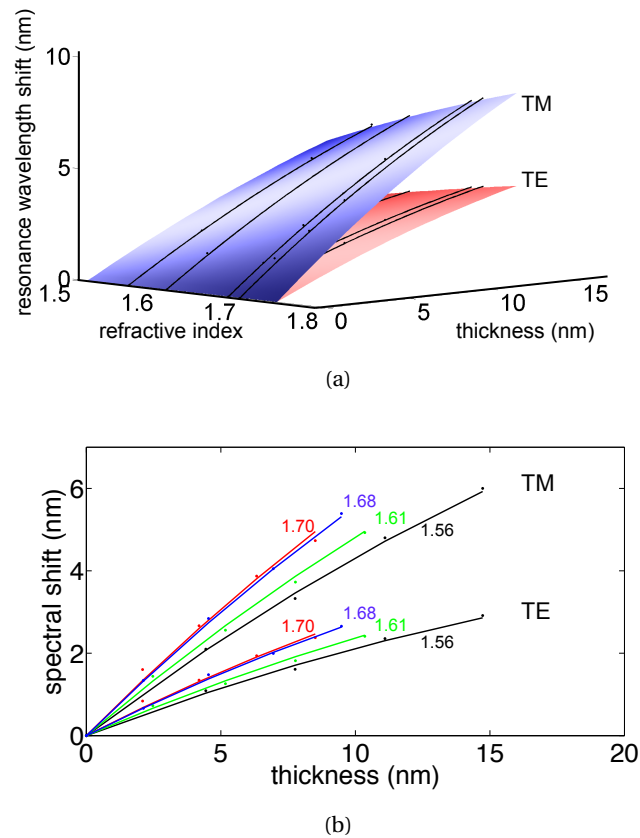


Figure 3.14: (a) The model (equation 3.1) follows the trend of the 16 measured resonance wavelength shifts for both the quasi-TE and quasi-TM modes with a $0.9965 R^2$ goodness-of-fit value, but the measured shifts are noisy. (b) The projection of the measured shifts (dots) and model (lines) on one of the principal planes confirms this.

While the model (equation 3.1) follows the trend of the 16 measured resonance wavelength shifts for each polarization very well (Figure 3.14)) with a high goodness-of-fit value ($R^2 = 0.9965$), the measurement was very noisy, with a standard deviation of the difference between the measured shifts and the model as high as 75 pm and 120 pm for the quasi-TE and quasi-TM modes respectively. Temperature changes in between the measurements, despite the temperature-stabilized mount, are presumably an important noise factor. Note that temperature variations of only 1 K already result in resonance wavelength shifts in the order of 100 pm. Reference ring resonator sensors (section 2.4.3 in chapter 2) can help to compensate this noise in future experiments.

The large resonance wavelength noise translates into a large inaccuracy of the sensor in this particular experiment. Solving the model for the refractive index and thickness with the same measured resonance wavelength shifts as the once used for calibration (best case situation), results in a standard deviation of 0.2 RIU and 1.4 nm on the difference between the refractive index and thickness values measured with the ellipsometer and our ring sensor respectively. Although this experiment is insufficient to experimentally prove the applicability of the sensor to measure structural changes in a biolayer, it does show that our dual polarization ring resonator sensor can differentiate between the refractive index and thickness of thin layers. The inaccuracy is caused by the noisy measurement method, and is not inherent to the sensor, as resonance wavelength noise as low as 220 fm has been reported for the quasi-TE resonances of a similar sensor [15]. Future work should focus on performing low noise experiments, preferably in real-time and in a single buffer.

3.6 Conclusions

The fundamental quasi-TE and quasi-TM modes can simultaneously be excited in an easy-to-fabricate silicon ring resonator sensor by the low-loss quasi-TE mode of a single access waveguide that is narrowed in the directional coupler. The proposed dual polarization sensor can distinguish between the refractive index and thickness of thin dielectric layers, and has the prospect of being able to do so with sufficient accuracy to measure structural molecular changes. Silicon photonic dual polarization ring resonator sensors thus offer a highly multiplexed platform to study biomolecular interactions in more depth than with single-mode sensors.

References

- [1] S E Radford. *Protein folding: progress made and promises ahead*. Trends Biochem Sci, 25(12):611–8, Dec 2000.
- [2] www.farfield-group.com.
- [3] Juan Wang, Xiaowen Xu, Zhanxia Zhang, Fan Yang, and Xiurong Yang. *Real-Time Study of Genomic DNA Structural Changes upon Interaction with Small Molecules Using Dual-Polarization Interferometry*. Analytical Chemistry, 81(12):4914–4921, 2009.
- [4] Maryline Fresquet, Thomas A. Jowitt, Joni Yloestalo, Paul Coffey, Roger S. Meadows, Leena Ala-Kokko, David J. Thornton, and Michael D. Briggs. *Structural and functional characterization of recombinant matrilin-3 A-domain and implications for human genetic bone diseases*. Journal of Biological chemistry, 282(48):34634–34643, November 2007.
- [5] Katrien De Vos. *Label-free Silicon Photonics Biosensor Platform with Microring Resonators*. PhD thesis, Universiteit Gent, 2010.
- [6] B. Lillis, M. Manning, H. Berney, E. Hurley, A. Mathewson, and M.M. Sheehan. *Dual polarisation interferometry characterisation of DNA immobilisation and hybridisation detection on a silanised support*. Biosensors and Bioelectronics, 21(8):1459 – 1467, 2006.
- [7] J. Voros. *The density and refractive index of adsorbing protein layers*. Biophysical Journal, 87(1):553–561, JUL 2004.
- [8] KA Peterlinz, RM Georgiadis, TM Herne, and MJ Tarlov. *Observation of hybridization and dehybridization of thiol-tethered DNA using two-color surface plasmon resonance spectroscopy*. Journal of the American Chemical Society, 119(14):3401–3402, April 1997.
- [9] AW Peterson, LK Wolf, and RM Georgiadis. *Hybridization of mismatched or partially matched DNA at surfaces*. Journal of the American Chemical Society, 124(49):14601–14607, December 2002.
- [10] J Wen and T Arakawa. *Refractive index of proteins in aqueous sodium chloride*. Analytical Biochemistry, 280(2):327–329, May 2000.
- [11] F Hook, J Voros, M Rodahl, R Kurrat, P Boni, JJ Ramsden, M Textor, ND Spencer, P Tengvall, J Gold, and B Kasemo. *A comparative study of protein adsorption on titanium oxide surfaces using in situ ellipsom-*

- etry, optical waveguide lightmode spectroscopy, and quartz crystal microbalance/dissipation.* Colloids and Surfaces B-Biointerfaces, 24(2):155–170, March 2002.
- [12] J Tsai, R Taylor, C Chothia, and M Gerstein. *The packing density in proteins: standard radii and volumes.* J Mol Biol, 290(1):253–66, Jul 1999.
- [13] Marcus Swann, Neville Freeman, Simon Carrington, Gerry Roman, and Paul Barrett. *Quantifying structural changes and stoichiometry of protein interactions using size and density profiling.* Letters in Peptide Science, 10:487–494, 2003.
- [14] F Morichetti, A Melloni, and M Martinelli. *Effects of polarization rotation in optical ring-resonator-based devices.* Journal of Lightwave Technology, 24(1):573–585, January 2006.
- [15] Muzammil Iqbal, Martin A. Gleeson, Bradley Spaugh, Frank Tybor, William G. Gunn, Michael Hochberg, Tom Baehr-Jones, Ryan C. Bailey, and L. Cary Gunn. *Label-Free Biosensor Arrays Based on Silicon Ring Resonators and High-Speed Optical Scanning Instrumentation.* IEEE J. Sel. Topics Quantum Electron., 16(3):654–661, May-June 2010.
- [16] D Vermeulen, K Van Acoleyen, S Ghosh, S Selvaraja, W A D De Cort, N A Yebo, E Hallynck, K De Vos, P P P Debackere, P Dumon, W Bogaerts, G Roelkens, D Van Thourhout, and R Baets. *Efficient Tapering to the Fundamental Quasi-TM Mode in Asymmetrical Waveguides.* In European Conference on Integrated Optics, 2010.
- [17] D. Vermeulen, P. De Heyn, T. Van Vaerenbergh, W Bogaerts, and G. Roelkens. *Silicon-on-Insulator polarization rotating micro-ring resonator.* In IEEE Photonics Conference, 2011.
- [18] P. De Heyn, D. Vermeulen, D. Van Thourhout, and G. Roelkens. *Silicon-on-insulator all-pass microring resonator using a polarization rotating coupling section.* to be published in IEEE Photonics Technology Letters, 2012.
- [19] Liu Liu, Yunhong Ding, Kresten Yvind, and Jorn M. Hvam. *Efficient and compact TE-TM polarization converter built on silicon-on-insulator platform with a simple fabrication process.* Optics Letters, 36(7):1059–1061, April 2011.

- [20] Liu Liu, Yunhong Ding, Kresten Yvind, and Jorn M. Hvam. *Silicon-on-insulator polarization splitting and rotating device for polarization diversity circuits*. *Optics Express*, 19(13):12646–12651, June 2011.
- [21] A. Yariv. *Coupled-Mode Theory For Guided-Wave Optics*. *IEEE Journal of Quantum Electronics*, QE 9(9):919–933, 1973.

4

Slot waveguide ring resonator sensor

A ring resonator sensor can quickly and accurately measure the analyte concentration through the initial slope of the binding curve with a limit of detection down to the femtomolar range (section 2.4 in chapter 2). At the beginning of this PhD-research, it was an active topic of research whether the sensor's limit of detection could further benefit from an enhanced light-matter interaction and corresponding enhanced sensitivity to refractive index changes. A promising concept was that of a ring resonator sensor comprised of a slot waveguide, a waveguide with a narrow low-refractive-index region in between two high-refractive-index strips which is known to enhance the transverse-electric (TE) polarized field in the vertical low-refractive-index slot [1, 2]. As opposed to resonant confinement schemes, such as photonic crystal waveguides, the confinement in the low-index region is broadband. C. A. Barrios et al. [3, 4] proved that a slot waveguide ring resonator in Si_3N_4 on SiO_2 with $140\ \mu\text{m} \times 140\ \mu\text{m}$ footprint and a 200 nm wide slot region indeed enhances the sensitivity compared to a normal strip waveguide. Later, this sensor was further optimized [5], and integrated in a compact cartridge for label-free multiplexed sensing [6]. However, it remained unclear whether the slot waveguide effectively improved the limit of detection of the ring resonator sensor.

Moreover, this sensor was made with electron beam lithography, a high resolution fabrication tool that is not suited for mass fabrication, and at that time it was unclear whether the concept was also applicable to more compact silicon-on-insulator sensors fabricated with mass-fabrication-compatible optical lithography and dry etching.

Therefore, we theoretically and experimentally studied the sensitivity enhancement with a silicon slot waveguide ring resonator that can be fabricated with this method. We also looked into its impact on other parameters that are relevant for biosensing, and estimated the limit of detection attainable with this sensor.

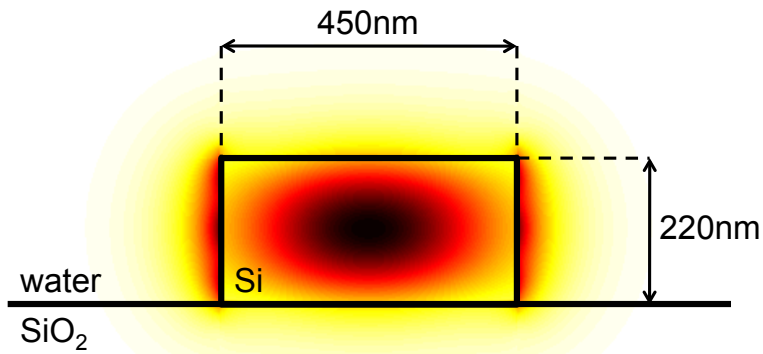
After section 4.1 describes the working principle of sensitivity enhancement in a slot waveguide, section 4.2 presents an optimized slot waveguide for biosensing that can still be manufactured with mass fabrication compatible optical lithography and dry etching. Subsequently, section 4.3 discusses the fabrication of slot waveguides and sections 4.4 and 4.5 present the experimental verification of the sensitivity enhancement in a silicon slot waveguide ring resonator sensor, both for refractive index changes of the complete liquid as for protein binding at its surface. Section 4.6 finalizes with a comparison of the limit of detection of a slot waveguide ring resonator sensor with that of a wire waveguide ring resonator sensor.

4.1 Working principle

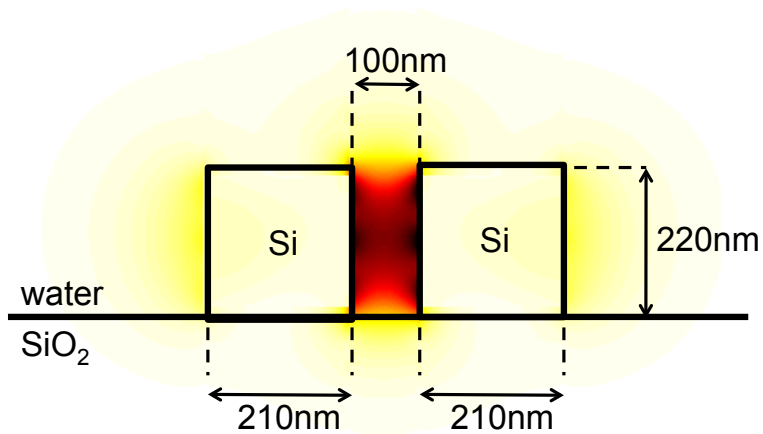
The limit of detection of a ring resonator sensor, the smallest concentration it can reliably detect, is inversely proportional to the sensitivity of its resonance wavelengths to refractive index changes at its surface (section 2.4 in chapter 2), which depends heavily on the electric field energy density there (section 2.3.2 in chapter 2):

$$\Delta\lambda(x, y) \propto \frac{\lambda \cdot |\vec{E}(x, y)|^2}{\iint_{-\infty}^{\infty} n^2(x, y) \cdot |\vec{E}(x, y)|^2 dx dy} \quad (4.1)$$

with $\Delta\lambda(x, y)$ the resonance wavelength shift caused by a molecule binding at location (x, y) at the waveguide surface, $|\vec{E}(x, y)|^2$ the electric field energy density there at wavelength λ , and $n(x, y)$ the refractive index profile of the waveguide.



(a) Electric field energy density profile of a wire waveguide



(b) Electric field energy density profile of a slot waveguide

Figure 4.1: The electric field energy density of the quasi-TE mode of a silicon waveguide in water is significantly enhanced close to vertical sidewalls due to the boundary conditions at a dielectric interface and the large refractive index contrast between water and silicon. A slot waveguide has a narrow slot in between two high-index strips, and hence has two extra vertical sidewalls close to the high-intensity center of its quasi-TE mode that cause a large enhancement of the field inside the slot. This results in a larger sensitivity to molecular interactions at the slot walls.

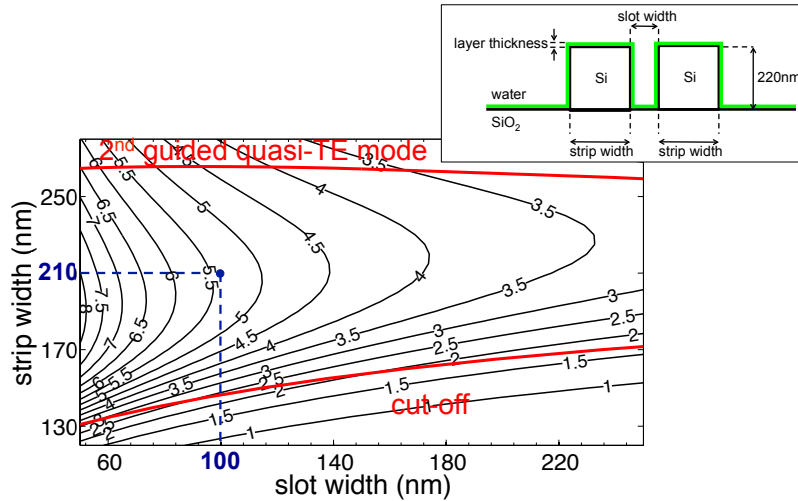


Figure 4.2: The simulated resonance wavelength shift (nm) of a silicon slot waveguide ring resonator sensor for saturation of its surface with proteins increases with decreasing slot width. The best slot waveguide that can still be fabricated with our mass fabrication compatible method (section 2.1.1) has a 100 nm-wide slot and 210 nm-wide silicon strips, and is six times more sensitive to molecular interactions than a normal silicon ring resonator sensor.

Since the normal component of the electric displacement field must be continuous at a dielectric interface, the normal component of the electric field at the cladding-side of the core-cladding interface of a waveguide is enhanced with a factor $n_{core}^2/n_{cladding}^2$ compared to its value at the core-side. For the high-index-contrast interface between silicon ($n_{core} = 3.47$) and water ($n_{cladding} = 1.31$) in our sensors, this corresponds with a sevenfold enhancement of the electric field component normal to the waveguide surface. As the quasi-TE mode of a waveguide has its major electric field component normal to the waveguide sidewalls, the major field discontinuity occurs there. This effect already happens to some extent for the quasi-TE mode of a wire waveguide, which has a significant electric field energy density enhancement at its sidewalls compared to its top surface (Figure 4.1(a)). The effect is however much larger for a slot waveguide, with two extra vertical sidewalls close to the high-intensity center of the mode that are moreover placed in each other's evanescent field (Figure 4.1(b)). Molecules that bind to receptors placed at these inner sidewalls will induce a large phase shift in the mode, and will therefore result in a large resonance wavelength shift of the ring resonator.

4.2 Design of a silicon slot waveguide for sensing

Taking into account the fixed 220 nm waveguide height of our fabrication process (section 2.1.1 of chapter 2), the impact of the slot and strip width of a silicon slot waveguide on the sensitivity of a ring resonator sensor is studied (Figure 4.2). First, the film mode matching tool *Fimmwave* [7] was used to simulate the effective refractive index change induced by 5 nm thickness increase of a layer with refractive index 1.45 uniformly covering the waveguide, which models saturation of the waveguide surface with proteins [8, 9]. Then, the corresponding resonance wavelength shift was calculated using (appendix C):

$$\Delta\lambda = \frac{\lambda \cdot \Delta n_{eff}}{n_g}$$

with λ the wavelength in vacuum, Δn_{eff} the change of the effective refractive index, and n_g the group refractive index, which was also simulated with *Fimmwave*. This resonance wavelength shift is a measure for the sensitivity of a ring resonator comprised of the corresponding waveguide, averaged over its surface.

In the relevant range of the parameters, the sensitivity increases with decreasing slot width. Since a slot width down to 100 nm is feasible with our technology (section 4.3), Figure 4.2 shows that the optimal silicon strip width is 210 nm, which corresponds with a 5.4 nm resonance wavelength shift at saturation of the biosensor. This is a sixfold enhancement compared to a ring resonator comprised of a 450 nm-wide silicon wire waveguide.

However, also some drawbacks can be identified.

First, whereas a slot waveguide enhances the signal of molecular interactions at its surface with a factor 6, it also increases the impact of noisy refractive index changes in the bulk of the fluidic sample with a factor 4, lowering the benefit for the signal-to-noise ratio (the surface-to-volume sensitivity ratio) to only a factor 1.5. Reference sensors help to compensate refractive index noise (section 2.4.3 in chapter 2), but might fail to do so sufficiently in the case of noise sensitive slot waveguides.

Second, the sensitivity of a slot waveguide depends heavily on the location of molecular binding on the waveguide surface. Whereas a silicon wire waveguide is already four times more sensitive at the center of its sidewalls than at two locations at its top side (section 2.3.1 in chapter 2), there is

a 32-fold (15 dB) different impact between molecules binding in the slot region and at the top side of our optimal slot waveguide (Figure 4.3). This huge non-uniformity can hinder the interpretation of measurements, especially at low concentrations, since molecules can preferentially bind to more accessible parts of the waveguide.

Third, loss influences the performance of a ring resonator sensor through its resonance width (section 2.1.2 in chapter 2), and is much higher in a slot waveguide than in a wire waveguide. A vast fraction of the mode travels through water, which absorbs light at the wavelength of $1.55\ \mu\text{m}$ with an absorption coefficient as high as $10.9\ \text{cm}^{-1}$ [11]. This results in a simulated contribution of $37\ \text{dB/cm}$ to the propagation loss of our slot waveguide, almost 800 times more than for a $450\ \text{nm}$ -wide wire waveguide. Additionally, scattering at the roughly etched slot walls will also contribute significantly, although this is more difficult to predict. C. Koos et al. [12] measured $12\ \text{dB/cm}$ propagation loss for a slot waveguide fabricated with the same optical lithography process as ours (section 4.3) and covered with silicon oxide. This is a bottom limit for the scatter loss in our water-covered waveguide, since the refractive index contrast between silicon and silicon oxide is lower and since the waveguide measured by C. Koos et al. has a broader slot region ($157\ \text{nm}$). Finally, the lower confinement in slot waveguides will also increase the radiation loss in bends, forcing large bend radii in the design of ring resonator sensors. Only for bend radii larger than $11\ \mu\text{m}$, is the radiation loss smaller than the expected combined absorption and scatter loss in our slot waveguide (Figure 4.4), as indicated by the calculated radiation loss in three dimensions with the finite-difference time-domain method using the software package *Meep* [10]. The roundtrip loss is expected to be minimal for a circular cavity with $16\ \mu\text{m}$ bend radius.

4.3 Fabrication of silicon slot waveguides

The sensitivity enhancement of silicon slot waveguide ring resonator sensors increases with decreasing slot width (section 4.2), making it worth considering fabrication methods with a higher resolution than optical lithography. A first alternative, electron beam lithography and dry etching, is popular for allowing fabricating low-loss slot waveguides with slot widths down to only tens of nanometers [2, 13]. However, it is a serial technique that is not suited for high-volume fabrication of disposable sensor chips. A second alternative, focused-ion-beam etching, is a technique

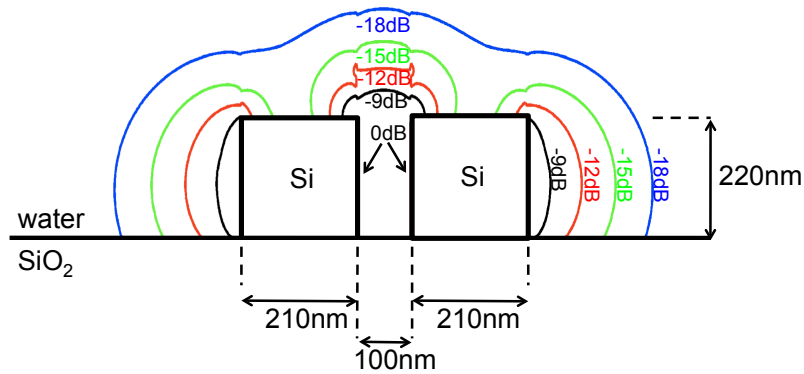


Figure 4.3: The evanescent electric field energy density of the selected silicon slot waveguide varies considerably over the waveguide surface, with a 32-fold (15 dB) contrast between the centers of the slot walls and the top side of the silicon strips. Since molecules can preferentially bind to more accessible parts of the waveguide, this can obstruct the interpretation of results, especially at low analyte concentrations.

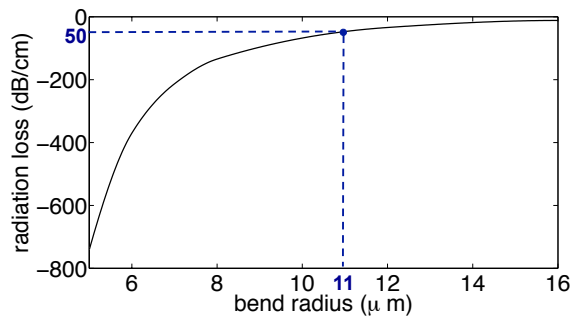


Figure 4.4: A three-dimensional finite-difference time-domain simulation with the software package *Meep* [10] confirms that the radiation loss in water-covered slot waveguide bends is much higher than in wire bends due to the lower mode confinement. Only for bend radii larger than $11 \mu\text{m}$ the radiation loss stops dominating the expected absorption and scatter loss.

that can directly mill slots in silicon waveguides without needing resist or dry etching. It therefore allows medium volume fabrication of slots in structures that are prefabricated in high-volume with optical lithography and dry etching. We tested this method and contributed to making 90 nm-wide slots in existing silicon waveguides [14] using focused-ion-beam etching with iodine enhancement and an alumina hard mask to protect the waveguide against crystal damage and implantation of impurities [15, 16]. The high loss of the resulting waveguides (100 dB/cm) and moderate throughput of the technique however indicated that also this method is not a good alternative to fabricate high-quality disposable sensor chips.

Hence, the structures presented in this chapter are made by mass fabrication compatible 193 nm optical lithography and dry etching via *ePIX-fab* [17], using the method detailed by S. Selvaraja et al. [18, 19]. Slot widths down to 100 nm appeared to be feasible with the standard process by defining 120 nm-wide slots on the mask and decreasing the illumination dose.

4.4 A silicon slot waveguide ring resonator sensor

The slot waveguide ring resonator sensor we designed and fabricated with optical lithography (Figure 4.5) has a circular cavity with a bend radius (14 μm) that is large enough to avoid domination of radiation loss over the other expected loss contributions. Its waveguide has a 105 nm-wide slot and 235 nm-wide silicon strips, which is close to the optimal parameters feasible with our fabrication process (Figure 4.2). Its directional coupler consists of two slot waveguides to match the phase and increase the coupling strength, and a small gap of 180 nm between the waveguides appeared to critically couple the quasi-TE mode of the access waveguide to that of the ring. An adiabatic mode convertor [20] adapts the quasi-TE mode of the slotted access waveguide to that of a wire to efficiently connect the sensor to on-chip grating couplers.

The transmission spectrum of the slot waveguide ring resonator sensor in water (Figure 4.6) exhibits deep resonance dips with 9.9 nm free spectral range and 2.9 nm full-width at half-maximum. The latter corresponds with an average propagation loss as high as 223 dB/cm (via equation (2.6) for critical coupling), much higher than the combination of the expected absorption loss (37 dB/cm), scatter loss at surface roughness (12 dB/cm)

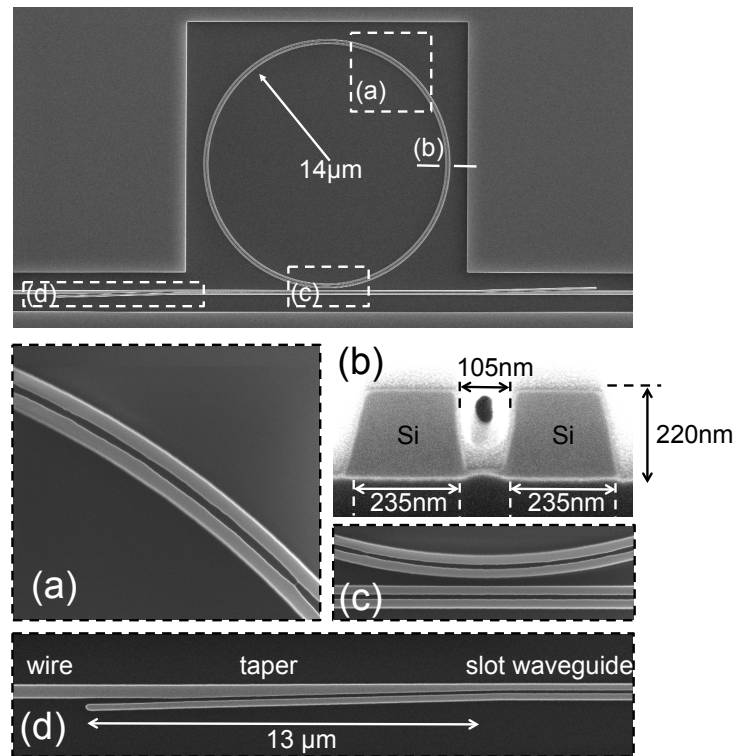


Figure 4.5: Our silicon slot waveguide ring resonator sensor has a circular cavity with a large bend radius ($14\ \mu\text{m}$) to avoid domination of radiation loss over the other expected loss contributions, and was fabricated with optical lithography and reactive ion etching. (a,b) The resonator consists of a close-to optimal waveguide with a 105 nm-wide slot and 235 nm-wide silicon strips, which is at the edge of what is feasible with our standard process, resulting in a rough slot region. (c) Its directional coupler consists of two slot waveguides to match the phase and increase the couple strength, with a small gap (180 nm) to critically couple the quasi-TE mode of the access waveguide to that of the ring. (d) An adiabatic mode converter [20] adapts the quasi-TE mode of the efficient wire access waveguides to that of the slot access waveguide.

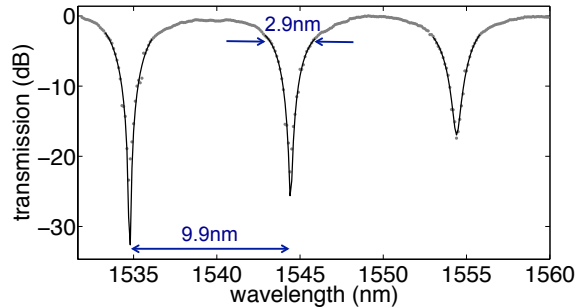


Figure 4.6: The transmission spectrum of the slot waveguide ring resonator sensor in water exhibits deep resonance dips with 9.9 nm free spectral range and 2.9 nm full-width at half-maximum. The extinction decreases with increasing wavelength, probably due a decrease of the confinement and gradual over-coupling.

and radiation loss in bends (18 dB/cm) as predicted in section 4.2. A first possible cause for the extra loss is coupling between the slot waveguide and the slab waveguide surrounding the ring resonator, only separated by a $2\ \mu\text{m}$ trench. A second possible reason is scattering in the directional coupler due to the small gap. While both issues have a straightforward solution, this research was discontinued due to reasons detailed in the next sections.

4.5 Experimental sensitivity enhancement

This experiment was performed in collaboration with dr. Jordi Girones Molera and prof. dr. Etienne Schacht from the Polymer Chemistry and Biomaterials Research Group of the Department of Organic Chemistry of Ghent University.

To verify the slot waveguide sensor's sensitivity enhancement to molecular interactions, its surface was silanized with 3-glycidyloxypropyltrimethoxysilane (GOPTS) following the procedure published by K. De Vos et al. [22], and biotin receptor molecules were immobilized by immersing the GOPTS treated chips overnight in a 0.2 mg/ml solution of 5-(biotinamido)-pentylamine in phosphate buffered saline (pH 9.0). Then the sensor's resonance wavelength shift was monitored continuously while saturating its surface with avidin, a protein with a large affinity to

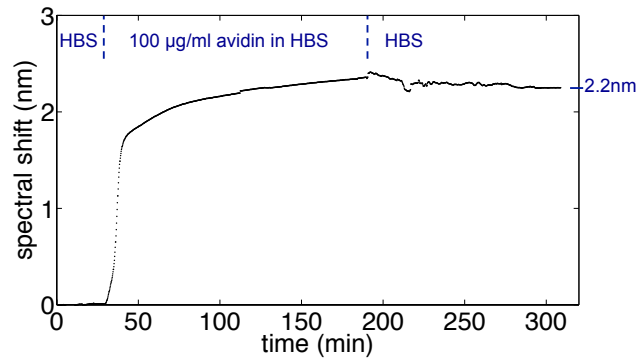


Figure 4.7: The slot waveguide sensor's resonance wavelengths permanently shift 2.2 nm after saturating its surface with avidin-molecules, which is 3.5 times more than the maximum resonance wavelength shift of a normal silicon ring resonator sensor when saturated with avidin (625 pm [21]). While this also confirms the sensitivity enhancement to biomolecular interactions, it is only half of the expected improvement. Together with the large variability between multiple experiments, this indicates possible issues with mass transport inside the narrow slot region.

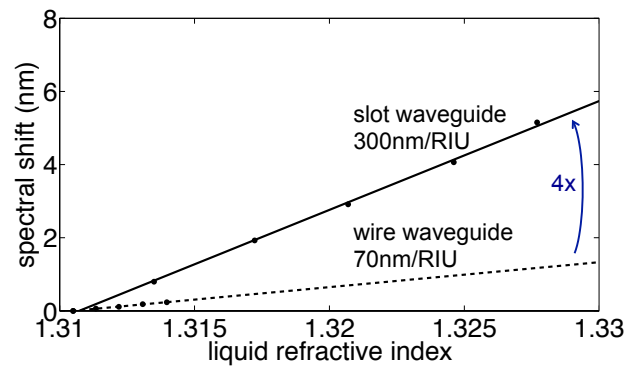


Figure 4.8: The experimental sensitivity to refractive index changes of aqueous solutions is four times larger for our slot waveguide ring resonator sensor than for a normal wire ring resonator sensor [21], proving the expected sensitivity increase to refractive index noise in the bulk of the liquid sample.

biotin, by switching a liquid flow over the sensor from HEPES-buffered saline (HBS) with pH 7.5 to a very high concentration of 100 $\mu\text{g/ml}$ avidin in HBS. After 1.7ml of the avidin solution was flown over the ring resonator, HBS without avidin was again flown over the sensor to rinse its surface, revealing a permanent resonance wavelength shift of 2.2 nm (Figure 4.7). While this is 3.5 times more than the maximum resonance wavelength shift of a normal silicon ring resonator sensor when saturated with avidin (625 pm [21]), it is only half of the enhancement predicted by *Fimmwave* simulations (section 4.2). Moreover, we found large variations of the experimental enhancement between different experiments, which might indicate hindered biochemical surface modification and mass transport in the narrow slot region.

To additionally verify the slot waveguide ring resonator sensor's increased sensitivity to refractive index noise, watery solutions with different NaCl-concentrations were flown over the sensor in a closed channel and the corresponding refractive index was calculated [23]. It was found that indeed the slot waveguide ring resonator sensor is four times more sensitive (300 nm/RIU) to bulk refractive index changes in its aqueous environment than a wire sensor (70 nm/RIU [21]).

4.6 Limit of detection

Slot waveguide ring resonator sensors enhance the sensitivity compared to wire ring resonator sensors, as predicted in sections 4.1 and 4.2, and experimentally confirmed in section 4.5. However, end-users of the platform value the limit of detection (LOD) of the sensor much more than its optical sensitivity enhancement. The limit of detection can be approximated by (section 2.4.1 in chapter 2):

$$LOD \approx 3.29 \cdot 2\sqrt{3} \cdot \frac{\sqrt{2} \cdot \sigma_{\Delta\lambda}}{\sqrt{R_t} \cdot T^{\frac{3}{2}} \cdot S_{slope}} \quad (4.2)$$

with $\sigma_{\Delta\lambda}$ the standard deviation of the Gaussian noise on the binding curve, R_t the temporal resolution of the binding curve, T the measurement time, and S_{slope} the slope sensitivity. The factor $\sqrt{2}$ in the numerator accounts for taking the difference between the signal of a biosensor with receptor molecules and a reference sensor without receptor molecules.

The ratio between the limits of detection of a slot waveguide ring resonator

sensor and that of a wire ring resonator sensor is

$$\frac{LOD_{wire}}{LOD_{slot}} = \frac{S_{slope,slot}}{S_{slope,wire}} \cdot \frac{\sqrt{R_{t,slot}}}{\sqrt{R_{t,wire}}} \cdot \frac{\sigma_{\Delta\lambda,wire}}{\sigma_{\Delta\lambda,slot}} \quad (4.3)$$

The first factor, the ratio of the slope sensitivities, can theoretically reach a value of 6 (section 4.2), but experimentally only a factor 3.5 has been measured (section 4.5).

The sensor interrogation speed determines the second factor, the ratio of the square roots of the temporal resolution of the respective binding curves. Parallel interrogation of a large amount of sensors is preferably done by scanning the wavelength of a laser source, distributing its power over multiple sensors and measuring their transmission with a detector array (section 2.8 in chapter 2). In that case the temporal resolution depends on the wavelength scan speed and on the scan range, which corresponds to the ring resonator's free spectral range. The free spectral range of a wire ring resonator can be as small as 100 pm for a long folded cavity, and is best measured with a small wavelength step of 1 pm. Even for a slot waveguide ring resonator with very large bend radius that only suffers from absorption loss (37 dB/cm) and scatter loss at surface roughness (12 dB/cm), only free spectral range values that are ten times larger than that of a wire resonator are feasible with sufficient visibility of the resonances, since the slot waveguide ring resonances are ten times broader. To maintain the same temporal resolution for both sensors, the wavelength step when interrogating a slot waveguide can best be chosen 10 pm instead of 1 pm, which roughly results in the same number of measurement points per resonance dip as for a normal ring resonator sensor. The laser can in that case scan ten times faster for the same line rate of the detector array. Under these conditions the second factor in equation (4.3) is approximately one.

The third factor in equation (4.3), the ratio of the noise amplitudes of the binding curves, depends heavily on the noise compensation by the reference sensor (section 2.4.3 of chapter 2):

In a first scenario, differential refractive index variations between the biosensor with receptor molecules and the reference sensor without receptor molecules dominates the noise on their binding curve. Since slot waveguides are less confined than wires, they are more susceptible to refractive index variations in the sample solutions that happen further from the sensor surface. Hence, they are more likely to operate in this scenario. In that case the noise is enhanced together with the signal, so

that the third factor in equation (4.3) is approximately the inverse of the sensitivity enhancement of the slot waveguide, annihilating its benefit. Thus in noisy conditions slot waveguide ring resonator sensors do not significantly improve the limit of detection compared to wire ring resonator sensors. Note however that they are less temperature sensitive due to their lower confinement, since the thermo-optic coefficient of water ($-8 \cdot 10^{-5} / \text{K}$ [24]) at one hand, and that of silicon ($+1.87 \cdot 10^{-4} / \text{K}$ [25]) and silicon dioxide ($+1 \cdot 10^{-5} / \text{K}$) at the other hand have an opposite sign.

In a second scenario, the reference sensor compensates the refractive index variations in the sample liquid sufficiently to make the noise on the resonance wavelength extraction from the transmission spectra dominant on the binding curve noise. Then the large propagation loss in slot waveguides (minimally 49 dB/cm in water) is a drawback. The same Monte-Carlo method as described in section 2.4.4 of chapter 2 predicts that in this case the noise is an order of magnitude larger for slot waveguide ring resonator sensors than for wire ring resonator sensors (Figure 4.9(a)), because of the broader resonances and larger wavelength step (10 pm instead of 1 pm to obtain the same temporal resolution). Again, this annihilates the sensitivity enhancement. The ratio of the limit of detection of a slot waveguide sensor in ideal circumstances (only Gaussian noise on the transmission spectra, and minimal loss of 49 dB/cm) to the minimal limit of detection of a wire sensor (0.9 fM of avidin, section 2.4.4 in chapter 2) is not in the benefit of the slot waveguide sensor (Figure 4.9(b)). Its best limit of detection occurs for a 1.35 mm-long cavity.

4.7 Conclusions

A silicon slot waveguide manufacturable in high volume with accessible optical lithography and dry etching [17–19] can enhance the sensitivity of a ring resonator biosensor up to sixfold compared to a wire ring resonator sensor. However, experiments showed only half of the expected enhancement and were less reproducible than similar experiments on wire ring resonator sensors. This indicates troubled biochemical surface modification and interactions in the less accessible slot, which limits its applicability. Additionally, the increased sensitivity to refractive index variations in the sample solution and increased optical loss annihilate the benefit of the sensitivity enhancement for the sensor's limit of detection, a more important specification than the resonance wavelength sensitivity. Since both drawbacks are to a large extent inherent to slot waveguides,

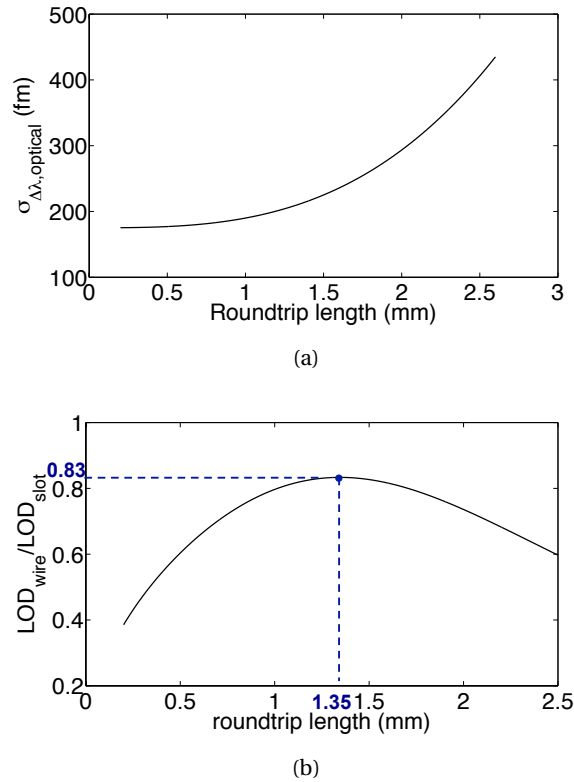


Figure 4.9: (a) Monte-Carlo simulations with the method described in section 2.4.4 of chapter 2 allow to estimate the standard deviation on the resonance wavelength extraction. For a constant propagation loss of 49 dB/cm, a constant extinction ratio of 15 dB and 10 pm wavelength step, the resonance width quickly increases with the roundtrip length, resulting in a monotonous deterioration of the fitting accuracy with increasing roundtrip length. The fitting accuracy is an order of magnitude worse than for a low-loss wire ring resonator sensor. (b) The limit of detection of our slot waveguide ring resonator sensor in ideal circumstances never surpasses that of the optimal wire ring resonator sensor (0.9 fM avidin, see section 2.4.4), despite the sixfold sensitivity enhancement and ten times faster laser scan speed.

little room is left for improvements. Together with the more challenging surface modification, this makes us conclude that silicon wire ring resonator sensors are preferred over silicon slot waveguide ring resonator sensors.

References

- [1] VR Almeida, QF Xu, CA Barrios, and M Lipson. *Guiding and confining light in void nanostructure*. Optics Letters, 29(11):1209–1211, JUN 1 2004.
- [2] Q. F. Xu, V. R. Almeida, R. R. Panepucci, and M. Lipson. *Experimental demonstration of guiding and confining light in nanometer-size low-refractive-index material*. optics letters, 29(14):1626–1628, JUL 15 2004.
- [3] Carlos A. Barrios, Kristinn B. Gylfason, Benito Sánchez, Amadeu Griol, H. Sohlström, M. Holgado, and R. Casquel. *Slot-waveguide biochemical sensor*. Opt. Lett., 32(21):3080–3082, 2007.
- [4] Carlos A. Barrios, Maria Jose Banuls, Victoria Gonzalez-Pedro, Kristinn B. Gylfason, Benito Sanchez, Amadeu Griol, A. Maquieira, H. Sohlstrom, M. Holgado, and R. Casquel. *Label-free optical biosensing with slot-waveguides*. Optics Letters, 33(7):708–710, APR 1 2008.
- [5] Kristinn B. Gylfason, Carl F. Carlborg, Andrzej Kazmierczak, Fabian Dortu, Hans Sohlström, Laurent Vivien, Carlos A. Barrios, Wouter van der Wijngaart, and Göran Stemme. *On-chip temperature compensation in an integrated slot-waveguide ringresonator refractive index sensor array*. Opt. Express, 18(4):3226–3237, 2010.
- [6] C F Carlborg, K B Gylfason, A Kaźmierczak, F Dortu, M J Bañuls Polo, A Maquieira Catala, G M Kresbach, H Sohlström, T Moh, L Vivien, J Popplewell, G Ronan, C A Barrios, G Stemme, and W Van der Wijngaart. *A packaged optical slot-waveguide ring resonator sensor array for multiplex label-free assays in labs-on-chips*. Lab on a Chip, 10(3):281–90, Feb 2010.
- [7] A. Sv Sudbo. *Film mode matching: a versatile numerical method for vector mode field calculations in dielectric waveguides*. Pure and Applied Optics, 2(3):211–33, May 1993.
- [8] J. Voros. *The density and refractive index of adsorbing protein layers*. Biophysical Journal, 87(1):553–561, JUL 2004.
- [9] S Rauf, DJ Zhou, C Abell, D Klenerman, and DJ Kang. *Building three-dimensional nanostructures with active enzymes by surface templated layer-by-layer assembly*. Chemical Communications, (16):1721–1723, 2006.

- [10] Ardavan Farjadpour, David Roundy, Alejandro Rodriguez, Mihai Ibanescu, Peter Bermel, J. D. Joannopoulos, Steven G. Johnson, and Geoffrey Burr. *Improving accuracy by subpixel smoothing in FDTD*. Optics Letters, 31:2972–2974, October 2006.
- [11] KF PALMER and D WILLIAMS. *Optical-properties of water in near-infrared*. Journal of the Optical Society of America, 64(8):1107–1110, 1974.
- [12] C. Koos, P. Vorreau, T. Vallaitis, P. Dumon, W. Bogaerts, R. Baets, B. Esembeson, I. Biaggio, T. Michinobu, F. Diederich, W. Freude, and J. Leuthold. *All-optical high-speed signal processing with silicon-organic hybrid slot waveguides*. Nature Photonics, 3(4):216–219, APR 2009.
- [13] T Baehr-Jones, M Hochberg, C Walker, and A Scherer. *High-Q optical resonators in silicon-on-insulator-based slot waveguides*. Applied Physics Letters, 86(8):081101, February 2005.
- [14] J. Schrauwen, J. Van Lysebettens, T. Claes, K. De Vos, P. Bienstman, D. Van Thourhout, and R. Baets. *Focused-Ion-Beam Fabrication of Slots in Silicon Waveguides and Ring Resonators*. Photonics Technology Letters, IEEE, 20(23):2004–2006, Dec.1, 2008.
- [15] Jonathan Schrauwen, Frederik Van Laere, Dries Van Thourhout, and Roel Baets. *Focused-ion-beam fabrication of slanted grating couplers in silicon-on-insulator waveguides*. Ieee Photonics Technology Letters, 19(9-12):816–818, May-Jun 2007.
- [16] V. Callegari, P. M. Nellen, J. Kaufmann, P. Strasser, and F. Robin. *Focused ion beam iodine-enhanced etching of high aspect ratio holes in InP photonic crystals*. Journal of Vacuum Science & Technology B, 25(6):2175–2179, November 2007.
- [17] www.epixfab.eu.
- [18] Shankar Kumar Selvaraja, Patrick Jaenen, Wim Bogaerts, Dries Van Thourhout, Pieter Dumon, and Roel Baets. *Fabrication of Photonic Wire and Crystal Circuits in Silicon-on-Insulator Using 193-nm Optical Lithography*. J. Lightw. Technol., 27(18):4076–4083, 2009.
- [19] Shankar Kumar Selvaraja. *Wafer-Scale Fabrication Technology for Silicon Photonic Integrated Circuits*. PhD thesis, Universiteit Gent, 2011.

- [20] J. Blasco and C.A. Barrios. *Compact slot-waveguide/channel-waveguide mode-converter*. Lasers and Electro-Optics Europe, 2005. CLEO/Europe. 2005 Conference on, pages 607–607, June 2005.
- [21] Katrien De Vos, Irene Bartolozzi, Etienne Schacht, Peter Bienstman, and Roel Baets. *Silicon-on-Insulator microring resonator for sensitive and label-free biosensing*. Optics Express, 15(12):7610–7615, JUN 11 2007.
- [22] Katrien De Vos, Jordi Girones, Stepan Popelka, Etienne Schacht, Roel Baets, and Peter Bienstman. *SOI optical microring resonator with poly(ethylene glycol) polymer brush for label-free biosensor applications*. Biosens Bioelectron, 24(8):2528–33, Apr 2009.
- [23] Hui Su and Xu Guang Huang. *Fresnel-reflection-based fiber sensor for on-line measurement of solute concentration in solutions*. Sens. Actuators, B, 126(2):579–582, OCT 1 2007.
- [24] Chang-Bong Kim and Chin B Su. *Measurement of the refractive index of liquids at 1.3 and 1.5 micron using a fibre optic Fresnel ratio meter*. Measurement Science and Technology, 15(9):1683, 2004.
- [25] Bradley J. Frey, Douglas B. Leviton, and Timothy J. Madison. *Temperature-dependent refractive index of silicon and germanium*. In Proc. SPIE, page 6273, 2006.

5

Vernier-cascade sensor

Previous chapter presented a slot waveguide ring resonator sensor, and concluded that while it increases the sensitivity compared to a conventional ring resonator sensor, it has several drawbacks. First, there are indications that the biochemical surface modification and interactions are troubled by the less accessible slot, which limits its applicability. Second, the increased sensitivity to refractive index variations in the sample solution and increased optical loss annihilate the benefit of the sensitivity enhancement for the sensor's limit of detection, a more important specification.

The sensor platform would benefit from a transducer that enhances the differential signal between selective analyte binding, and refractive index and temperature noise. Therefore, we studied a Vernier-cascade sensor that enhances the differential resonance wavelength shift between two ring resonators, and that allows to amplify the signal from analyte binding to only one of the resonators relative to the refractive index and temperature noise to which both resonators are exposed. Moreover, compared to a single ring resonator, this sensor provides a more flexible design of its transmission spectrum, which enables faster and cheaper interrogation (chapter 6).

Cascades of ring resonators with a similar concept are widespread to enlarge the free spectral range of lasers [1] and filters [2], and allow tuning their output over a wider range. For biosensing applications, the State Key Laboratory of Modern Optical Instrumentation at Zhejiang University in China contributed extensively. D. Dai introduced the concept theoretically [3], but proposed a digital operation that is not practical and reduces the attainable limit of detection of the sensor. Simultaneously with us, L. Jin et al. [4] extended this work and experimentally demonstrated a 24-fold sensitivity enhancement of a silicon-on-insulator implementation compared to a single ring resonator. However, also the resolution of their sensor interrogation is sub-optimal and limits the attainable limit of detection. We identified an operational regime that allows high-resolution monitoring of spectral shifts with a novel fitting procedure, studied the attainable limit of detection of this sensor and verified our theoretical formulas experimentally.

Section 5.1 introduces the working principle of a Vernier-cascade biosensor before section 5.2 describes its transmission spectrum and operational regimes. Section 5.3 studies the Vernier-cascade's attainable performance, and compares it to that of the optimal single ring resonator sensor. Section 5.4 finalizes this chapter with an experimental verification of the theoretical findings. Next chapter studies the combination of a Vernier-cascade sensor with an on-chip spectral filter for low-cost and broadband interrogation.

5.1 Working principle

A Vernier-cascade sensor (Figure 5.1) consists of two channel drop ring resonators with different optical roundtrip, that are cascaded so that the drop signal of the first resonator serves as the input of the second. Each individual resonator has a comb-like transmission spectrum at its drop port with peaks at the resonance wavelengths (section 2.2.2 in chapter 2). The spectral distance between these peaks, the free spectral range, is inversely proportional to the optical roundtrip of the resonator, so that each resonator in the cascade will have a different free spectral range. As the transmission spectrum of the cascade can be approximated by the product of the transmission spectra of the individual resonators, it will only exhibit peaks at wavelengths for which two resonance peaks of the respective ring resonators (partially) overlap, and the height of each of these peaks will be determined by the amount of overlap.

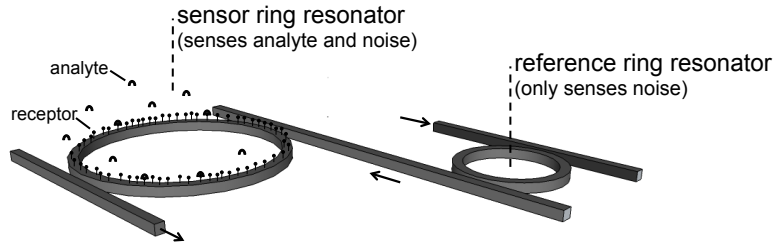


Figure 5.1: A Vernier-cascade sensor consists of two channel drop ring resonators that are cascaded, so that the drop signal of the first resonator serves as the input of the second. Only the sensor resonator has receptors immobilized on its surface and selectively reacts to the analyte. Together with the reference resonator it also reacts to common refractive index and temperature noise. The ring resonators have a different optical roundtrip, and therefore a comb spectrum with different free spectral range.

Only one ring resonator, the sensor resonator, has receptors immobilized on its surface and selectively reacts to the analyte. Together with the other ring resonator, the reference resonator, it also reacts to refractive index and temperature noise. Hence, this noise causes a resonance wavelength shift of both resonators, and therefore only a small shift of the total transmission (Figure 5.2). However, selective binding of the analyte to the sensor resonator causes a differential resonance wavelength shift between the resonators, and thus results in a much larger shift of the total transmission. This can have a positive impact on the signal-to-noise ratio and limit of detection.

To minimize the differential noise between the resonators, they are preferably placed close to each other in the same environment. One method is to chemically modify their surfaces differently with a molecular printer (section 2.6 in chapter 2), and expose them to the same noise factors by immersing them both in the sample liquid. Alternatively, a solid cladding with a similar thermo-optic coefficient as water can cover the reference ring resonator and isolate its evanescent field from the sample liquid (section 2.4.3 in chapter 2). While this relaxes the required spatial resolution of the chemical surface modification, the Vernier-cascade sensor will in this case only filter temperature noise.

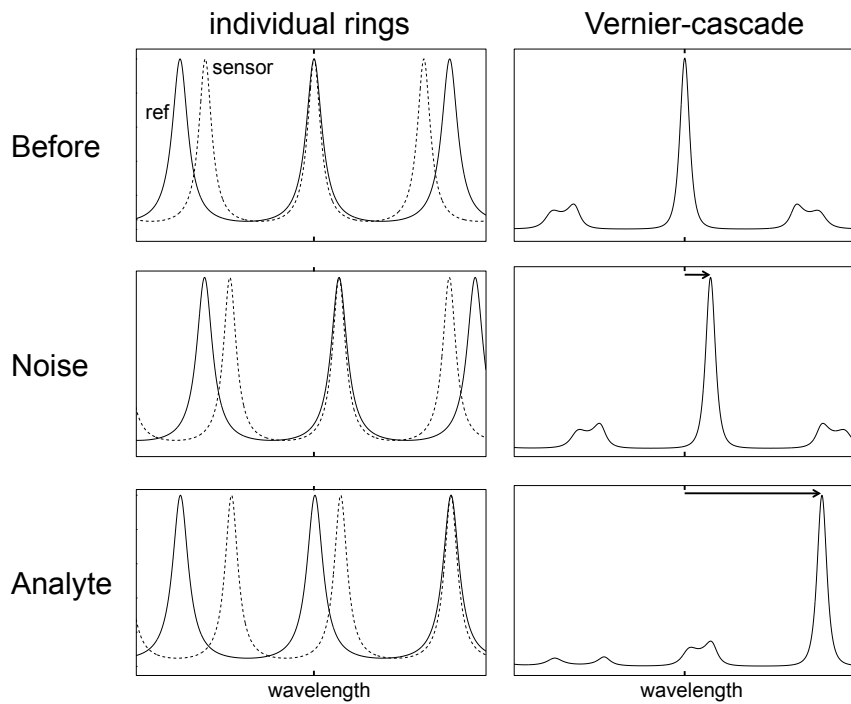


Figure 5.2: The transmission spectrum of the cascade will only have peaks at wavelengths for which two resonance peaks of the respective ring resonators overlap. Common noise will shift the resonances of both resonators, and only results in a small shift of the Vernier-cascade spectrum. However, selective analyte binding to the sensor resonator results in a differential resonance wavelength shift between the resonators, and therefore in a much larger shift of the Vernier-cascade transmission spectrum. The signal-to-noise ratio and limit of detection can benefit from this.

5.2 Transmission spectrum

Previous section introduced the working principle of a Vernier-cascade sensor, and described its increased sensitivity to differential resonance wavelength shifts between the two resonators. This section analyzes its transmission spectrum, and selects an attractive operational regime for sensing. It introduces formulas that describe the sensor's transmission spectrum in this regime, and that allow to design and predict the performance of the sensor.

5.2.1 Operational regimes

When the resonators have a small roundtrip difference and comparable roundtrip loss, the full-width at half-maxima of their resonance peaks are approximately equal. Based on the relation between this full-width at half-maximum and the free spectral range difference between the resonators, two regimes are identified:

The first regime (left in Figure 5.3) occurs when the free spectral range difference between the two resonators in the cascade is large compared to the full-width at half-maximum of the resonance peaks of the individual resonators. The transmission spectrum of the cascade then exhibits isolated peaks, of which the neighboring peaks are inhibited. In this regime the Vernier-cascade behaves as a discrete sensor, of which the transmission peak will hop from one reference ring resonance wavelength to another due to a differential resonance wavelength shift. Hence, the spectral shifts of the Vernier-cascade can only be measured with a resolution in the order of the free spectral range of the reference ring resonator, which heavily restricts its limit of detection.

A second regime occurs however (right in Figure 5.3) when the free spectral range difference between the two resonators in the cascade is small compared to the full-width at half-maxima of their resonance peaks. In this regime a periodic envelope signal is superposed on the constituent transmission peaks, which can shift smoothly without significantly changing shape in contrast with the discrete hopping of the transmission peaks in the first regime. The second regime is therefore more suited for sensing than the first regime, since it allows accurate monitoring of spectral shifts through data-fitting to the envelope signal. Next section introduces formulas that describe the transmission spectrum, and that can be fitted to experimental data.

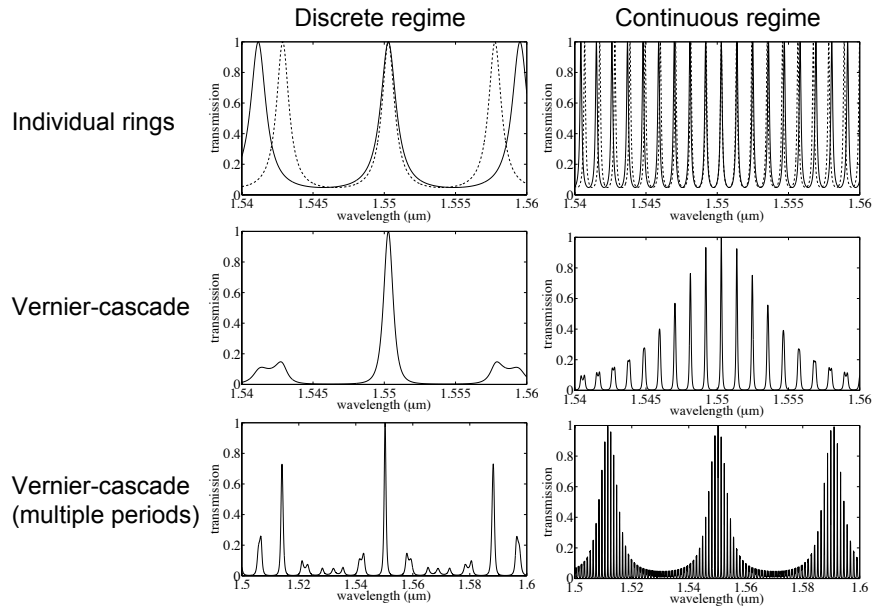


Figure 5.3: A discrete operational regime of the Vernier-cascade sensor occurs when the free spectral range difference between the two resonators is large compared to the full-width at half-maximum of the resonance peaks of the individual resonators. The transmission spectrum of the cascade then exhibits isolated peaks, of which the neighboring peaks are inhibited. In this regime the Vernier-cascade behaves as a discrete sensor, of which the transmission peak will hop from one reference ring resonance wavelength to another due to a differential resonance wavelength shift, which restricts the limit of detection. An operational regime that allows continuous, hop-free, monitoring of spectral shifts has more benefits for sensing, and occurs when the free spectral range difference between the two resonators is small compared to the full-width at half-maximum of the resonance peaks of the individual resonators. A periodic envelope signal is then superposed on the constituent transmission peaks, which can accurately be monitored with data-fitting.

5.2.2 Transmission spectrum in the continuous regime

The transmission spectrum of a Vernier-cascade operating in the continuous regime defined in previous section consists of sharp constituent peaks that are modulated with a periodic envelope signal (Figure 5.4).

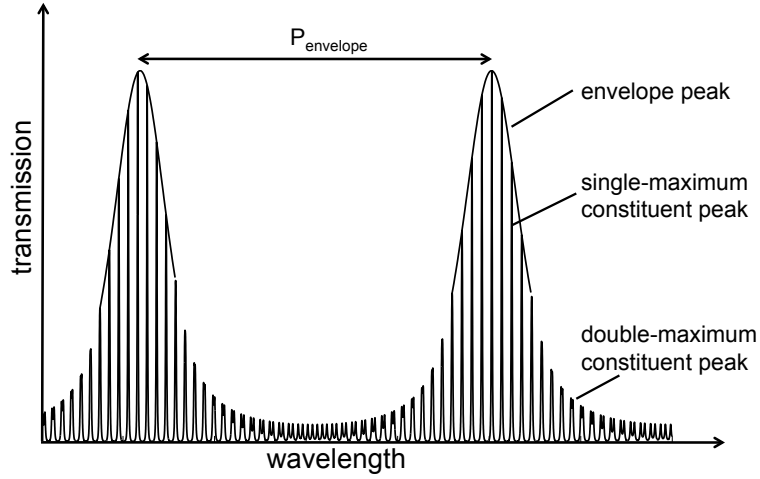


Figure 5.4: The transmission spectrum of a Vernier-cascade that operates in the continuous regime manifests a periodic envelope signal superposed on sharp constituent peaks. The low intensity peaks far from the center of the envelope peaks have two maxima, while the higher intensity peaks closer to the center have a single maximum.

The envelope period depends on the roundtrip of the two individual resonators through their free spectral range values FSR_{sensor} and $FSR_{reference}$. Neglecting group index dispersion, it can be formulated as (appendix E):

$$P_{envelope} = \frac{FSR_{sensor} \cdot FSR_{reference}}{|FSR_{sensor} - FSR_{reference}|} \quad (5.1)$$

The required roundtrip difference between the two resonators to obtain a predefined envelope period decreases quadratically with linearly increasing values of both resonators' roundtrip (decreasing FSR_{sensor} and $FSR_{reference}$). Note that in practice the envelope period can not be chosen larger than the available wavelength range of the measurement equipment, so that the second regime (small denominator) typically requires

that the cascade consists of resonators with very large roundtrips (small numerator).

As each peak in the transmission spectrum of the individual ring resonators is well-approximated by a Lorentzian function (section 2.2.3 in chapter 2), each of the constituent peaks in the transmission spectrum of the cascade can be described as the product of two Lorentzian functions that are shifted relative to each other (appendix F):

$$T_{const}(\lambda) = \frac{T_{max} \cdot \left(\frac{FWHM_{ring}}{2}\right)^4}{\left(\left(\frac{FWHM_{ring}}{2}\right)^2 + \left(\lambda - \lambda_m - \frac{\Delta\lambda}{2}\right)^2\right) \cdot \left(\left(\frac{FWHM_{ring}}{2}\right)^2 + \left(\lambda - \lambda_m + \frac{\Delta\lambda}{2}\right)^2\right)} \quad (5.2)$$

where T_{max} is the maximal possible transmission of a constituent peak, $FWHM_{ring}$ is the full-width at half-maximum of each of the resonance peaks of the individual ring resonators, and where λ_m and $\Delta\lambda$ are respectively the mean of and the difference between the two resonance wavelengths under consideration from both combs.

Depending on their position in the envelope peak, two different shapes of the constituent peaks exist (Figure 5.4 and appendix F). Double-maximum constituent peaks occur in the low-intensity tails of the envelope peak, and arise when the difference between the corresponding individual resonance wavelengths is larger than the full-width at half-maximum of the individual resonance peaks ($\Delta\lambda > FWHM_{ring}$). Much higher single-maximum constituent peaks appear closer to the center of the envelope peak, where the difference between the individual resonance wavelengths is smaller than or equal to the full-width at half-maximum of the resonance peaks ($\Delta\lambda \leq FWHM_{ring}$).

The envelope peak in the transmission of the Vernier-cascade formed by the maxima of the single-maximum constituent peaks is in good approximation given by the square of a Lorentzian function (appendix G):

$$T_{envelope}(\lambda) = \left(\frac{\sqrt{T_{max}} \left(\frac{FWHM_{envelope}}{2\sqrt{\sqrt{2}-1}}\right)^2}{\left(\frac{FWHM_{envelope}}{2\sqrt{\sqrt{2}-1}}\right)^2 + (\lambda - \lambda_{central})^2} \right)^2 \quad (5.3)$$

It has a maximal transmission T_{max} at its central wavelength $\lambda_{central}$ and a full-width at half-maximum

$$FWHM_{envelope} = 2 \cdot \sqrt{\sqrt{2}-1} \cdot \frac{FWHM_{ring} \cdot FSR_{min}}{|FSR_{reference} - FSR_{sensor}|} \quad (5.4)$$

with $FSR_{min} = \min(FSR_{sensor}, FSR_{reference})$

5.3 Performance

Selective interactions between analyte molecules and immobilized receptor molecules on the sensor resonator result in a shift of the envelope signal of the Vernier-cascade and forms a binding curve similar to that of a single ring resonator sensor (section 2.3.3 in chapter 2). Its initial slope represents the analyte concentration, which can reliably be detected down to the limit of detection.

The potential benefits of a Vernier-cascade are twofold. First, the differential resonance wavelength shift between its resonators is enhanced, increasing the slope sensitivity. Second, variations of the refractive index of the sample solution and of the temperature are directly compensated by the reference resonator, decreasing their impact on the noise of the spectral position. However, the envelope peak of the Vernier-cascade sensor is much broader than a resonance dip of a single ring resonator, decreasing the accuracy with which its position can be determined and also decreasing the temporal resolution.

Before section 5.3.3 compares the limit of detection of a Vernier-cascade with that of an individual ring resonator sensor, section 5.3.1 introduces a formula for the sensitivity enhancement and section 5.3.2 presents a fitting algorithm that allows to determine the envelope peak position in a noise resistant way.

5.3.1 Sensitivity enhancement

A differential resonance wavelength shift between the sensor resonator and reference resonator results in a much larger spectral shift of the transmission spectrum of the Vernier-cascade (Figure 5.2), increasing the sensitivity towards analyte molecules that only bind to the sensor resonator. The spectral shift of a Vernier-cascade sensor in response to changes of the effective refractive index of the sensor resonator waveguide is (appendix H):

$$\Delta\lambda = \underbrace{\frac{\lambda \cdot \Delta n_{eff,sensor}}{n_{g,sensor}}}_{\text{sensor ring sensitivity}} \cdot \underbrace{\frac{FSR_{reference}}{FSR_{reference} - FSR_{sensor}}}_{\text{sensitivity enhancement } S^*} \quad (5.5)$$

with $n_{g,sensor}$ and $\Delta n_{eff,sensor}$ respectively the group refractive index and the change of the effective refractive index of the sensor resonator, $FSR_{reference}$ and FSR_{sensor} the free spectral range values of the corresponding resonators, and λ the wavelength in vacuum.

The first factor of equation (5.5) expresses the resonance wavelength shift of the sensor resonator in response to an effective refractive index change (section 2.3.2 in chapter 2 and appendix C). The second factor enhances this shift, since in practical Vernier-cascade sensors the free spectral range of the reference is much larger than the free spectral range difference between the resonators ($FSR_{reference} \gg |FSR_{reference} - FSR_{sensor}|$). While the resonance wavelength of a ring resonator sensor always increases with an increasing effective refractive index, the Vernier-cascade sensor can shift in a predefined direction depending on the relation between the free spectral range values of its ring resonators.

For a predefined envelope period $P_{envelope}$ (equation 5.1), which should be chosen considering the available wavelength range of the measurement instrument and grating couplers, the sensitivity of a Vernier-cascade sensor is inversely proportional to the free spectral range of the sensor resonator:

$$|\Delta\lambda| = \frac{\lambda \cdot \Delta n_{eff,sensor}}{n_{g,sensor}} \cdot \frac{P_{envelope}}{FSR_{sensor}} \quad (5.6)$$

The longer the resonators in the Vernier-cascade, the larger its sensitivity.

5.3.2 Noise resistant tracking of the envelope peak

When the impact of liquid refractive index variations and temperature variations on the sensor signal are sufficiently compensated by the reference resonator in the Vernier-cascade, the precision of the envelope peak central wavelength determination dominates the binding curve noise. Just taking the wavelength of maximal transmission of the sensor is very intolerant to noise, because it is susceptible to hopping between different constituent peaks and can give errors as large as the free spectral range of the resonators. We propose a two-step method to precisely extract the envelope peak central wavelength from a discretized and noisy spectrum (Figure 5.5).

The first step determines the top of the single-maximum constituent peaks by fitting equation (5.2) to the most central and highest constituent

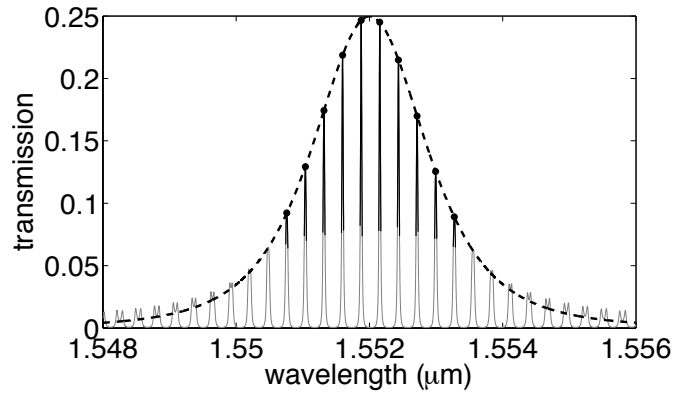


Figure 5.5: Illustration of the fitting procedure on a calculated transmission spectrum (grey) of a silicon Vernier-cascade sensor. The central wavelength of the envelope peak is determined in a noise resistant way by first fitting equation (5.2) to the highest constituent peaks (full lines) and determining their analytical maxima (black dots). Then equation (5.3) is fitted (dashed line) with the central wavelength as a parameter.

peaks, and by calculating the position and value of their analytical maxima.

The second step determines the central wavelength of the envelope peak by fitting equation (5.3) to the output of the first step, with the central wavelength as one of the fitting parameters.

The error on the determined central wavelength is ten times smaller than the distance between the constituent peaks, as found by Monte-Carlo simulations with the method proposed in section 2.4.4 of chapter 2 and as confirmed by our measurement (section 5.4). Therefore, this procedure is an order of magnitude better than when just taking the wavelength of maximal transmission.

5.3.3 Limit of detection

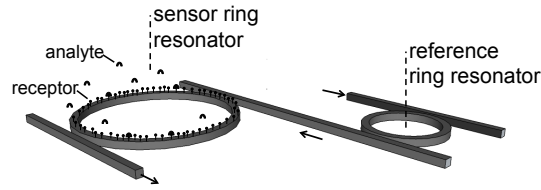
This section compares the limit of detection (*LOD*) of a Vernier-cascade sensor (Figure 5.6(a)) with that of an individual ring resonator sensor that is unconnected to its reference sensor (Figure 5.6(b)). The limit of

detection of both configurations can be expressed as (section 2.4.1):

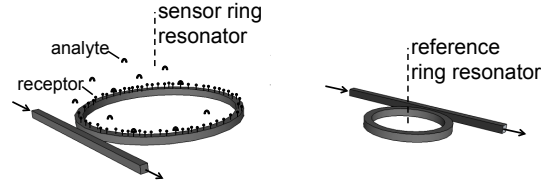
$$LOD_{ring} \approx 3.29 \cdot 2\sqrt{3} \frac{\sqrt{2} \cdot \sigma_{\Delta\lambda,ring}}{\sqrt{R_{t,ring}} \cdot T^{\frac{3}{2}} \cdot S_{slope,ring}} \quad (5.7)$$

$$LOD_{Vernier} \approx 3.29 \cdot 2\sqrt{3} \frac{\sigma_{\Delta\lambda,Vernier}}{\sqrt{R_{t,Vernier}} \cdot T^{\frac{3}{2}} \cdot S_{slope,Vernier}} \quad (5.8)$$

with R_t the temporal resolution of the binding curve, T the measurement time, S_{slope} the slope sensitivity, $\sigma_{\Delta\lambda,Vernier}$ the standard deviation of the noise on the binding curve of the Vernier-cascade, and $\sigma_{\Delta\lambda,ring}$ the standard deviation of the uncorrelated noise of the individual biosensor and reference sensor. The latter is multiplied by a factor $\sqrt{2}$ to account for taking the difference between the two signals to obtain the binding curve.



(a) Connected biosensor and reference resonator in a Vernier-cascade configuration



(b) Unconnected biosensor and reference resonator configuration for separate interrogation

Figure 5.6

The ratio between the limits of detection

$$\frac{LOD_{ring}}{LOD_{Vernier}} = \frac{S_{slope,Vernier}}{S_{slope,ring}} \cdot \frac{\sqrt{R_{t,Vernier}}}{\sqrt{R_{t,ring}}} \cdot \frac{\sqrt{2} \cdot \sigma_{\Delta\lambda,ring}}{\sigma_{\Delta\lambda,Vernier}} \quad (5.9)$$

would be larger than 1 when in favor of the Vernier-cascade.

The potential benefit of the Vernier-cascade configuration over the unconnected configuration is its sensitivity enhancement (section 5.3.1):

$$\frac{S_{slope,Vernier}}{S_{slope,ring}} = S^* > 1$$

with the sensitivity enhancement factor S^* .

However, a first drawback of the Vernier-cascade configuration compared to the unconnected configuration is the reduced temporal resolution when scanning the spectrum with a wavelength-tunable laser. It is inversely proportional to the required scan range, which is approximately equal to the period of the sensor signal. Therefore the proportion of the temporal resolutions becomes

$$\frac{R_{t,Vernier}}{R_{t,ring}} = \frac{\frac{laser\ scan\ speed}{P_{envelope}}}{\frac{laser\ scan\ speed}{FSR_{ring}}} = \frac{FSR_{ring}}{P_{envelope}} \quad (5.10)$$

with the envelope period of the Vernier-cascade signal $P_{envelope}$ typically at least an order of magnitude larger than the free spectral range of the individual ring resonator FSR_{ring} . The optimal individual ring resonator has a very large roundtrip length (section 2.4.4 in chapter 2) that would induce too much loss in a Vernier-cascade. Therefore, the free spectral range of an optimal individual ring resonator FSR_{ring} is smaller than the free spectral range of the sensor resonator FSR_{sensor} in the optimal Vernier-cascade, so that with equation (5.6), equation (5.10) becomes:

$$\begin{aligned} \frac{R_{t,Vernier}}{R_{t,ring}} &< \frac{FSR_{sensor}}{P_{envelope}} \\ \Leftrightarrow \frac{R_{t,Vernier}}{R_{t,ring}} &< \frac{1}{S^*} \end{aligned}$$

A second drawback of the Vernier-cascade is the increased noise on its binding curve:

If the reference ring does not sufficiently compensate the noise, i.e. if the differential noise in the refractive index and temperature of the sample liquid between the biosensor ring and reference ring dominates the noise on the binding curve, the Vernier-cascade amplifies the noise together with the analyte signal, canceling the benefit of the sensitivity enhancement. In that case the ratio of the standard deviations of the noise on the

binding curve becomes

$$\frac{\sqrt{2} \cdot \sigma_{\Delta\lambda, ring}}{\sigma_{\Delta\lambda, Vernier}} = \frac{\sqrt{2}}{S^*} \quad (5.11)$$

so that the ratio of the limits of detection of both configurations (equation 5.9) becomes:

$$\frac{LOD_{ring}}{LOD_{Vernier}} < S^* \cdot \frac{1}{\sqrt{S^*}} \cdot \frac{\sqrt{2}}{S^*} = \frac{\sqrt{2}}{\sqrt{S^*}},$$

of which the right hand side is much smaller than 1 for all practical designs.

If the refractive index noise and temperature noise are sufficiently compensated by the reference sensors to make optical noise on the transmission spectra dominant, the inaccuracies in the extraction of the spectral position by data-fitting determine the noise on the binding curve. For the maximal envelope period equal to the bandwidth of our grating couplers (40 nm) and a roundtrip length of the sensor resonator in the Vernier-cascade as large as 4 mm, the sensitivity enhancement is $S^* = P_{envelope}/FSR_{sensor} = 267$. A Monte-Carlo simulation similar to the one described in section 2.4.4 of chapter 2 resulted in a minimal standard deviation on the fitted central wavelength of the noisy envelope peak of 10 pm, which is much larger than the 30 fm standard deviation on the resonance wavelength extraction of the optical individual ring (section 2.4.4). With these optimistic parameters, equation (5.9) results in

$$\frac{LOD_{ring}}{LOD_{Vernier}} < 267 \cdot \frac{1}{\sqrt{267}} \cdot \frac{\sqrt{2} \cdot 30 \text{ fm}}{10000 \text{ fm}} = 0.07 \quad (5.12)$$

so that the limit of detection of a Vernier-cascade is also in this case worse than that of the individual read-out of the biosensor and reference sensor.

A very important limiting factor of the Vernier-cascade's limit of detection is the heavily reduced temporal resolution, due to the large envelope period and consequent laser scan period. However, chapter 6 introduces a method to use the broad envelope spectrum of this sensor in its benefit to achieve a higher temporal resolution by replacing interrogation by wavelength-scanning of a laser with interrogation with a broadband light source and an on-chip spectral filter.

5.4 Experimental proof-of-concept

In order to experimentally verify the formulas that describe the transmission spectrum (section 5.2) and the sensitivity enhancement of differential resonance wavelength shifts between the two resonators (section 5.3.1), we implemented and characterized a Vernier-cascade sensor in silicon-on-insulator. Since the sensor preferably consists of ring resonators with a large roundtrip, we assessed whether the large refractive index contrast of silicon waveguides allows to make the sensor compact in order to be compatible with highly multiplexed sensing.

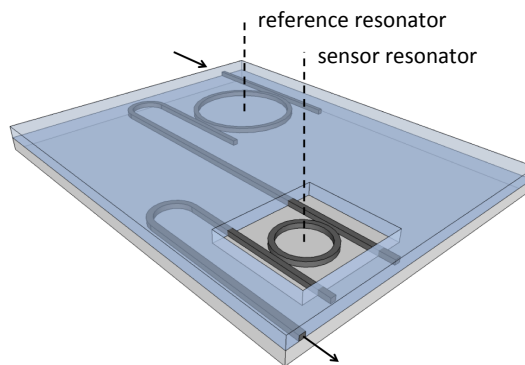


Figure 5.7: To experimentally proof the concept, a cladding on the reference ring resonator shields its evanescent field from liquid flowing over the chip, so that only the sensor ring resonator reacts to refractive index changes of that liquid and differential resonance wavelength shifts between the resonators can be applied.

To apply a refractive index change between the two resonators of the Vernier-cascade, a cladding covers the complete chip with only a window for the sensor ring resonator (Figure 5.7). Only this resonator's evanescent field interacts with refractive index changes in the liquid flowing over the chip. While this Vernier-cascade sensor does not allow to compensate noise in the refractive index of the liquid or non-specific binding such as the sensor depicted in Figure 5.1, it does compensate for temperature noise if both resonators are in contact with the liquid and if they both have the same temperature dependence.

Section 5.4.1 presents our silicon Vernier-cascade sensor, and section 5.4.2 finalizes by comparing the experimental sensitivity enhancement of the sensor with the theoretical one.

5.4.1 Compact silicon Vernier-cascade sensor

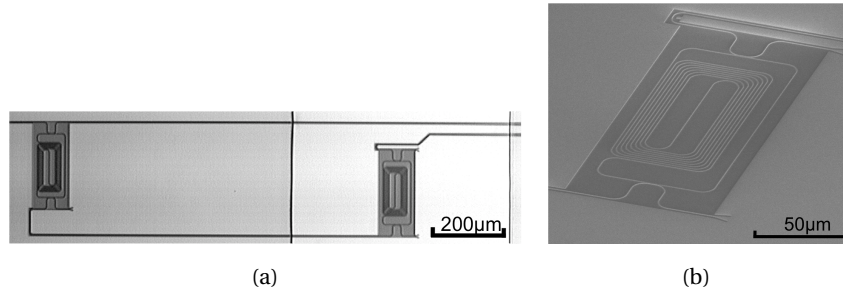


Figure 5.8: (a) The silicon Vernier-cascade sensor used for the proof-of-concept measurements consists of two ring resonators that are cascaded similar to the concept depicted in Figure 5.7. A 500 nm-thick silicon oxide cladding covers the complete chip except for the etched opening to the sensor ring resonator. (b) The footprint of the 2.5 mm-long resonators is reduced by folding the cavity.

A silicon Vernier-cascade sensor was fabricated with CMOS-compatible 193 nm optical lithography and dry etching, corresponding to the process described before (section 2.1.1 in chapter 2) and elaborated in [5, 6]. It entirely consists of 450 nm-wide and 220 nm-high strip waveguides that do not complicate the biochemical surface modification compared to a single ring resonator sensor. The physical roundtrip lengths of the reference resonator (2528 μm) and sensor resonator (2514 μm) make the cascade work in the second operational regime (section 5.2.1) with an envelope period (4.5 nm) much smaller than the bandwidth of our grating couplers (40 nm, see section 2.8.1 in chapter 2). Employing the high refractive index contrast of silicon-on-insulator by folding the cavity with a bend radius of 7 μm reduces the footprint of the resonators to only 200 $\mu\text{m} \times 70 \mu\text{m}$, so that despite the large roundtrips still many sensors fit on a chip to provide highly multiplexed sensing. This technique was proposed before by D.-X. Xu et al. [7]. All four directional couplers follow the design described before (section 2.2.4 in chapter 2) with 6 μm length, 180 nm gap and 7 μm bend radius. The complete chip was covered with 500 nm silicon oxide by plasma deposition (at that time the Cyclotene-process was not yet in place) and a window was etched to the second resonator in the cascade by consecutive dry and wet etching.

The grating-coupled fiber-to-fiber transmission (method in sections 2.8.1 and 2.8.2 in chapter 2) of the sensor immersed in deionized water (Figure 5.9) confirms that a periodic envelope signal is superposed on the

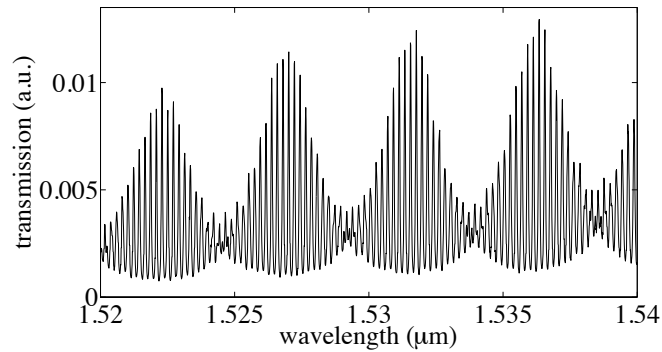


Figure 5.9: The measured transmission of the silicon Vernier-cascade sensor (Figure 5.8) immersed in water confirms that a periodic envelope signal is superposed on the constituent peaks. The height of the envelope peaks varies due to the wavelength-dependent coupling efficiency of the grating couplers.

constituent peaks. Moreover, formulas (5.2) and (5.3) fit very well to the measured spectrum (Figure 5.10) with the previously introduced method (section 5.3.2), further validating the theory and allowing to extract the central wavelength with a standard deviation (18 pm) that is ten times smaller than the distance between the constituent peaks.

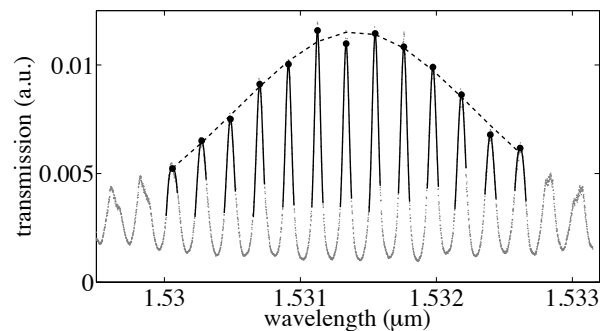


Figure 5.10: The qualitative fit of formulas (5.2) and (5.3) to the measured transmission spectrum validates the theory, and extracts the central wavelength with a standard deviation of 18 pm. This is less than a tenth of the distance between the constituent peaks (214 pm), thus confirming the added value of the fitting procedure (section 5.3.2).

Note however that this implementation is suboptimal and only serves as a proof-of-principle. The coupler length is not optimized, and the propagation loss (19 dB/cm in water) prior to oxide deposition was unexpectedly high on the measured die. This results in broader constituent peaks and a broader envelope peak, which has a negative impact on the confidence interval of the fitted central wavelength (18 pm standard deviation on the central wavelength). Moreover, the process for the cladding is also sub-optimal, since the top cladding cannot selectively be removed from the waveguide, resulting in either damaged waveguides or incomplete cladding removal. A silicon nitride etch-stop layer would help [8], but increases the number of fabrication steps. Section 2.4.3 introduced photopatternable Cyclotene from Dow chemical as a promising alternative cladding material, for being more easy to pattern and having a thermo-optic coefficient closer to that of water. Next chapter describes a Vernier-cascade sensor made with this material.

5.4.2 Experimental sensitivity enhancement

To measure the sensitivity enhancement of the Vernier-cascade compared to a single ring resonator, the shift of the envelope signal was measured when changing between flowing deionized water and three aqueous solutions of NaCl with different concentrations. The refractive index of each of these solutions was calculated [9]. The oxide-clad reference resonator does not respond to these changes, so that the liquid changes result in a differential shift between the two resonators and therefore in a sensitivity enhancement. To allow controlled delivery of liquids to the sensor, a microfluidic channel with $600\mu\text{m} \times 50\mu\text{m}$ cross section was made in PDMS by casting (section 2.7 in chapter 2) and directly bonded to the sensor chip at 135°C after having applied a short oxygen plasma treatment to both surfaces [10]. The liquids were pumped through the channel over the sensor ring resonator with a syringe pump at a $5\mu\text{L}/\text{min}$ flow rate. Since the thermo-optic coefficient of silicon oxide differs from that of water, the sensor is not temperature independent and therefore the chip was mounted on a temperature-stabilized chuck to avoid drifting of the sensor signal.

The measured sensitivity of the sensor is 2170 nm/RIU, 29 times higher than that of a single ring resonator sensor (Figure 5.11). Despite this significant sensitivity enhancement, this sensor does however not improve the limit of detection due to its broader transmission and the resulting impact on the achievable temporal resolution and fitting accuracy (section

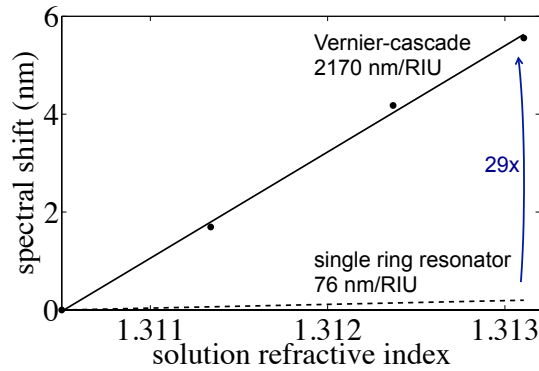


Figure 5.11: The envelope signal of the studied silicon Vernier-cascade sensor is 29 times more sensitive to liquid refractive index changes than a single ring resonator, as expected from the previously derived theory. The dots represent the measured envelope shift when changing the flow between deionized water and aqueous solutions of NaCl with different concentrations. The linear fit to this experimental data (solid line) reveals a sensitivity of 2169nm/RIU, compared to only 76 nm/RIU for an individual ring resonator (dashed line).

5.3.3). Nevertheless next chapter introduces a beneficial application of this broad envelope signal.

5.5 Conclusions

When interrogated by repeatedly scanning the wavelength of a tunable laser, a Vernier-cascade sensor does not improve the limit of detection compared to an individual ring resonator sensor that is interrogated independently from its reference sensor. The main limitation is the broader envelope spectrum, and consequent reduced temporal resolution and increased noise on the binding curve. However, next chapter introduces another interrogation method of the Vernier-cascade that employs its broad envelope spectrum to reduce the cost of interrogation and increase the temporal resolution.

References

- [1] B Liu, A Shakouri, and JE Bowers. *Wide tunable double ring resonator coupled lasers*. IEEE Photonics Technology Letters, 14(5):600–602, MAY 2002.
- [2] P Rabiei and WH Steier. *Tunable polymer double micro-ring filters*. IEEE Photonics Technology Letters, 15(9):1255–1257, SEP 2003.
- [3] Daoxin Dai. *Highly sensitive digital optical sensor based on cascaded high-Q ring-resonators*. Optics Express, 17(26):23817–23822, 2009.
- [4] Lei Jin, Mingyu Li, and Jian-Jun He. *Highly-sensitive silicon-on-insulator sensor based on two cascaded micro-ring resonators with vernier effect*. Opt. Commun., 284(1):156 – 159, 2011.
- [5] Shankar Kumar Selvaraja, Patrick Jaenen, Wim Bogaerts, Dries Van Thourhout, Pieter Dumon, and Roel Baets. *Fabrication of Photonic Wire and Crystal Circuits in Silicon-on-Insulator Using 193-nm Optical Lithography*. J. Lightw. Technol., 27(18):4076–4083, 2009.
- [6] Shankar Kumar Selvaraja. *Wafer-Scale Fabrication Technology for Silicon Photonic Integrated Circuits*. PhD thesis, Universiteit Gent, 2011.
- [7] D. X. Xu, A. Densmore, A. Delâge, P. Waldron, R. McKinnon, S. Janz, J. Lapointe, G. Lopinski, T. Mischki, E. Post, P. Cheben, and J. H. Schmid. *Folded cavity SOI microring sensors for high sensitivity and real time measurement of biomolecular binding*. Optics Express, 16(19):15137–15148, 2008.
- [8] D-X Xu, M. Vachon, A. Densmore, R. Ma, S. Janz, A. Delage, J. Lapointe, P. Cheben, J. H. Schmid, E. Post, Sonia Messaoudene, and Jean-Marc Fedeli. *Real-time cancellation of temperature induced resonance shifts in SOI wire waveguide ring resonator label-free biosensor arrays*. Optics Express, 18(22):22867–22879, Oct 2010.
- [9] Hui Su and Xu Guang Huang. *Fresnel-reflection-based fiber sensor for on-line measurement of solute concentration in solutions*. Sens. Actuators, B, 126(2):579–582, OCT 1 2007.
- [10] S Bhattacharya, A Datta, JM Berg, and S Gangopadhyay. *Studies on surface wettability of poly(dimethyl) siloxane (PDMS) and glass under oxygen-plasma treatment and correlation with bond strength*.

IEEE Journal of Microelectromechanical Systems, 14(3):590–597,
JUN 2005.

6

Low-cost and fast interrogation of a Vernier-cascade sensor

Interrogating ring resonator sensors by repeatedly measuring their transmission spectra by scanning the wavelength of a laser and measuring the transmitted power for different wavelengths is widespread. It offers the high spectral resolution required to accurately monitor shifts of the narrow resonances (linewidth in the order of 10 pm) through the narrow linewidth of external cavity lasers (down to a few femtometers). Additionally, this method provides sufficient power budget to interrogate hundreds of sensors simultaneously for multiplexed sensing. However, the required external cavity laser and wavelength monitoring system increase the cost and size of the interrogation instrument. Moreover, the low temporal resolution of the wavelength scanning is disadvantageous for the limit of detection.

One way to reduce the cost and size of the interrogation instrument, while increasing its temporal resolution, is to apply intensity interrogation instead of wavelength interrogation, either by measuring the sensor's transmission with a fixed-wavelength laser [1] or broadband source [2, 3]. However, this can be impractical due to the non-linear response and the

need to align the sensor's transmission spectrum to the spectrum of the source or detector. This can be overcome by implementing wavelength interrogation with a cheap broadband source and on-chip wavelength filtering to divide the sensor's transmission spectrum in multiple wavelength channels and distribute them to spatially separated output ports. The multiple outputs can be monitored in parallel with a detector array, a helpful component for any multiplexed sensor platform (section 2.8.3 in chapter 2) that provides a temporal resolution equal to its line rate (typically several kHz).

Yet, compact silicon-on-insulator spectral filters typically have a spectral resolution in the nanometer range [4], which is too low to resolve the sharp resonances of a ring resonator sensor (tens of picometers). In [5] a silicon ring resonator sensor with integrated photonic crystal filter is proposed, but the sharp resonances of the sensor put very stringent requirements on the filter and so far no low detection limits have been shown.

Therefore, we propose to use a Vernier-cascade sensor (chapter 5) instead of a single ring resonator sensor for this purpose, since it has an envelope signal that is much broader than the resonance width of a single resonator, and hence can more easily be resolved by an on-chip spectral filter. Additionally it enhances the sensitivity up to two orders of magnitude, compensating the low spectral resolution of this interrogation method.

Next section details the working principle of the interrogation of a Vernier-cascade sensor with a broadband light source and an on-chip spectral filter, before section 6.2 compares its limit of detection with that of an individual ring resonator sensor interrogated by scanning the wavelength of a laser. Then, sections 6.3 and 6.4 describe the implementation and characterization of a Vernier-cascade sensor with a compact integrated arrayed waveguide grating spectral filter.

6.1 Working principle

The transmission spectrum of a Vernier-cascade sensor exhibits a periodic envelope signal superimposed on sharp constituent peaks, and can be measured with a low-cost broadband light source by dividing it into different wavelength channels with an integrated spectral filter that distributes them to spatially separated output ports (Figure 6.1). A detector array or camera simultaneously measures the power transmitted by each of the ports with a temporal resolution far superior to that of the laser scanning method.

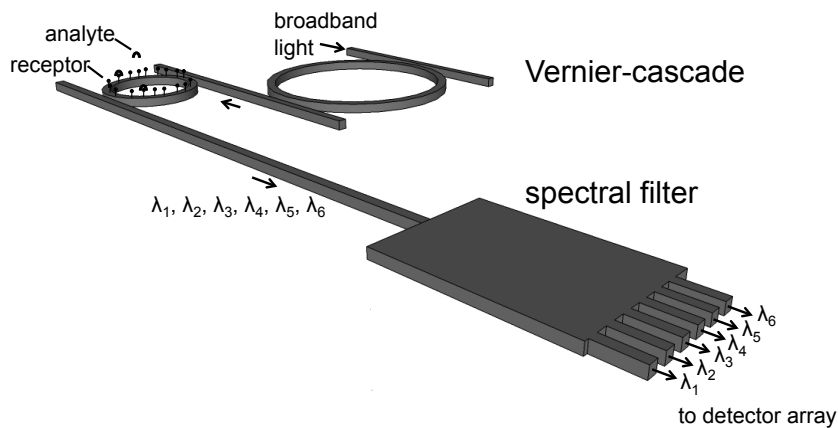
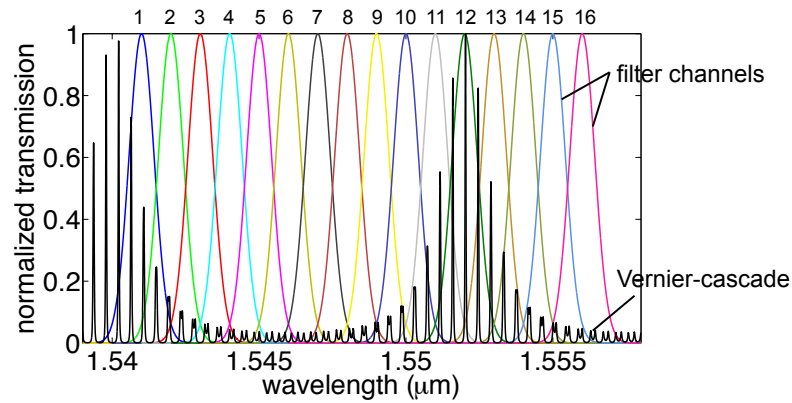
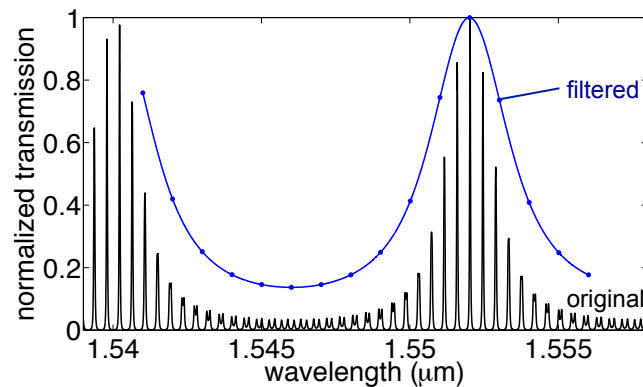


Figure 6.1: The transmission spectrum of a Vernier-cascade sensor can be measured with a low-cost broadband light source by dividing it into different wavelength channels with an integrated spectral filter that distributes them to spatially separated output ports. These can be monitored in parallel with a detector array.

The filtered broadband transmission spectrum (Figure 6.2) is the convolution of the Vernier-cascade spectrum with the transmission function of the spectral filter to each of its channels, discretized with the channel spacing of the filter. If the bandwidth of that transmission function is larger than the distance between the constituent peaks in the Vernier-cascade spectrum, the Vernier-cascade's filtered broadband transmission spectrum directly reveals the envelope signal, of which the spectral position can be accurately monitored by data-fitting. Note however that the extinction is reduced by the convolution.



(a)



(b)

Figure 6.2: (a) The transmission spectrum of a Vernier-cascade has a periodic envelope signal superimposed on sharp constituent peaks (black). When using a broadband light source, filtering this spectrum in different wavelength channels (a color for each channel) that each enclose multiple constituent peaks, (b) directly reveals the envelope signal (blue). Here, as a simulated example, a Gaussian filter channel transmission function with 1 nm full-width at half-maximum was chosen to filter the transmission of a silicon Vernier-cascade with 1.3 mm-long cavities and 12 nm envelope period. Note that the averaging effect of the filter reduces the extinction.

6.2 Limit of detection

Similar to section 5.3.3 in chapter 5, the ratio of the limits of detection of an individual ring resonator sensor that is interrogated independently from its reference sensor by scanning the wavelength of a tunable laser, and a Vernier-cascade sensor interrogated with a broadband light source and an on-chip spectral filter, can be expressed as

$$\frac{LOD_{ring}}{LOD_{Vernier}} = \frac{S_{slope,Vernier}}{S_{slope,ring}} \cdot \frac{\sqrt{R_{t,Vernier}}}{\sqrt{R_{t,ring}}} \cdot \frac{\sqrt{2} \cdot \sigma_{\Delta\lambda,ring}}{\sigma_{\Delta\lambda,Vernier}} \quad (6.1)$$

with R_t the temporal resolution of the binding curve, T the measurement time, S_{slope} the slope sensitivity, $\sigma_{\Delta\lambda,Vernier}$ the standard deviation of the noise on the binding curve of the Vernier-cascade, and $\sigma_{\Delta\lambda,ring}$ the standard deviation of the uncorrelated noise of the individual biosensor and reference sensor. The latter is multiplied by a factor $\sqrt{2}$ to account for taking the difference between the two signals to obtain the binding curve. Expression (6.1) should be larger than one to favor the Vernier-cascade with spectral filter.

The sensitivity of the Vernier-cascade configuration is enhanced over the unconnected configuration (section 5.3.1):

$$\frac{S_{slope,Vernier}}{S_{slope,ring}} = S^* > 1$$

with a sensitivity enhancement factor S^* up to several hundreds.

Whereas the broad envelope of the Vernier-cascade reduced its attainable temporal resolution when interrogated by wavelength scanning, here it allows very fast interrogation at the line rate of a detector array, typically several kHz. This is easily a hundred times faster than the interrogation rate of a ring resonance with an external cavity tunable laser.

If the differential noise in the refractive index and temperature of the sample liquid between the biosensor ring resonator and reference ring resonator dominates the noise on the binding curve, the Vernier-cascade amplifies the noise together with the analyte signal. In that case the ratio of the standard deviations of the noise on the binding curve becomes

$$\frac{\sqrt{2} \cdot \sigma_{\Delta\lambda,ring}}{\sigma_{\Delta\lambda,Vernier}} = \frac{\sqrt{2}}{S^*}$$

In these noisy circumstances, the ratio of the limits of detection of both configurations (equation 5.9) is thus beneficial for the Vernier-cascade with on-chip spectral filter:

$$\frac{LOD_{ring}}{LOD_{Vernier}} = \sqrt{2} \cdot \frac{\sqrt{R_{t,Vernier}}}{\sqrt{R_{t,ring}}}, \quad (6.2)$$

since it can be interrogated much faster, allowing more accurate fitting to the initial slope of the binding curve. However, while the improvement expressed by equation (6.2) can go up to an order of magnitude, the improvement is probably smaller in practice, since the expression is only valid if the noise on the binding curve is uncorrelated Gaussian noise, an unlikely condition at very high temporal resolution.

If the refractive index noise and temperature noise are sufficiently compensated by the reference sensors to make optical noise on the transmission spectra dominant, the inaccuracies in the extraction of the spectral position by data-fitting determine the noise on the binding curve. While the sharp ring resonances interrogated with a wavelength scan can be resolved up to tens of femtometers (section 2.4.4 in chapter 2), the filtered broadband transmission spectrum of a Vernier-cascade can less accurately be tracked. Our preliminary proof-of-concept experiment (section 6.4) resulted in binding curve noise as high as hundreds of picometers, but this is a conservative value derived from a suboptimal experiment. Monte-Carlo simulations with a similar method as presented in section 2.4.4 of chapter 2 indicate that binding curve noise of tens of picometers is feasible. While this is still three orders of magnitude worse compared to a laser-interrogated single ring resonator sensor, the limits of detection of both configurations are comparable, taking into account the attainable two orders of magnitude enhancement in the sensitivity and two orders of magnitude larger temporal resolution of the Vernier-cascade compared to the single ring resonator,

Despite the low spectral resolution, interrogation of a Vernier-cascade sensor with a broadband light source and an on-chip spectral filter can reach a comparable limit of detection as the more expensive and bulky wavelength scan interrogation of a ring resonator sensor.

6.3 Compact silicon Vernier-cascade sensor with on-chip arrayed waveguide grating

We chose to integrate a Vernier-cascade sensor with a well-known and compact arrayed waveguide grating (AWG) [4], as depicted in Figure 6.3. The silicon Vernier-cascade sensor for this experiment entirely consists of the 450 nm-wide single-mode waveguide proposed in section 2.1.1 of chapter 2, and was fabricated using the process described before (section 2.1.1 in chapter 2) and elaborated in [6, 7]. A 600 nm thick cladding of photopatternable Cyclotene with low water absorption (section 2.4.3 in chapter 2) covers the complete chip except for a window to the second resonator. The filter and sensor resonator roundtrip lengths were chosen respectively $1271 \mu\text{m}$ and $1257 \mu\text{m}$ so that the sensor would have a clearly visible envelope signal and would have a large sensitivity, while retaining acceptable roundtrip losses. Both resonator cavities were folded with a $6 \mu\text{m}$ bend radius to reduce their footprint to less than $7500 \mu\text{m}^2$.

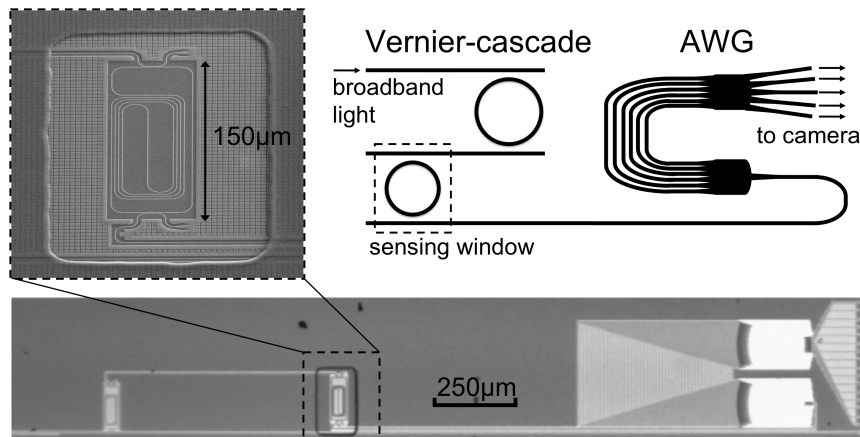


Figure 6.3: An arrayed waveguide grating (AWG) is a well-known spectral filter that can be made very compact with high quality in silicon, while providing sufficient spectral resolution (in the order of a nanometer) to accurately filter the envelope from the transmission spectrum of a Vernier-cascade. The micrograph of the silicon-on-insulator chip shows the compact folded cavities of the ring resonators constituting the Vernier-cascade that is connected to a dense 16-channel AWG. To allow easy application of refractive index differences between the resonators in the proof-of-concept experiment, the chip is covered with a Cyclotene cladding except for a window to the second resonator.

The AWG has 16 channels with 1.6 nm spacing, so that its bandwidth is larger than the envelope period of the sensor (13 nm) to avoid it from limiting the sensor's dynamic range. The chosen channel spacing is the result of a trade-off between having a high resolution and having enough spectral averaging per channel to be able to reveal the envelope signal directly with a broadband light source. The AWG's footprint is only $750 \mu\text{m} \times 350 \mu\text{m}$, which is smaller than a planar concave grating with similar specifications [4].

To couple light from and to the device, the input and output waveguides were adiabatically tapered to a $10 \mu\text{m}$ wide ridge waveguide in which a second-order grating was etched to diffract TE-polarized light out-of-plane (section 2.8.1 of chapter 2). The relative power diffracted to free space by all output gratings, each corresponding with a channel of the AWG, was monitored in parallel using a near-infrared camera with a microscope objective at a distance of several centimeters from the chip. A standard single-mode optical fiber was butt-coupled to the input grating.

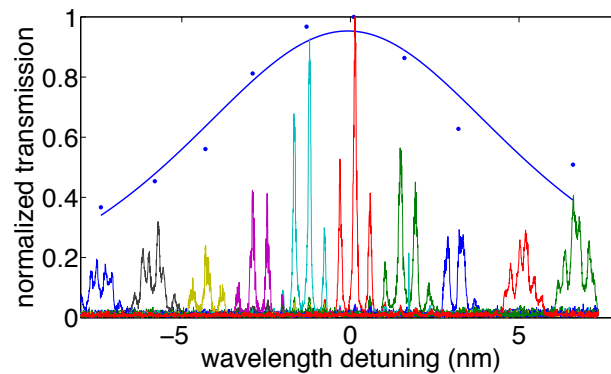


Figure 6.4: The transmission spectrum of the Vernier-cascade through different channels of the AWG measured with a tunable laser (bottom, a color for each AWG-channel) shows the envelope peak superposed on the sharp constituent peaks. Approximately three constituent peaks are transmitted by each channel, providing enough power averaging per channel to also reveal the shape of the envelope peak when the transmission is measured with a broadband light source (blue dots). A squared Lorentzian function can be satisfactorily fitted to the broadband transmission peak (blue line), allowing accurate determination of the peak position.

An envelope peak superposed on the constituent peaks is visible in the transmission spectrum of the water-covered Vernier-cascade sensor fil-

tered by the AWG to its different channels (Figure 6.4), confirming the on-chip spectral filtering and parallel camera read-out. The spectrum measured by stepping the wavelength of a tunable laser shows that approximately three constituent peaks are transmitted by each channel, providing enough power averaging to also reveal the envelope shape when the transmission spectrum is measured with a super-luminescent light emitting diode (LED) broadband light source with $1.55\ \mu\text{m}$ central wavelength. A squared Lorentzian function (equation 5.3 in chapter 5) is satisfactorily fitted to this envelope peak, allowing accurate determination of the peak position. The broadband input power was limited to 10 mW to avoid saturation of the camera, proving that the transmission of the combination of the Vernier-sensor and AWG is sufficiently high for practical applications.

6.4 Real-time refractive index change measurement

The performance of the device as transducer for label-free biosensing was characterized by measuring the refractive index change of watery salt solutions in real-time. To allow controlled delivery of the solutions to the sensor, a microfluidic channel with $600\ \mu\text{m} \times 50\ \mu\text{m}$ cross section was made in polydimethylsiloxane (PDMS) by casting and directly bonded to the sensor chip. Using a syringe pump, the solutions were pumped at a $10\ \mu\text{L}/\text{min}$ flow rate over both resonators of the Vernier-cascade to keep them both in thermal contact with the liquid. As the thermo-optic coefficient of the Cyclotene cladding ($-1.5 \cdot 10^{-4} / \text{K}$ [8]) is close to the thermo-optic coefficient of water ($-1.1 \cdot 10^{-4} / \text{K}$ at $1550\ \text{nm}$ [9]), both resonators react similarly to changes in the liquid temperature. Hence the device is very tolerant to temperature changes and no thermal control was needed for the experiment. While the flow was repeatedly switched between deionized water and three different concentrations of NaCl in water, the broadband transmission of the Vernier-cascade sensor through the different channels of the AWG was measured with a suboptimal 6 Hz resolution and the spectral position of the transmission peak was determined by fitting the squared Lorentzian function mentioned before. The refractive index of the salt solutions was calculated according to ref. [10].

The device allows to monitor refractive index changes continuously (Figure 6.5), but the noise on the sensorgram was unexpectedly high (290 pm standard deviation) due to excessive intensity noise on the spectrum. This was probably caused by vibrations of the input fiber, and is not a funda-

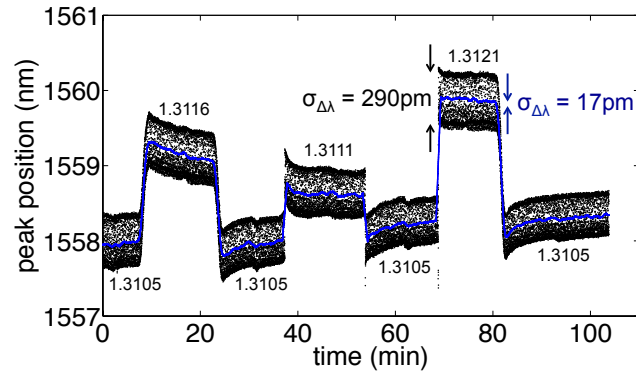


Figure 6.5: The device can continuously monitor refractive index changes of watery NaCl solutions in real-time while being interrogated with a low-cost broadband light source, making it very applicable in low-cost label-free biosensing. The noise on the sensorgram was unexpectedly high (290 pm standard deviation), probably due to vibrations on the input fiber. After smoothing the signal with a 1 min window, the standard deviation of the noise was only 17.4 pm, illustrating the potential of interrogation with high temporal resolution.

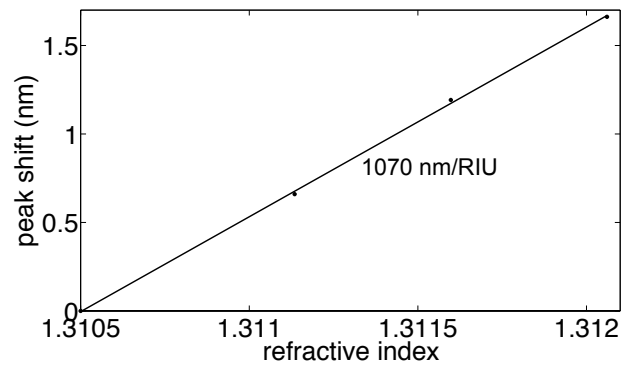


Figure 6.6: The sensor responded very linearly to refractive index changes with 1070 nm/RIU sensitivity.

mental problem of the device, as it can be overcome with more robust read-out instrumentation. However, this noisy experiment allows to illustrate the importance of fast sensor interrogation: even the moderate temporal resolution in this experiment (6 Hz) already allows to significantly reduce the impact of noise. This is illustrated by smoothing the sensorgram (blue in Figure 6.5) with a moving average with a window of one minute, which results in only 17 pm standard deviation on the new sensorgram. Therefore, despite the noisy experiment, the device could monitor the refractive index changes accurately, with a highly linear dependence of its peak shift with a sensitivity as large as 1070 nm/RIU (Figure 6.6). Faster read-out of a camera or detector array, with several kHz feasible, can further exploit this effect in future experiments.

An unresolved issue remains the cause of the drift of the sensor signal during the experiment, which was negative for salt solutions and positive for deionized water. Diffusion of ions in and out the Cyclotene cladding is considered as a possible cause.

6.5 Conclusions

Despite the low spectral resolution, interrogation of a Vernier-cascade sensor with a broadband light source and an on-chip spectral filter can reach a comparable or even better limit of detection as the more expensive and bulky wavelength scan interrogation of a ring resonator sensor. The more compact read-out instrumentation moreover is more widely applicable, and has the prospect of further integration.

One question that remains is whether this scheme of interrogation with a broadband light source can be scaled to a high degree of multiplexing, since it typically has a significantly lower power density than a laser. Our experiment indicated that there is sufficient power budget for several sensors, but simultaneous interrogation of tens or hundreds of sensors would require adaptations to the read-out. This is an interesting topic for future research.

References

- [1] B. Sepulveda, J. Sanchez del Rio, M. Moreno, F. J. Blanco, K. Mayora, C. Dominguez, and L. M. Lechuga. *Optical biosensor microsystems based on the integration of highly sensitive Mach-Zehnder interferometer devices*. J. Opt. A: Pure Appl. Opt., 8(7, Sp. Iss. SI):S561–S566, JUL 2006.
- [2] Panagiota S. Petrou, Maria Kitsara, Eleni Makarona, Ioannis Raptis, Sotirios E. Kakabakos, Remco Stoffer, Gerhard Jobst, and Konstantinos Misiakos. *Monolithically Integrated Biosensors based on Frequency-Resolved Mach-Zehnder Interferometers for Multi-analyte determinations*. In Conf. Proc. IEEE Eng. Med. Biol. Soc., page 298, 2010.
- [3] Lei Jin, Mingyu Li, and Jian-Jun He. *Optical waveguide double-ring sensor using intensity interrogation with a low-cost broadband source*. Opt. Lett., 36(7):1128–1130, Apr 2011.
- [4] Wim Bogaerts, Shankar Kumar Selvaraja, Pieter Dumon, Joost Brouckaert, Katrien De Vos, Dries Van Thourhout, and Roel Baets. *Silicon-on-Insulator Spectral Filters Fabricated With CMOS Technology*. IEEE J. Sel. Topics Quantum Electron., 16(1):33–44, JAN-FEB 2010.
- [5] Zhixuan Xia, Babak Momeni, Murtaza Askari, Maysamreza Chamanzar, Siva Yegnanarayanan, Ali Asghar Eftekhari, and Ali Adibi. *Silicon Microring Resonator Sensor with Integrated PC Spectrometer for Sharp Spectral Features Detection*. In IEEE Photonics Annual Meeting, pages 329–330, 2010.
- [6] Shankar Kumar Selvaraja, Patrick Jaenen, Wim Bogaerts, Dries Van Thourhout, Pieter Dumon, and Roel Baets. *Fabrication of Photonic Wire and Crystal Circuits in Silicon-on-Insulator Using 193-nm Optical Lithography*. J. Lightw. Technol., 27(18):4076–4083, 2009.
- [7] Shankar Kumar Selvaraja. *Wafer-Scale Fabrication Technology for Silicon Photonic Integrated Circuits*. PhD thesis, Universiteit Gent, 2011.
- [8] Kesavan S/O Ulaganathen. *Attenuation Measurement On Cyclotene (Bcb Photo Resin) Polymer Based Slab Waveguide*. Master's thesis, Faculty of Electrical Engineering, Universiti Teknologi Malaysia, 2005.

-
- [9] Chang-Bong Kim and Chin B Su. *Measurement of the refractive index of liquids at 1.3 and 1.5 micron using a fibre optic Fresnel ratio meter*. *Measurement Science and Technology*, 15(9):1683, 2004.
- [10] Hui Su and Xu Guang Huang. *Fresnel-reflection-based fiber sensor for on-line measurement of solute concentration in solutions*. *Sens. Actuators, B*, 126(2):579–582, OCT 1 2007.

7

Conclusions

Silicon ring resonators form a promising platform for highly-multiplexed label-free sensing (chapter 2) that in contrast with widespread label-based techniques can continuously monitor biomolecular interactions, providing highly quantitative measures on the concentration, affinity and binding kinetics. Moreover, label-free assays require almost no sample preparation, lowering the cost and enhancing the throughput, and simplify assay development, especially for highly-multiplexed assays, since only one recognition element is required for each analyte. Developing this platform is highly multidisciplinary, since it not only needs an efficient transducer, but also performant read-out, assays and mass transport. Nevertheless, the silicon photonic transducer is the main differentiator from other label-free platforms, and the versatility of silicon photonics offers a unique toolset to make the platform truly excel over others.

A common problem for all label-free platforms is that straightforward direct label-free assays are often less specific than sandwich assays, since they only employ a single biomolecular recognition element. The dual polarization ring resonator sensor we propose (chapter 3) can distinguish between the refractive index and thickness of thin dielectric layers, and has the prospect of being able to do so with sufficient accuracy to measure

structural molecular changes that allow distinguishing specific interactions from non-specific ones. Moreover, it allows to study molecular interactions in more depth by providing information on e.g. DNA-orientation or protein conformation, which has already proven to play an important role in several cancers and in Alzheimer's disease.

Another primary concern of the platform is the moderate limit of detection (1.5 pg/mm^2), as it is insufficient for the direct (unamplified) detection of small molecules, such as cytokines at clinically relevant concentrations. Therefore, we derived an approximate formula for the limit of detection (section 2.4 in chapter 2) of accurate concentration measurements based on least-squares fitting the initial slope of the binding curve. It identifies the governing parameters and can serve as a figure of merit in the initial comparison of transducers and interrogation techniques. It shows that the resonance wavelength sensitivity of the ring sensor is only one parameter, and that the temporal resolution of and the noise on the binding curve also have a significant impact. The formula first of all indicates that reference sensors for compensation of refractive index and temperature noise are indispensable. A second implication of the formula is that not only sharp and deep resonances are important in the design of ring resonator sensors, but also small values of the free spectral range, since this allows faster interrogation of a multiplexed platform using wavelength scanning. Therefore, ring resonator sensors with large roundtrips (up to 7 mm) in folded cavities are beneficial (section 2.4.4 in chapter 2).

Slot waveguide ring resonator sensors (chapter 4) were found to improve the resonance wavelength sensitivity through enhanced light-matter interaction. However, the sixfold gain is too small to compensate the drawbacks: extra optical losses and troubled biochemical surface modification.

Vernier-cascade ring resonator sensors (chapter 5) have a much larger gain of the wavelength sensitivity (up to two orders of magnitude), do not complicate the biochemical surface modification, and additionally optically compensate the most important noise factors. Although they are less suited for fast interrogation with a wavelength scan because of their broad transmission spectrum, they can be combined with an on-chip spectral filter to provide very fast and cost-effective interrogation with a broadband light source (chapter 6). Our preliminary results indicate that this transducer can offer the same or better limit of detection than optimized ring resonator sensors with separate reference sensors that are interrogated with a more expensive and bulky high-end exter-

nal cavity laser. Moreover, it has the prospect of more compact read-out instrumentation that is more widely applicable.

7.1 Perspectives

While this thesis introduced novel silicon photonic transducers for label-free sensing, and presented initial proofs-of-concept that indicate their strengths and weaknesses, it should be clear that only relevant multiplexed assays performed in (diluted) serum in an optimized read-out instrument provides the necessary data for a proper comparison with other technologies. The main challenge for any label-free technology is to bridge the gap between the different disciplines, and provide a prototype platform that comprises efficient optics, fluidics and biochemistry. The obvious next step is to integrate the most promising sensors, such as the Vernier-cascade with integrated arrayed waveguide grating, into such a prototype, and characterize the most important parameters, such as the limit of detection, for relevant model assays.

Regarding the silicon ring resonator transducers themselves, it is worth researching whether operating at smaller wavelengths (e.g. $1.3\ \mu\text{m}$) with the quasi-TM waveguide mode improves the performance, since it suffers less from absorption by water and from scattering at sidewall roughness. However, the improvement might be marginal, and will only be visible when refractive index and temperature noise are sufficiently compensated. A larger benefit can be offered by silicon nitride ring resonator sensors, since they can operate at visible wavelengths with very low water absorption, while still being compatible with the fabrication facilities for the silicon electronics industry. Moreover, the cost of the interrogation instrument will benefit from the cheaper silicon detectors in this wavelength region. However, the lower refractive index contrast reduces the attainable density of microarrays, which could limit its use for very high-throughput and/or high-content applications, and currently the wafer-scale fabrication with optical lithography is less mature than for silicon-on-insulator.

On the long term, the largest asset of silicon photonic ring resonator label-free sensors is their potential towards integration with other (micro)systems due to their small size and flexible read-out with grating couplers. This could lead to integration in existing instruments, or in new laboratories-on-a-chip.



First order approximation of the roundtrip phase

The transmission of a ring resonator, as expressed by formulas (2.3), (2.8) and (2.12), depends on the wavelength-dependent roundtrip phase ϕ :

$$\phi = \frac{2\pi}{\lambda} n_{eff}(\lambda) L \quad (\text{A.1})$$

with λ the wavelength, L the physical roundtrip of the resonator and $n_{eff}(\lambda)$ the wavelength-dependent effective refractive index. Since our waveguides are very dispersive, this wavelength dependency has to be taken into account.

Approximating the effective refractive index by its first order Taylor series at an arbitrary fixed wavelength λ_0 yields

$$\phi \approx \frac{2\pi}{\lambda} L \left[n_{eff}(\lambda_0) + \frac{\partial n_{eff}(\lambda_0)}{\partial \lambda} (\lambda - \lambda_0) \right] \quad (\text{A.2})$$

$$= \frac{2\pi}{\lambda} L \left[n_{eff}(\lambda_0) - \lambda_0 \frac{\partial n_{eff}(\lambda_0)}{\partial \lambda} + \lambda \frac{\partial n_{eff}(\lambda_0)}{\partial \lambda} \right] \quad (\text{A.3})$$

Using the definition of the group index (equation 2.1)

$$n_g(\lambda_0) = n_{eff}(\lambda_0) - \lambda_0 \frac{\partial n_{eff}(\lambda_0)}{\partial \lambda} \quad (\text{A.4})$$

equation (A.3) becomes

$$\phi \approx \frac{2\pi}{\lambda} n_g(\lambda_0) L + \frac{2\pi}{\lambda_0} (n_{eff}(\lambda_0) - n_g(\lambda_0)) L$$

The wavelength-dependent first term determines the shape of the ring resonator transmission spectrum, while the constant second term determines the position of the resonances.

B

Derivation of the Lorentzian approximation of resonances

B.1 Lorentzian approximation of resonance dips

The power transmission to the pass port of a channel drop ring resonator is introduced in section 2.2.2:

$$T_{pass}(\lambda) = \frac{\tau_1^2 + a^2\tau_2^2 - 2a\tau_1\tau_2 \cos\left(\frac{2\pi}{\lambda} n_{eff}L\right)}{1 + (a\tau_1\tau_2)^2 - 2a\tau_1\tau_2 \cos\left(\frac{2\pi}{\lambda} n_{eff}L\right)} \quad (\text{B.1})$$

Note that the power transmission of an all-pass ring resonator (equation (2.3)) can be seen as the pass transmission of a channel drop ring resonator that has no coupling in its second coupler ($\tau_1 = \tau$ and $\tau_2 = 1$), so that the derivation also applies for all-pass ring resonators.

Equation B.1 can be rewritten as

$$T_{pass}(\lambda) = \frac{(\tau_1 - a\tau_2)^2 + 2a\tau_1\tau_2(1 - \cos\left(\frac{2\pi}{\lambda} n_{eff}L\right))}{(1 - a\tau_1\tau_2)^2 + 2a\tau_1\tau_2(1 - \cos\left(\frac{2\pi}{\lambda} n_{eff}L\right))}$$

Substituting equation (2.10) of the transmission at resonance

$R_{min} = \frac{(\tau_1 - a\tau_2)^2}{(1 - a\tau_1\tau_2)^2}$, and $1 - \cos\phi = \left(\sin\frac{\phi}{2}\right)^2$ results in

$$T_{pass}(\lambda) = \frac{R_{min} + \frac{4a\tau_1\tau_2}{(1 - a\tau_1\tau_2)^2} \left(\sin\left(\frac{\pi}{\lambda} n_{eff} L\right)\right)^2}{1 + \frac{4a\tau_1\tau_2}{(1 - a\tau_1\tau_2)^2} \left(\sin\left(\frac{\pi}{\lambda} n_{eff} L\right)\right)^2} \quad (\text{B.2})$$

Close to a resonance, the sine can be approximated by its first order Taylor polynomial at that resonance:

$$\sin\left(\frac{\pi}{\lambda} n_{eff} L\right) \approx \cos(m\pi) \frac{\pi L \left(\frac{\partial n_{eff}}{\partial \lambda} \lambda_{res} - n_{eff}\right)}{\lambda_{res}^2} (\lambda - \lambda_{res}) \quad (\text{B.3})$$

$$= (-1)^{m+1} \frac{\pi L n_g}{\lambda_{res}^2} (\lambda - \lambda_{res}) \quad (\text{B.4})$$

using the definition of the group refractive index $n_g = n_{eff} - \lambda_{res} \frac{\partial n_{eff}}{\partial \lambda}$.

Substituting (B.4) in (B.2) yields the approximate power transmission near the resonance dip:

$$T_{dip}(\lambda) \approx \frac{R_{min} + \left(\frac{2\sqrt{a\tau_1\tau_2}\pi L n_g}{(1 - a\tau_1\tau_2)\lambda_{res}^2}\right)^2 (\lambda - \lambda_{res})^2}{1 + \left(\frac{2\sqrt{a\tau_1\tau_2}\pi L n_g}{(1 - a\tau_1\tau_2)\lambda_{res}^2}\right)^2 (\lambda - \lambda_{res})^2} \quad (\text{B.5})$$

Inserting the formula for the full-width at half-maximum $FWHM = \frac{(1 - a\tau_1\tau_2)\lambda_{res}^2}{\pi n_g L \sqrt{a\tau_1\tau_2}}$ finally gives

$$T_{dip}(\lambda) \approx \frac{R_{min} \left(\frac{FWHM}{2}\right)^2 + (\lambda - \lambda_{res})^2}{\left(\frac{FWHM}{2}\right)^2 + (\lambda - \lambda_{res})^2}$$

This is the approximation proposed in equation (2.15).

B.2 Lorentzian approximation of resonance peaks

Similar to the derivation in previous section, the power transmission of the drop port of a channel drop filter

$$T_{drop}(\lambda) = \frac{a(1 - \tau_1^2)(1 - \tau_2^2)}{1 + (a\tau_1\tau_2)^2 - 2a\tau_1\tau_2 \cos\left(\frac{2\pi}{\lambda} n_{eff} L\right)}$$

can be rewritten as

$$T_{drop}(\lambda) = \frac{R_{max}}{1 + \frac{4a\tau_1\tau_2}{(1-a\tau_1\tau_2)^2} \left(\sin\left(\frac{\pi}{\lambda} n_{eff} L\right)\right)^2}$$

using equation (2.14) of the power transmission at resonance

$$R_{max} = \frac{a(1-\tau_1^2)(1-\tau_2^2)}{(1-a\tau_1\tau_2)^2}.$$

Substituting the first order Taylor approximation of the sine (equation (B.4)) yields an approximation of the power transmission close to the resonance peaks:

$$T_{peak}(\lambda) \approx \frac{R_{max} \frac{(1-a\tau_1\tau_2)^2}{4a\tau_1\tau_2}}{\frac{(1-a\tau_1\tau_2)^2}{4a\tau_1\tau_2} + \left(\frac{\pi L n_g}{\lambda_{res}^2}\right)^2 (\lambda - \lambda_{res})^2}$$

which finally reduces to

$$T_{peak}(\lambda) \approx \frac{R_{max} \left(\frac{FWHM}{2}\right)^2}{\left(\frac{FWHM}{2}\right)^2 + (\lambda - \lambda_{res})^2}$$

using the same expression for the full-width at half-maximum as in previous section. This approximation for T_{peak} corresponds with equation (2.16).

C

Derivation of a formula for the resonance wavelength shift due to an effective refractive index change

Section 2.2 in chapter 2 introduces the resonance condition of a ring resonator as:

$$\lambda = \frac{n_{eff} \cdot L}{m}, \quad m \in \mathbb{N} \quad (\text{C.1})$$

with λ the resonance wavelength, L the physical roundtrip length of the ring resonator and n_{eff} the effective refractive index of the waveguide mode.

Differentiating both sides of the equation yields:

$$d\lambda = \frac{dn_{eff} \cdot L}{m} \quad (\text{C.2})$$

In refractive index biosensing applications, n_{eff} changes due to variations in the (watery) cladding refractive index n_w , which results in a change of the resonance wavelength of the resonator. Due to dispersion (section

2.1.3), this resonance wavelength change will also have an effect on the effective refractive index. In a first order approximation we can decouple both effects:

$$d\lambda = \frac{\left(\frac{\partial n_{eff}}{\partial n_w} dn_w + \frac{\partial n_{eff}}{\partial \lambda} d\lambda\right) \cdot L}{m} \quad (C.3)$$

As described in section 2.1.3, first order dispersion is characterized by the group refractive index

$$n_g = n_{eff} - \lambda \frac{\partial n_{eff}}{\partial \lambda} \quad (C.4)$$

Substituting equations (C.1) and (C.4) in (C.3) yields

$$d\lambda = \frac{\frac{\partial n_{eff}}{\partial n_w} dn_w \cdot \lambda}{n_g} \quad (C.5)$$

The effective refractive index changes induced by changes of the cladding refractive index $\frac{\partial n_{eff}}{\partial n_w} dn_w$ will be further noted as Δn_{eff} , so that equation (C.5) finally becomes

$$d\lambda = \frac{\Delta n_{eff} \cdot \lambda}{n_g} \quad (C.6)$$

This formula has the same form as when dispersion would not be taken into account, but with the group refractive index in the denominator instead of the effective refractive index. In the case of our high-index-contrast waveguides this has a significant impact (up to a factor 2).

D

Derivation of a formula for the limit of detection

Calibration of the sensor results in a relation $\alpha(C)$ between the analyte concentration and the initial slope of the binding curve in the association phase. Since the slope is zero when the analyte is absent, it can be written as

$$\alpha(C) = C \cdot S_{slope}(C)$$

Although the slope sensitivity function $S_{slope}(C)$ can be concentration-dependent, for small values of the concentration it is well-approximated by the first term of its Taylor-series at zero concentration.

$$\begin{aligned} S_{slope}(C) &= S_{slope}(C=0) + \frac{\partial S_{slope}(C=0)}{\partial C} C + \frac{1}{2} \frac{\partial^2 S_{slope}(C=0)}{\partial C^2} C^2 + \dots \\ &\approx S_{slope}(C=0) \end{aligned}$$

Defining the slope sensitivity $S_{slope} = S_{slope}(C=0)$, small concentrations can thus be calculated from a measured initial slope α via:

$$C = \frac{\alpha}{S_{slope}} \quad (\text{D.1})$$

Neglecting calibration errors, which corresponds with assuming the slope sensitivity to be deterministic, the standard deviation on the measured concentration is

$$\sigma_C = \frac{\sigma_\alpha}{S_{slope}} \quad (D.2)$$

Since the noise on the binding curve typically has many independent contributions (temperature variations, liquid refractive index variations, detector noise,...), the noise on the binding curve is in good approximation Gaussian with standard deviation $\sigma_{\Delta\lambda}$. Least-squares fitting a straight line to N data points of the resonance wavelength shift $\Delta\lambda_i$ measured at time t_i ($i = 0, 1, \dots, N$) allows to determine the slope α with a Gaussian distribution and a standard deviation σ_α [1, 2]:

$$\sigma_\alpha = \frac{1}{\sqrt{N-2}} \sqrt{\frac{SS_{\Delta\lambda\Delta\lambda}}{SS_{tt}} - \alpha^2} \quad (D.3)$$

The sum of squares are defined as:

$$SS_{tt} = \sum_{i=0}^{N-1} (t_i - \bar{t})^2 \quad (D.4)$$

$$SS_{\Delta\lambda\Delta\lambda} = \sum_{i=0}^{N-1} (\Delta\lambda_i - \overline{\Delta\lambda})^2 \quad (D.5)$$

with \bar{t} and $\overline{\Delta\lambda}$ the average values of the measurement times and of the resonance wavelength shifts.

The sum of squares of the resonance wavelength shifts (equation (D.5)) can be rewritten as:

$$SS_{\Delta\lambda\Delta\lambda} = N \cdot \sigma_{\Delta\lambda}^2 \quad (D.6)$$

Choosing $t_0 = 0$ and assuming measurements at equally spaced time steps over a time interval T , the sum of squares of the measurement times (equation D.4) becomes:

$$SS_{tt} = \sum_{i=0}^{N-1} \left(i \cdot \frac{T}{N-1} - \bar{t} \right)^2 \quad (D.7)$$

$$= \frac{T^2}{(N-1)^2} \cdot \sum_{i=0}^{N-1} i^2 + N \cdot \bar{t}^2 - 2 \cdot \frac{T}{N-1} \cdot \bar{t} \cdot \sum_{i=0}^{N-1} i \quad (D.8)$$

with

$$\sum_{i=0}^{N-1} i = \frac{1}{2}N(N-1) \quad (D.9)$$

$$\sum_{i=0}^{N-1} i^2 = \frac{1}{6}N(N-1)(2N-1) \quad (D.10)$$

$$\bar{t} = \frac{T}{2} \quad (D.11)$$

Substituting equations (D.9) till (D.11) in equation (D.8) and assuming N large enough so that $N-2 \approx N-1 \approx N$, yields:

$$SS_{tt} \approx \frac{N \cdot T^2}{12} \quad (D.12)$$

Substituting equations (D.1), (D.6) and (D.12) in equation (D.3), and approximating $N-2 \approx N$ for large N , yields:

$$\sigma_{\alpha}(C) \approx \frac{1}{\sqrt{N}} \sqrt{\frac{12 \cdot \sigma_{\Delta\lambda}^2}{T^2} - (S_{slope} \cdot C)^2} \quad (D.13)$$

Equation (D.2) then becomes

$$\sigma_C(C) \approx \frac{1}{\sqrt{N}} \sqrt{\frac{12 \cdot \sigma_{\Delta\lambda}^2}{T^2 \cdot S_{slope}^2} - C^2} \quad (D.14)$$

When the concentration is small enough, so that

$$\frac{12 \cdot \sigma_{\Delta\lambda}^2}{T^2 \cdot S_{slope}^2} \gg C^2 \quad (D.15)$$

the standard deviation on the measured concentration is in good approximation independent of the concentration, and reduces to

$$\sigma_C(C) \approx \frac{2\sqrt{3} \cdot \sigma_{\Delta\lambda}}{\sqrt{N} \cdot T \cdot S_{slope}}$$

The fulfillment of condition (D.15) depends on the experiment. M. Iqbal et al. [3] measured the initial slope of their silicon ring resonator sensor system for the interaction of streptavidin with immobilized biotin, and from

their data follows $\sigma_{\Delta\lambda} = 0.22$ pm, $T = 8$ min and $S_{slope} = 0.18$ pm/min/pM and a limit of detection in the order of 0.06 pM, so that the left hand side of equation (D.15) is almost two orders of magnitude larger than the right hand side. This indicates the relevance of the approximation made here.

Often the resonance wavelengths will be measured at a fixed temporal resolution R_t , so that N is proportional to T . The standard deviation on the measured concentration can in that case be expressed as:

$$\sigma_C(C) \approx \frac{2\sqrt{3} \cdot \sigma_{\Delta\lambda}}{\sqrt{R_t} \cdot T^{\frac{3}{2}} \cdot S_{slope}}$$

References

- [1] <http://mathworld.wolfram.com/LeastSquaresFitting.html>.
- [2] E. S. Acton. *Analysis of Straight-Line Data*. Wiley Publication in Applied Statistics, 1966.
- [3] Muzammil Iqbal, Martin A. Gleeson, Bradley Spaugh, Frank Tybor, William G. Gunn, Michael Hochberg, Tom Baehr-Jones, Ryan C. Bailey, and L. Cary Gunn. *Label-Free Biosensor Arrays Based on Silicon Ring Resonators and High-Speed Optical Scanning Instrumentation*. IEEE J. Sel. Topics Quantum Electron., 16(3):654–661, May-June 2010.

E

Derivation of a formula for the period of a Vernier-cascade's envelope signal

When the free spectral range difference between the two resonators in a Vernier-cascade is small compared to the full-width at half-maximum of the resonance peaks of the individual resonators, a periodic envelope signal is superposed on the constituent transmission peaks in the transmission spectrum of the cascade. To derive the envelope period, we will start from the case displayed in Figure E.1, where the transmission spectra of the two individual ring resonators are plotted. The resonance wavelengths of the resonator with the shortest optical roundtrip (solid line) are denoted λ_{short} , and the resonance wavelengths of the resonator with the longest optical roundtrip (dashed line) as λ_{long} .

At the wavelength λ_0 two resonances of the respective resonators coincide. Neglecting group index dispersion, the other resonance wavelengths of both resonators are

$$\lambda_{short,k} = \lambda_0 + k \cdot FSR_{short} \quad (\text{E.1})$$

$$\lambda_{long,k} = \lambda_0 + k \cdot FSR_{long} \quad (\text{E.2})$$

with FSR the free spectral range of the corresponding resonator and k an

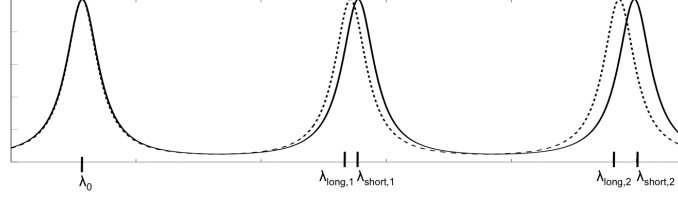


Figure E.1: Transmission spectra of the two individual ring resonators with different optical roundtrip. The resonator with the short optical roundtrip (solid line) has a larger free spectral range than the resonator with the long optical roundtrip (dashed line).

integer.

Starting from λ_0 , an envelope period will be reached when two resonances coincide again. This occurs for an index $k = K$ for which:

$$\lambda_{short,K} = \lambda_{long,K+1} \quad (\text{E.3})$$

$$\Leftrightarrow K \cdot FSR_{short} = (K+1) \cdot FSR_{long} \quad (\text{E.4})$$

$$\Leftrightarrow K = \frac{FSR_{long}}{FSR_{short} - FSR_{long}} \quad (\text{E.5})$$

The two resonances will only exactly coincide when K is an integer. However, when the free spectral range difference between the two resonators in the cascade is small compared to the full-width at half-maximum of the resonance peaks of the individual resonators, this period will also be visible when K is not an integer.

The envelope period is given by

$$P_{envelope} = \lambda_{short,K} - \lambda_0 \quad (\text{E.6})$$

By substituting Eq. (E.5) in Eq. (E.1), the formula for the period becomes:

$$P_{envelope} = \frac{FSR_{long} \cdot FSR_{short}}{FSR_{short} - FSR_{long}} \quad (\text{E.7})$$

$$= \frac{FSR_{filter} \cdot FSR_{sensor}}{|FSR_{sensor} - FSR_{filter}|} \quad (\text{E.8})$$

F

Analysis of the constituent peaks in a Vernier-cascade's transmission spectrum

As the peaks in the transmission spectrum of a channel drop ring resonator are well-approximated by a Lorentzian function (section 2.2.3 in chapter 2), each of the constituent peaks in the transmission spectrum of a Vernier-cascade can be described as the product of two Lorentzian functions that are shifted relative to each other:

$$T_{const}(\lambda) = \frac{R_{max,filter} \left(\frac{FWHM_{ring}}{2}\right)^2}{\left(\frac{FWHM_{ring}}{2}\right)^2 + \left(\lambda - \lambda_m - \frac{\Delta\lambda}{2}\right)^2} \cdot \frac{R_{max,sensor} \left(\frac{FWHM_{ring}}{2}\right)^2}{\left(\frac{FWHM_{ring}}{2}\right)^2 + \left(\lambda - \lambda_m + \frac{\Delta\lambda}{2}\right)^2} \quad (\text{E1})$$

where R_{max} and $FWHM_{ring}$ are respectively the transmission at resonance and the full-width at half-maximum of each of the resonance peaks of the individual ring resonators, and where λ_m and $\Delta\lambda$ are respectively the mean of and the difference between the two resonance wavelengths under consideration from both combs.

This equation can be rewritten as:

$$T_{const}(\lambda) = \frac{T_{max} \cdot \left(\frac{FWHM_{ring}}{2}\right)^4}{\left(\left(\frac{FWHM_{ring}}{2}\right)^2 + \left(\lambda - \lambda_m - \frac{\Delta\lambda}{2}\right)^2\right) \cdot \left(\left(\frac{FWHM_{ring}}{2}\right)^2 + \left(\lambda - \lambda_m + \frac{\Delta\lambda}{2}\right)^2\right)} \quad (F.2)$$

with $T_{max} = R_{max,filter} \cdot R_{max,sensor}$

The location of the extreme values of this function can be found by solving following equation to λ :

$$\frac{\partial T_{const}(\lambda)}{\partial \lambda} = 0 \quad (F.3)$$

This results in three extreme values at wavelengths

$$\lambda_m, \lambda_m + \frac{\sqrt{\Delta\lambda^2 - FWHM_{ring}^2}}{2}, \lambda_m - \frac{\sqrt{\Delta\lambda^2 - FWHM_{ring}^2}}{2} \quad (F.4)$$

There are two possibilities for the location and values of the maxima of the constituent peaks.

First, if the difference between the resonance wavelengths under consideration is larger than the full-width at half-maximum of the individual resonances ($\Delta\lambda > FWHM_{ring}$), the three extrema are all real. The constituent peak will in this case have two maxima at $\lambda_{max} = \lambda_m \pm \frac{\sqrt{\Delta\lambda^2 - FWHM_{ring}^2}}{2}$ and a local minimum at λ_m . The peak transmission at each of the two maxima is

$$T_{peak} = \left(\frac{\sqrt{T_{max}} \cdot FWHM_{ring}}{2 \cdot \Delta\lambda} \right)^2 \quad (F.5)$$

which quadratically converges to zero for increasing values of $\Delta\lambda$. This situation corresponds to the tails of the envelope, where the transmission is very low.

Second, if the difference between the resonance wavelengths under consideration is smaller or equal than the full-width at half-maximum of the individual resonators ($\Delta\lambda \leq FWHM_{ring}$), only one of the extreme values in equation (F.4) is real. This situation corresponds to the constituent peaks in the center of the envelope peak, where the transmission is high. In this case the constituent peak has a maximum at its central wavelength

λ_m , and the peak transmission at this maximum is given by

$$T_{peak} = \left(\frac{\sqrt{T_{max}} \cdot FWHM_{ring}^2}{FWHM_{ring}^2 + \Delta\lambda^2} \right)^2 \quad (E6)$$

In appendix G this formula forms the basis to calculate a formula for the envelope peaks in the transmission spectrum of a Vernier-cascade.

G

Derivation of a formula for the envelope peak in a Vernier-cascade's transmission spectrum

The highest constituent peaks in the center of an envelope peak only have one maximum, with a peak transmission (appendix F):

$$T_{peak} = \left(\frac{\sqrt{T_{max}} \cdot FWHM_{ring}^2}{FWHM_{ring}^2 + \Delta\lambda^2} \right)^2 \quad (G.1)$$

with T_{max} the maximal possible transmission of a constituent peak, $FWHM_{ring}$ the full-width at half-maximum of each of the resonance peaks, and $\Delta\lambda$ the difference between the two resonance wavelengths under consideration.

We will first consider the special case displayed in Fig. G.1 where there exists a wavelength λ_0 at which a resonance peak of the filter ring resonator (solid line) coincides with a resonance peak of the sensor ring resonator (dashed line). At this wavelength λ_0 , it holds that $\Delta\lambda_0 = 0$ and the corresponding constituent peak in the transmission spectrum

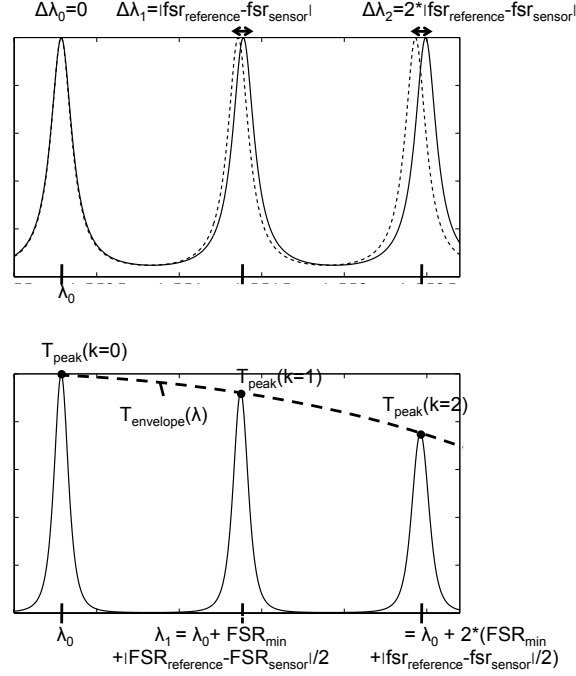


Figure G.1: Top: transmission spectra of the filter ring resonator (solid line) and sensor ring resonator (dashed line). Bottom: transmission spectrum of the cascade of the two ring resonators, showing three different constituent peaks of which the maxima form an envelope signal. This is a special case, where two resonance peaks coincide.

of the cascade will reach the maximum height of the envelope signal. For the next resonance peak of both resonators the resonance wavelength difference is equal to the difference in free spectral range, $\Delta\lambda_1 = |FSR_{sensor} - FSR_{filter}|$. The corresponding constituent peak will have a maximum at the mean resonance wavelength (appendix F):

$$\lambda_1 = \lambda_0 + FSR_{min} + \frac{|FSR_{sensor} - FSR_{filter}|}{2} \quad (G.2)$$

with $FSR_{min} = \min(FSR_{sensor}, FSR_{filter})$.

This reasoning can be generalized to all constituent peaks of the same

envelope peak:

$$\begin{aligned}\Delta\lambda_k &= |k \cdot (FSR_{sensor} - FSR_{filter})| \\ \lambda_k &= \lambda_0 + k \cdot \left(FSR_{min} + \frac{|FSR_{sensor} - FSR_{filter}|}{2} \right)\end{aligned}$$

where k is an integer.

Substituting the second equation in the first results in:

$$\Delta\lambda_k = \frac{|FSR_{sensor} - FSR_{filter}| \cdot |\lambda_k - \lambda_0|}{FSR_{min} + \frac{|FSR_{sensor} - FSR_{filter}|}{2}} \quad (G.3)$$

The second term in the denominator is typically much smaller than the first, so we can neglect the second term

$$\Delta\lambda_k \approx \frac{|FSR_{sensor} - FSR_{filter}| \cdot |\lambda_k - \lambda_0|}{FSR_{min}} \quad (G.4)$$

If we substitute equation (G.4) in equation (G.1), we get:

$$T_{peak}(k) = \left(\frac{\sqrt{T_{max}} \left(\frac{W}{2}\right)^2}{\left(\frac{W}{2}\right)^2 + (\lambda_k - \lambda_0)^2} \right)^2 \quad (G.5)$$

$$W = 2 \cdot \frac{FWHM_{ring} \cdot FSR_{min}}{|FSR_{filter} - FSR_{sensor}|} \quad (G.6)$$

This formula gives the peak transmission values of the highest constituent peaks in the central region of the envelope peak, for the special case where there exists a constituent peak that is the product of two coinciding resonance peaks.

It can be generalized to the formula of a continuous function going through the maxima of the constituent peaks, also for the case where there is no perfect coincidence of resonances, by defining $\lambda_{central}$ as the central wavelength of the envelope peak and by substituting λ_0 and λ_k respectively by $\lambda_{central}$ and the continuous wavelength λ :

$$T_{envelope}(\lambda) = \left(\frac{\sqrt{T_{max}} \left(\frac{W}{2}\right)^2}{\left(\frac{W}{2}\right)^2 + (\lambda - \lambda_{central})^2} \right)^2 \quad (G.7)$$

$$W = 2 \cdot \frac{FWHM_{ring} \cdot FSR_{min}}{|FSR_{filter} - FSR_{sensor}|} \quad (G.8)$$

The square of a Lorentzian function (equation (G.8)) with full-width at half maximum W (equation (G.8)) describes the envelope peak formed by the maxima of the highest constituent peaks very well. The envelope peak itself has a full-width at half-maximum formulated by:

$$\begin{aligned} FWHM_{envelope} &= \sqrt{\sqrt{2}-1} \cdot W \\ &= 2 \cdot \sqrt{\sqrt{2}-1} \cdot \frac{FWHM_{ring} \cdot FSR_{min}}{|FSR_{filter} - FSR_{sensor}|} \end{aligned}$$

H

Derivation of a formula for a Vernier-cascade's sensitivity

A differential resonance wavelength shift between the sensor resonator and filter resonator results in a much larger spectral shift of the transmission spectrum of the Vernier-cascade, increasing the sensitivity towards analyte molecules that only bind to the sensor resonator.

The sensitivity of a Vernier-cascade sensor to changes of the effective refractive index of the sensor resonator waveguide can be understood by considering the special case (Figure H.1) where there exists a wavelength λ_0 at which a resonance peak of the filter ring resonator (solid line) coincides with a resonance peak of the sensor ring resonator (dashed line). At this wavelength λ_0 the corresponding constituent peak in the transmission spectrum of the cascade will reach the maximum height of the envelope signal.

We distinguish two cases:

The first case is illustrated in the left graph in Figure H.1, and occurs when the free spectral range of the filter resonator is larger than the free spectral range of the sensor resonator. When in this case the resonance

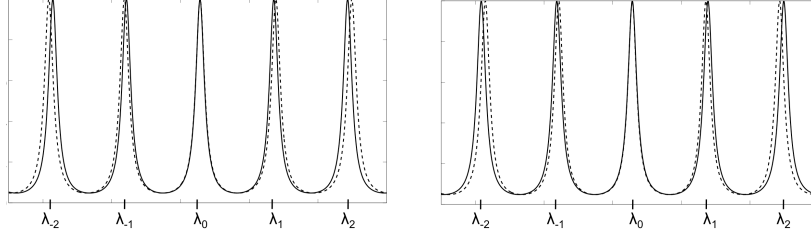


Figure H.1: Transmission spectra of the individual filter ring resonator (solid line) and sensor ring resonator (dashed line) for the case where two resonances of the respective resonators coincide at λ_0 . Left: the free spectral range of the filter resonator is larger than the free spectral range of the sensor resonator. Right: the free spectral range of the filter resonator is smaller than the free spectral range of the sensor resonator.

wavelengths of the sensor ring resonator shift to larger wavelengths over a spectral distance $|FSR_{sensor} - FSR_{filter}|$, the resonances of the filter and sensor resonators will overlap at wavelength λ_1 . The peak of the envelope signal will thus have shifted over a distance FSR_{filter} to larger wavelengths.

The second case is illustrated in the right graph in Figure H.1, and occurs when the free spectral range of the filter resonator is smaller than the free spectral range of the sensor resonator. When in this case the resonance wavelengths of the sensor ring resonator shift to larger wavelengths over a spectral distance $|FSR_{sensor} - FSR_{filter}|$, the resonances of the filter and sensor resonators will overlap at wavelength λ_{-1} . The peak of the envelope signal will thus have shifted over a distance FSR_{filter} to smaller wavelengths.

From both cases, we can conclude that the sensitivity of the Vernier-cascade sensor is equal to the sensitivity of the sensor ring resonator multiplied by a factor $\frac{FSR_{filter}}{FSR_{filter} - FSR_{sensor}}$. This factor is positive if $FSR_{filter} > FSR_{sensor}$ and negative when $FSR_{filter} < FSR_{sensor}$.

With the expression of the sensitivity of the sensor ring resonator (section 2.3.2 in chapter 2 and appendix C), the sensitivity of the Vernier-cascade becomes:

$$\Delta\lambda = \underbrace{\frac{\lambda \cdot \Delta n_{eff,sensor}}{n_{g,sensor}}}_{\text{sensor ring sensitivity}} \cdot \underbrace{\frac{FSR_{filter}}{FSR_{filter} - FSR_{sensor}}}_{\text{sensitivity enhancement}} \quad (\text{H.1})$$

with $n_{g,sensor}$ and $\Delta n_{eff,sensor}$ respectively the group refractive index and the change of the effective refractive index of the sensor resonator, and FSR_{filter} and FSR_{sensor} the free spectral range values of the corresponding resonators.